SYNTHESIS, FUNCTIONALIZATION AND CHARACTERIZATION OF HYBRID NANOSYSTEM

A thesis submitted in partial fulfillment of the requirements for
award of the degree of Doctor of Philosophy

MADHULEKHA GOGOI

Registration No: 067 of 2010

Department of Physics

School of Sciences

Tezpur University

Napaam, Tezpur – 784028

Assam, India

October 2013

“Science and everyday life cannot and should not be separated”

— **Rosalind Franklin**

SYNTHESIS, FUNCTIONALIZATION AND CHARACTERIZATION OF HYBRID NANOSYSTEM

Abstract

Nanotechnology is defined as the engineering of structures, devices and systems by controlled manipulation of size and shape at nanometer scale to produce newer ones with at least one novel/superior characteristic or property. Nanoparticles are the basic constituents of nanomaterials with at least one of the three dimensions in the range of 1-100 nm. Nanoparticles have been attracting a considerable attention because of their unique physical and chemical properties enabling them to find multidisciplinary applications [1-3]. Due to the enhanced implementation of nanoparticles in biomedical field, research on the development of multifunctional hybrid nanosystem is gaining momentum since last few years. Hybrids are developed by integrating more than one nanocomponent either in host template or by conjugating them directly [4-5]. They are multifunctional in the sense that they can impart more than one function synergistically. For example, magneto-fluorescent hybrid nanosystem developed by combining magnetic and fluorescent nanoparticles together are useful for dual imaging application with enhanced contrast property [6]. Magnetic nanoparticles can serve as contrast agent for magnetic resonance imaging (MRI) technique whereas fluorescent nanoparticles are used in real time monitoring of tumor targeting and treatment.

In the thesis, we have presented an in-depth study on synthesis and properties of magnetic and fluorescent nanoparticles and their magneto fluorescent hybrid nanosystems developed by using silica as template. The multifunctional applicability of the so prepared hybrid nanosystems has been demonstrated in biomedical applications. Also, multifunctionality in a single moiety nanosystem as potential MRI contrast agent as well as therapeutic agent has been discovered.

Chapter 1 gives a general introduction and background of scientific research in hybrid nanosystem. This is followed by brief discussions of different imaging functionalities of hybrid nanosystems. Also, the strategy for delivery of such systems to targeted locations is touched upon. Then the synthetic approaches of multifunctional hybrid nanosystems are discussed. A brief introduction to the magnetic and optical imaging is also presented. Finally, the objectives of the thesis are identified at the end of this chapter based on the literature review.

In **Chapter 2**, the experimental details of the thesis work is outlined. All the chemicals used, the synthetic routes followed and the instrumentation techniques that were used to analyze the samples, are introduced in this chapter.

Chapter 3 is divided into two parts. **Part A** describes the synthesis of fatty acid capped superparamagnetic iron oxide nanoparticles (SPION) by a non-aqueous method involving thermal decomposition of precursor followed by isothermal heat treatment. Then a facile method is reported for controlled replacement of fatty acid from nanoparticle surface with a hydrophilic ligand to obtain ultrastable hydrophilic nanoparticles with unaltered morphology, phase and properties. The surface chemistry of functionalized SPIONs is analyzed by Fourier Transform Infrared spectroscopy (FTIR), thermogravimetric analysis (TGA) and X-ray photoelectron spectroscopy (XPS) revealing the presence of bound and unbound thiol groups and disulfides, leading to its prolonged stability in aqueous medium.

Part B of **Chapter 3** describes a facile, aqueous, thermo-free, green synthetic route for developing an iron-platinum nanosystem using ascorbic acid as both reducing and capping agent. Detailed microstructural, magnetic and surface properties of the nanoparticles are studied with the aid of high resolution transmission electron microscopy, X-ray diffraction, vibrating sample magnetometer (VSM), FTIR and XPS results. Optimization of reaction conditions such as reducing agent, pH and sequence of precursor addition is explained to obtain highly water soluble, superparamagnetic iron-platinum nanosystems stabilized with ascorbic acid.

Chapter 4 is divided into two parts. **Part A** describes the aqueous colloidal synthesis of a size-tunable undoped and Mn^{2+}-doped cadmium telluride (CdTe) quantum dots with emission wavelength varying between 500 to 680 nm. Differentially tunable optical properties of doped and undoped CdTe quantum dots have been explained from UV-Visible absorption and photoluminescence spectroscopy. The size tunable emission of the QDs is achieved through Ostwald ripening phenomenon while in case of doped QDs, surface adsorbed Mn promotes ripening of the system as well as disintegration into smaller fraction after saturation in growth occurs. In the present chapter, photophysics of Mn^{2+}-doped nanocrystals is explained as well as an optimum size fraction is identified for both the doped and undoped QDs based on their PL quantum yield.

Part B of **Chapter 4** describes the facile synthesis of organic dye from oleylamine and glutaraldehyde. The dye compound is synthesized by dimer formation of glutaraldehyde molecules in alkaline pH and then its Michael addition with oleylamine. The identification of the compound is done with the help of GC-MS technique and is named as O-complex. The fluorescent property of O-complex originating from electronic transition is examined through UV-Visible absorption and PL spectroscopy.

Chapter 5 describes the synthesis of silica based magneto-fluorescent hybrid nanosystems by employing template and template-free routes. Then their detailed microstructural, surface, magnetic and fluorescent properties are studied based on different characterization results. Also, formation mechanism of the nonporous, mesoporous and microporous hybrids with radial distrinution of pore channels are proposed with schematic diagrams.

Chapter 6 has reported an intensity quantized effect in the developed hybrid nanosystems. In the emission characteristics of the hybrids, Quantum Confined Stark Effect is observed due to the local electric field induced by charge dispersion at

SiO_2/polar solvent interface. Also, enhancement in the Stark shift is observed in case of mesoporous hybrid nanosystem due to greater specific charge in these nanosystems.

MRI contrast property results of the pristine magnetic nanosystems and their hybrids with fluorescent nanosystems are analyzed in **Chapter 7**. Along with it, other potential functions of the nanosystems are explored in biomedical application to obtain multifunctionality from the systems.

The main conclusions drawn from the complete thesis work and future prospects of it are described in **Chapter 8**.

References:

[1] Lee, J. H., et al. On-demand drug release system for *in vivo* cancer treatment through self-assembled magnetic nanoparticles, *Angew. Chem.* **52** (16), 4480-4484, 2013.

[2] Kwak, G., et al. Preparation method of Co_3O_4 nanoparticles using ordered mesoporous carbons as a template and their application for Fischer-Tropsch synthesis, *J. Phys. Chem. C* **117** (4), 1773-1779, 2013.

[3] Liu, L., et al. Bio-inspired fabrication of hierarchical FeOOH nanostructure array films at the air-water interface, their hydrophobicity and application for water treatment, *ACS Nano* 7 (2), 1368-1378, 2013.

[4] Wan, L., et al. Novel hybrid organic-inorganic monolithic column containing mesoporous nanoparticles for capillary electrochromatography, *Talanta* **98** (30 August 2012), 277-281, 2012.

[5] Ebrahiminezhad, A., et al. Preparation of novel magnetic fluorescent nanoparticles using amino acids, *Colloids Surf., B* **102** (1st February), 534-539, 2013.

[6] Medarova, Z., et al. In vivo imaging of siRNA delivery and silencing in tumours, *Nature Med.* **13** (3), 372-377, 2007.

Declaration

I hereby declare that the thesis entitled "**SYNTHESIS, FUNCTIONALIZATION AND CHARACTERIZATION OF HYBRID NANOSYSTEM**", submitted to the School of Sciences, Tezpur University, in partial fulfillment of the requirements for the award of the Doctor of Philosophy in Physics, has been carried out by me at the Advanced Functional Material Research Laboratory, Department of Physics, Tezpur University, Assam, India, under the supervision of Dr. P. Deb (Research Guide). The work is original and has not been submitted in part or full in any other University or institute for any degree, diploma, associateship, fellowship or any other similar title or recognition.

Madhulekha Gogoi

Date: 7.10.2013
Place: Tezpur

(Madhulekha Gogoi)
Advanced Functional Material Research Laboratory
Department of Physics
School of Sciences
Tezpur University
Tezpur–784028, Assam, India

TEZPUR UNIVERSITY

Certificate

This is to certify that the thesis entitled "**Synthesis, functionalization and characterization of hybrid nanosystem**" submitted to the School of Sciences, Tezpur University in partial fulfillment for the award of the degree of Doctor of Philosophy in Physics, is a record of research work carried out by Ms Madhulekha Gogoi under my supervision and guidance.

All help received by her from various sources have been duly acknowledged.

No part of this thesis has been submitted elsewhere for award of any other degree.

(P. Deb)

Supervisor
Deptt. of Physics
Tezpur University

Signature of Supervisor:
Designation: Associate Professor
School: Sciences
Department: Physics
Date: 07/10/2013

I dedicate this thesis to my beloved parents

Shri Padmeshwar Gogoi and Smt. Sulekha Gogoi

Acknowledgement

It is an honour for me to express my sincere gratefulness to my research supervisor Dr. P. Deb for his constant support, training and valuable advices without which the completion of my doctoral research would not have been a reality. Particularly, his confident belief on my capability strengthened my self confidence and the lessons of punctuality and hard work learnt from him has helped me to grow in life. Working with him has been a brilliant experience that I will cherish throughout my life.

Most importantly, I would like to thank Department of Physics, Tezpur University to give me the opportunity to pursue PhD and to provide the research facilities. I would like to express my gratitude to Prof. A. J. Choudhury, Prof. A. Kumar, Prof. J. K. Sarma, Prof. N. Bhattacharya, Prof. N. Das, Dr. G. Ahmed, Dr. D. Mohanta of Dept. of Physics; Dr. A. J. Thakur of Dept. of Chemical Sciences, Dr. R. R. Haque of Environmental Science and Dr. E. Kalita of Dept. of MBBT, TU for their valuable suggestions and inspirations to carry out my research work.

I would like to thank CIF-IITG, SAIF-NEHU, CCMB, BARC, JNU and MPIE, Germany for giving us opportunity to characterize samples through advanced characterization techniques. I would like to specially thank our German collaborators Dr. A. Erbe and his group of MPIE for XPS and streaming potential measurement services, Dr. A. Kostka for HR-TEM facility; Indian collaborators Dr. A. B. Patel and his group of CCMB for MR imaging and relaxivity measurement services as well as to Dr. D. Sen of BARC for SANS and SAXS facilities. Moreover, their advices and valuable scientific discussions have gone a long way to help in understanding different aspects of material science.

It is my pleasure to express my deepest admiration and reverence to my beloved and respected parents for their limitless support and affection through my happiest and hardest times. I have been bestowed with two lovely sisters (Mrs. Ruplekha Phukan and Dr. Ashrulekha Gogoi) and their families whose love and affection have always enriched my life. In this auspicious occasion, I would like to thank Almighty to have Aditya Man Borborah in my life without whose love, inspirations and moral support I would have not been really able to stand at this point of my life. Also I would like to thank my entire family members and relatives who always wish to see me with a career of flying colors.

I owe my heartiest gratitude to my labmates Deepak, Koushik, Kakoli and Kashmiri with whom I work in a homely atmosphere in the lab and share each and everything of my research life. I would like to extend my heartful gratefulness to my entire group of friends for the inspiration and support they offered to me and for the wondrous time I spent with them. In this regard, I would specially thank to Nabanita ba and Bornali ba for giving me a wonderful time in hostel to be remembered throughout my life. Also, I would like to thank specially Sikha, Anisha, Rasna, Bondita, Prarthana, Kalpana, Anggana, Dhruba, Biswa, Sayan, Murshid, Vijay and Anup for discussing important concepts of research work as well as enjoying lots of funny and light moments and for being by my side at both grief and happiness. Special thanks to my seniors Sovan da, Somik da, Kunal da, Prakash da, Jyoti da, Ankur da, Mayuree ba, Mehmuda ba, Angshuman da and Madhurjya da for the support they offered to me whenever I approached for any kind of help required. I would also like to express my love and thankfulness to my beloved juniors Runjun, Priyanka, Pranami, Sushmita, Pawan, Samiran, Manjit, Rizwin, Nibedita, Pragyan, Jayanta, Chandranee, Parag, Jyanendra, Nomita, Nayanmoni, Saurabh and Tanvir for providing me enormous support and encouragement. Away from the laboratory, I extend my thanks to all the faculties and staffs of Dept. of Physics, TU for various assistance and help.

I would also like to thank my distant friends Angeeta, Dimpy, Tushar, Lakhi da, Prashanta, Sandeep and Nirmal for their endless support and encouragement and for providing me the inaccessible research papers at any time I requested.

Last but not the least I would like to thank entire fraternity of Tezpur University for providing all types of facilities to carry out this thesis. Also, the financial support provided by DBT, DST-INSPIRE, DAE-BRNS, Govt. of India at various stages of my PhD research is highly acknowledged.

Madhulekha Gogoi

Dated: 7.10.2013

Place: Tezpur

(MADHULEKHA GOGOI)

Contents

List of Tables

List of figures

List of abbreviations

Abbreviation	**Meanings**
AFM	atomic force microscope
APTES	aminopropyl trimethoxysilane
BE	binding energy
BET	Brunauer–Emmett–Teller
BJH	Barett-Joyner-Halenda
BSA	bovine serum albumin
CEST	chemical exchange saturation transfer
CLI	Cerenkov luminescence imaging
CMC	critical micelle concentration
C_{CTAB}	CTAB concentration
CTAB	cetyl-trimethyl ammonium bromide
DCFHDA	2′,7′-dichlorofluorescin diacetate
DCFH	2′,7′-dichlorofluorescein
DCF	2′,7′-dichlorofluorescin
DMSA	dimercaptosuccinic acid
DOT	diffuse optical tomography
EDX	energy dispersive X-ray spectroscopy
EPR	enhanced permeability and retention
fcc	face centered cubic
FC	field cooled

fct	face centered tetragonal
FDA	food and drug administration
FFT	fast Fourier transform
FOLZ	first order Laue zone
FTIR	Fourier transform infrared spectroscopy
FWHM	full width half maxima
GC-MS	gas chromatography mass spectroscopy
HOLZ	higher order Laue zone
HR-TEM	high resolution transmission electron microscope
ICP	inductively coupled plasma
JCPDS	joint committee on powder diffraction standards
LO	longitudinal-optic
LSW	Lifshitz-Slyozov-Wagner
LRP	lysine-rich protein
MRI	magnetic resonance imaging
MSA	mercaptosuccinic acid
NC size	nanocrystal size
NIR	near-infra red
PBS	phosphate buffer saline
PET	positron emission tomography
PL	photoluminescence
QD	quantum dot
QY	quantum yield

SAED	selected area electron diffraction
SAXS	small angle X-ray scattering
SOLZ	second order Laue zone
SPION	superparamagnetic iron oxide nanoparticles
TEOS	tetraethylorthosilicate
TGA	thermogravimetric analysis
THF	tetrahydrofuran
TMAOH	tetramethyl ammonium hydroxide
TRPL	time resolved photoluminescence
USANS	ultra small-angle neutron scattering
UV	ultra-violet
VEGF	vascular endothelial growth factor
VSM	vibrating sample magnetometer
XPS	X-ray photoelectron spectroscopy
XRD	X-ray diffraction
ZFC	zero field cooled

List of symbols

Symbols	**Meanings**
T_1	longitudinal relaxation time in MRI
T_2	transverse relaxation time in MRI
K	anisotropy constant
a_B	exciton Bohr radius in bulk
ε	extinction coefficient
E_g	band gap energy of bulk QD
μ	effective mass of QD
R_y	exciton Rydberg energy
ϵ'	dielectric constant
k_r	radiative rate constant
k_{nr}	nonradiative rate constant
τ	decay lifetime
T_B	Blocking temperature
k_B	Boltzmann constant
$I(q)$	scattering intensity
λ	wavelength
q	scattering wave vector
e	electronic charge
R_2	transverse relaxation rate
r_2	transverse relaxivity

Chapter 1

Introduction

Nanotechnology is an interdisciplinary area being founded on the marriage between science and technology. The outbreak of its revolutionary transformation is expected to occur in all aspects of technology dependent sectors. Due to the enhanced implementation of nanostructured materials in biomedical applications, research on the development of multifunctional nanosystem is gaining momentum since last few years. Utilizing the nanomaterials, a robust platform, referred to as hybrid nanosystem, can be designed by incorporating multiple components in a nanoassembly.

1.1 Multifunctionality:

The hybrid nanosystems are multifunctional in the meaning that they can deliver more than one function synergistically. The concept of hybrid system has been actualized and then became popular from last few years [1,2]. For instance, the therapeutic application is a combination of functionalities viz. detection, targeting and delivery which can be brought about by an efficient multifunctional nanosystem. Figure 1.1 shows the schematic of a multifunctional hybrid nanosystem.

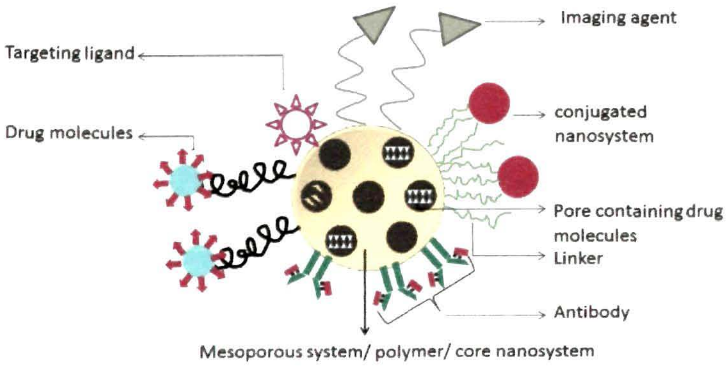

Figure 1.1: Schematic diagram of a multifunctional hybrid nanosystem

1.1.1Imaging functionalities of hybrid nanosystem:

The hybrid nanosystems can be developed to function as imaging probes in biomedical applications. Considering the multi-modal imaging prospect for detection, the probes can be classified as:

1.1.1.1Nuclear-optical dual imaging:

It consists of a radioactive component useful for positron emission tomography (PET) and a fluorescent component for optical imaging. An example of this kind is composed of quantum dot (QD) with near-infrared (NIR) fluorescence and a chelating agent to bind radioactive nuclei ^{64}Cu for PET imaging and to a vascular endothelial growth factor (VEGF) protein [3].

1.1.1.2 Cerenkov luminescence imaging (CLI):

Cerenkov radiation occurs when a charged particle travels faster than light in an insulating medium and in multimodal strategy acts as an energy donor for the adjacent fluorophore. A combination of PET isotope and QDs can be excited by a wide range of wavelengths and produce fluorescent light with high Stokes-shift [4].

1.1.1.3 Magneto fluorescent imaging:

The superparamagnetic and fluorescent nanoparticle combination provides simultaneous anatomic imaging and real time monitoring of molecular targeting through magnetic resonance (MR) and optical imaging respectively. Enhanced biomedical imaging of diseased cells can be realized through this magnetic resonance (MR) and optical imaging. An excellent example of such multifunctional nanosystem having tremendous potential in biomedical imaging has been reported by Medarova et al. in 2007 [5].Their system consists of a magnetic nanoparticle labeled with an NIR fluorescence dye and covalently linked therapeutic agent siRNA such that *in vivo* transfer of siRNA and its simultaneous accumulation in tumors can be probed by optical and magnetic resonance (MR) imaging respectively.

1.1.1.4 Non-Nanoparticulate Chemical-Exchange Saturation Transfer (CEST) Agents for MR imaging:

An MRI contrast scheme relying upon a novel contrast agent known as chemical exchange saturation transfer (CEST) has been developed recently. These contrast agents can vary the signal of water protons through chemical exchange sites on the agent via saturation transfer [6]. In 2007, Gilad et al. have reported a non-metallic, bio-degradable, lysine-rich protein (LRP) receptor, expressing frequency selective contrast [7]. Depending on the transfer of radiofrequency labeling from the receptor's amide protons to water protons, the contrast can be switched 'on' and 'off'.

1.2Delivery of multifunctional hybrid nanosystem to target:

For therapeutic applications, the multifunctionality of nanosystem lies in bringing together the targeting, delivery of an active agent and imaging for both detection and visualization of delivery. Hence combination of biological entities brings off target-specific imaging and drug delivery with the multifunctional nanosystem. Different aspects of targeting are described below:

• *1.2.1 Passive targeting:*

It is the accumulation of the nanoparticles within the tumor matrix by enhanced permeability and retention (EPR), caused by leakiness of the tumor vasculature combined with poor lymphatic drainage [8]. This kind of targeting is dependent on the nanoparticle circulation time which in turn is a function of nanoparticle size [9]. To increase vascular permeability of nanoparticles, several strategies showed potency like administrating different agent for disruption of endothelial cellular function or vasoconstrictor infusion [10].

1.2.2 Active targeting:

Functionalization of nanoparticles with targeting ligands which can bind to its counterparts expressed on the target cells can prove to be valuable where EPR effect is not exhibited [11].

1.2.3 New targeting strategy:

A novel kind of targeting uses the pH-sensitive drug release from the multifunctional nanoparticles. The microenvironment of tumor becomes acidic due to increased glycolysis and reduced use of oxidative phosphorylation leading to increased level of lactic acid and low extracellular pH [12]. Iron oxide nanoparticles stabilized with PAMAM dendrimer and loaded with anticancer drug, DOX, through acid cleavable hydrazone bonding, can be used as a pH-responsive drug release system [13].

1.3 Synthetic approaches of multifunctional nanosystem:

The synthetic approaches for developing multifunctional nanosystem can be broadly divided into three general categories:

1.3.1 Encapsulation:

This general strategy works by filling matrix particles, which have channels of appropriate pore sizes, with different preformed nanoparticles. It can again be subdivided into two aspects —

1.3.1.1 Silica based:

In this approach, mesoporous or microporous silica particles are synthesized by following Stöber method, modified Stöber method or reverse microemulsion method [14, 15, 16]. The already synthesized nanoparticles are loaded in the mesopores of silica during its synthesis itself [17]. The stable conjugation is obtained through electrostatic force of attraction between silica and nanoparticle surface (schematic in Figure 1.2).

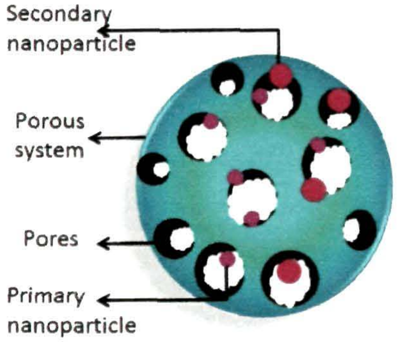

Figure 1.2: Schematic diagram of mesoporous silica encapsulation method of nanohybrid synthesis

1.3.1.2 Polymer based:

The encapsulating materials that have been generally used for this purpose ranges from natural polymers to synthetic organic/inorganic molecules [18-19]. In this approach, polymer spheres of size 50-500 nm are prepared, the hollow core of which are large enough to accommodate more than one kind of nanoparticles by simple mechanical stimulation viz. sonication, stirring etc. The working force behind stable conjugate formation is again electrostatic force of attraction. Recently, to avoid any possible quenching of individual property of the nanoparticles due to conjugation, preparation strategies are applied so that different kind of nanoparticles are remained spatially separated from each other within nanocapsules [20]. Figure 1.3 shows the schematic diagram of a hybrid of dendrimer capped core nanosystem.

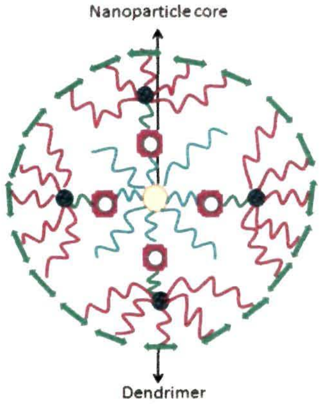

Figure 1.3: Schematic diagram of dendrimer based synthesis of hybrid

1.3.2 Direct conjugation:

In this procedure, nanoparticles functionalized with different functional groups can be linked covalently to form the hybrid [21]. If direct reaction between functional groups cannot take place, then by adding cross-linkers or spacers, this kind of conjugation is performed [22]. Figure 1.4 is the schematic diagram of such assembly.

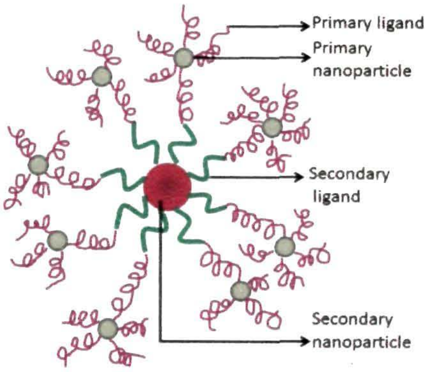

Figure 1.4: Schematic diagram of direct conjugation method of hybrid synthesis

1.3.3 Inorganic synthesis:

Inorganic nanoparticles made of different phases of different materials are formed by direct chemical synthesis route. Heterodimer nanoparticles of magnetic and semiconductor materials have been developed by a one-pot chemical synthesis method by taking advantage of lattice mismatching and selective annealing at a relatively low temperature [23]. Similarly, FeCo/graphitic-shell nanocrystals of advanced magnetic and optical properties have been synthesized by a scalable chemical vapour deposition method and explored for potential use for integrated diagnosis and therapeutic applications [24].

1.4 Magnetic imaging:

Basic principle of use of magnetic nanoparticles as contrast agent in MRI technique:

Magnetic Resonance Imaging (MRI) is a noninvasive medical imaging technique used to visualize internal structures of the body in detail. The MR image is the map of very weak magnetization, originated from some of the atomic nuclei in the body tissue, in the presence of an external magnetic field [25]. The potential of Magnetic Resonance Imaging (MRI) lies in the intrinsic contrast between tissues that it produces in the image. The contrast arises due to the signal intensity difference between adjacent pixels in the image and it results mainly because of the differences in the T_1 and/or T_2 relaxation times of the tissues under observation. Hence, the contrast between pathologic and normal tissue in MRI image depends completely on differences in T_1 and T_2. To have an MRI image with sharp contrast between normal and pathogenic tissue, contrast agents are administered to increase this signal intensity difference [26]. MRI contrast agents are indirect agents in the sense that they are not imaged directly, but affect T_1 or T_2 of the water protons in the tissue around them. Shortening of T_1 leads to increase in signal intensity while shortening of T_2 produces broader lines with decreased intensity. The ultimate result is a nonlinear relationship between signal intensity and contrast agent concentration [27]. The concentrated T_1 agents shorten T_2 times and diluted T_2 agents shorten T_1 times.

1.4.1 T_1 agents:

T_1 is the time required for the z component of magnetization to return to two third of its original value following an excitation pulse [25]. By this relaxation, the excited protons give up their energy to the surrounding lattice to return to their original orientation. T_1 contrast agents work as relaxation sinks for water protons. One important example of it is paramagnetic metal ions chelated with organic ligands, addressing less toxicity effect. Gadolinium-DTPA complex, a renally excreted chelate was approved by Food and Drug Administration of USA for clinical use in mid-1988 [27]. The compact chelate molecules reduce the free space in the coordination sphere. Because of this the large molecules, e.g. fat, cannot come close to the metal ions for efficient energy transfer. But the tissue water can easily diffuse into the vicinity of metal ions, relax and exchange with bulk tissue water. This process is very fast (~10^6 times per sec) and therefore, the tissue water near the contrast agent has a larger net magnetization than the neighboring tissue and will appear brighter in the MRI image [25].

1.4.2 T_2 agents:

T_2 is the time required for the magnetization in xy plane to return to one third of its original value via irreversible process [25]. Initially, magnetization orients only in z direction; but with absorption of 90° radiofrequency pulse, it rotates entirely into the xy plane. T_2 is also known as transverse relaxation or spin-spin relaxation process. The latter refers to the energy transfer from an excited proton to another nearby proton [25]. One very common kind of agents under this category is superparamagnetic iron oxide nanoparticles (SPION), consists of ultrafine iron oxide nanoparticles with large magnetic moment and zero remnant magnetization. The nanoparticles are generally encapsulated with inert materials to address the biocompatibility issue. The large magnetic moment of the molecules distorts the local magnetic field in the vicinity of the agent, causing the adjacent water protons to dephase more rapidly than the surrounding tissue [25]. This results into significant signal loss in T_2-weighted spin-echo images. These agents are taken up by the normal tissue and produce low intensity T_2-weighted image while the lesions that do not absorb the agents appear with dark contrast than the earlier one.

1.5Optical imaging:

Basic principle of use of fluorescent material for optical imaging:

Optical imaging is based on the absorption of light by endogenous or exogenous chromophore resulting into a contrast between diseased and normal surrounding tissue. Because of its capacity for wide range of spatial imaging from cells to organ systems, it has evolved out as an important technology for medical imaging. Based on contrast agent type, optical imaging technology can be classified as follows:

1.5.1 Endogenous optical contrast agent:

Due to the interaction of light with biological tissue, number of phenomena arise viz. scattering, absorption etc. Mie scattering governs the scattering phenomenon in tissue and the intensity of Mie scattered radiation is a function of wavelength and tissue morphology [28]. Hence, change in size of the major scatterers in tissue can be distinguished in pathogenic tissue from the healthy ones. By the phenomenon of absorption, variations in total saturation of endogenous chromophores like oxyhemoglobin, deoxyhemoglobin, melanin, myoglobin etc. can be inferred. The excited chromophores relax by releasing their energy in the form of heat or by a radiative decay.

Some fluorophores present in tissue like amino acids (phenylalanine, tyrosine, tryptophan etc.) emit light of different wavelength after photon absorption – a phenomenon known as tissue autofluorescence [29]. It is used to understand the basic mechanisms of molecular interactions and signaling processes under their native conditions [29]. The emitted fluorescence are obtained from one and two-photon confocal microscopy [30] as well as with diffuse spectroscopy [31].

1.5.2 Exogenous optical contrast agent:

Commonly used exogenous contrast agents are fluorescent molecules, fluorescent proteins and nanoparticles [29]. Among them, the nontargeted contrast agents concentrate in tumors by passive targeting as explained in section 1.2.1. To overcome the shortcomings of low selectivity for tumors where EPR effect does not work, targeted contrast agents are designed. For that, first of all biomarkers are identified such as over expressed proteins or enzymes in the tumor and their counter molecules to bind with them. After that the targeting molecules are attached to the contrast agent to make them targeted. Exogenous contrast agents emitting in the visible range are mainly used for superficial tissue imaging as these are associated with background tissue autofluorescence signal while the NIR probes are used for deep tissue imaging [32].

1.6 Aspects of literature review and objective of thesis:

The literature review presented above is a detailed description on multifunctional hybrid nanosystem development and some of their uses in biomedical applications. Hybrids are basically hierarchical structures built on nanoscale units. The understanding of hierarchical structure and physical properties of the multifunctional nanosystems is of immense importance for assuring its best application. During this literature search, I was inclined to develop silica based magneto-fluorescent hybrid nanosystem for (i) the efficacy of magneto-fluorescent hybrid nanosystem as imaging probe, described under subheading 1.1.1.3; and (ii) for the FDA acceptance of the biocompatibility of silica as "Generally Recognized as Safe" (GRAS) [33]. Additionally, the silica coating prevents free ions release from the nanoparticles and creates suitable sites for biofunctionalization. By simple variation of precursor concentration and reaction conditions, silica encapsulation of different morphology and mesopore structure can be obtained [34].The most important objective of multimodal probe is the retention of their dual imaging property execution after conjugate formation [35] which remains intact in case of silica encapsulation. Sometimes, deviations from the original properties of the pristine components are observed in case of silica conjugation [36,37,38]. Valid explanations are being forwarded in those regards. Following these facts, I became motivated to develop pristine magnetic, fluorescent nanoparticles as well as silica based magneto-fluorescent hybrid nanosystems through templated and non-templated methods and carry out a detailed microstructural, optical and magnetic property study of them. By varying the fluorescent components, different combinations of hybrids are developed. I have sought a deeper insight into the above mentioned properties of the nanosystems. Moreover, developing multifunctional nanosystem through a simple, one-pot procedure rather than the long, multi-step processes is also explored. The multifunctional applicability of the developed systems is examined in their respective fields. Also. quantum confinement effect exhibited by the hybrids is studied in the thesis work.

Materials that I have synthesized are:

1. Magnetic nanoparticles: iron oxide and iron platinum
2. Fluorescent nanoparticles: CdTe quantum dots, oleylamine based organic dye
3. Hybrid system: Silica based magneto-fluorescent system, FePt based single moiety, multifunctiuonal system.

The applicability of the systems is appraised as MRI contrast agent, therapeutic agent and as drug-protein loading vehicle.

References:

[1] Holtz, J. H. and Asher, S. A., Polymerized colloidal crystal hydrogel films as intelligent chemical sensing materials, *Nature* **389** (6653), 829-832, 1997.

[2] Yin, Y., et al. Template-assisted self-assembly: a practical route to complex aggregates of monodispersed colloids with well-defined sizes, shapes and structures, *J. Am. Chem. Soc.* **123** (8), 8718-8729, 2001.

[3] Kobayashi, H., et al. Dual-modality optical and positron emission tomography imaging of vascular endothelial growth factor receptor on tumor vasculature using quantum dots, *Eur. J. Nucl. Med. Mol. Imaging* **35** (12), 2235-2244, 2008.

[4] Dothager, R. S., et al. Cerenkov radiation energy transfer (CRET) imaging: a novel method for optical imaging of PET isotopes in biological systems, *PLoS One* **5** (10), e13300 (1-7), 2010.

[5] Medarova, Z., et al. In vivo imaging of siRNA delivery and silencing in tumours, *Nature Med.* **13** (3), 372-377, 2007.

[6] Terreno, E., et al. Encoding the frequency dependence in MRI contrast media: the emerging class of CEST agents, *Contrast Media Mol. Imaging* 5(2), 78-98,2010.

[7] Gilade, A. A., et al. Artificial reporter gene providing MRI contrast based on proton exchange, *Nature Biotech.***25** (2), 217-219, 2007.

[8] Cheng, Z., et al. Multifunctional nanoparticles: cost versus benefit of adding targeting and imaging capabilities, *Science***338** (6109), 903-910, 2012.

[9] Danhier, F., Feron, O. and Préat, V. To exploit the tumor microenvironment: passive and active tumor targeting of nanocarriers for anti-cancer drug delivery, *J. Control. Release* **148** (2), 135-146, 2010.

[10] Chrastina, A., et al.Overcoming *in vivo* barriers to targeted nanodelivery, *Wiley Interdiscip. Rev. Nanomed .Nanobio technol.*3 (4), 421-437, 2011.

---

[11] Hrkach, J., et al. Preclinical development and clinical translation of a PSMA-targeted docetaxel nanoparticle with a differentiated pharmacological profile, *Sci. Trans. Med.* **4** (128), 128ra39(1-11), 2012.

[12] Crayton, S. H. and Tsourkas, A. pH-titrat able superparamagnetic iron oxide for improved nanoparticle accumulation in acidic tumor microenvironments, *NANO* **5** (12), 9592-9601, 2011.

[13] Chang, Y., et al. Novel water-soluble and pH-responsive anticancer drug nanocarriers: doxorubicin-PAMAM dendrimer conjugates attached to superparamagnetic iron oxide nanoparticles (IONPs), *J. Coll. and Interf. Sci.* **363** (1), 403-409, 2011.

[14] Stöber, W. and Fink, A. Controlled growth of monodisperse silica spheres in the micron size range, *J. Colloid Interface Sci.* **26** (1), 62-69, 1968.

[15] Bogush, G. H., Tracy, M. A. and Zukoski IV, C. F. Preparation of monodisperse silica particles: Control of size and mass fraction, *J. Non-Crystl.Solids***104** (1), 95-106, 1988.

[16] He, D. G., et al. A facile route for shape-selective synthesis of silica nanostructures using poly-L-lysine as template, *Chin. Chem. Lett.***24** (2), 99-102, 2013.

[17] Wan, L., et al. Novel hybrid organic-inorganic monolithic column containing mesoporous nanoparticles for capillary electrochromatography, *Talanta* **98** (30 August 2012), 277-281, 2012.

[18] Chelebaeva, E., et al. Nanoscale coordination polymers exhibiting luminescence properties and NMR relaxivity, *Nanoscale* **3** (3), 1200-1210, 2011.

[19] Lu, G., et al. Imparting functionality to a metal-organic framework material by controlled nanoparticle encapsulation, *Nat. Chem.* **4** (4), 310-316, 2012.

[20] Chu, M., et al. Preparation of quantum-dot coated magnetic polystyrene nanospheres for cancer cell labelling and separation, *Nanotechnology* **17** (13), 3268-3273, 2006.

[21]Ebrahiminezhad, A., et al. Preparation of novel magnetic fluorescent nanoparticles using amino acids, *Colloids Surf., B***102** (1st February), 534-539, 2013.

[22] Das, M., et al. Bio-functionalization of magnetite nanoparticles using an aminophosphonic acid coupling agent: new, ultradispersed, iron-oxide folate

nanoconjugates for cancer-specific targeting, *Nanotechnology* **19** (41), 415101 (1)-415101(14), 2008.

[23] Gu, H., et al. Facile one-pot synthesis of bifunctional heterodimers of nanoparticles: A conjugate of quantum dot and magnetic nanoparticles, *J. Am Chem Soc.***126** (18), 5664-5665, 2004.

[24] Seo, S. W., et al. FeCo/graphitic-shell nanocrystals as advanced magnetic-resonance-imaging and near-infrared agents, *Nat. Mater.***5** (12), 971-976, 2006.

[25] Panepucci, H. and Tennús, A., Magnetic Resonance Imaging Tutorial I, Instituto de Física de São Carlos – Universidade de São Paulo – USP, Department de Física e Informática, São Carlos – SP – Brasil, 1994.

[26] Brown, M. A. and Semelka, R. C. *MRI Basic Principles and Applications,* Wiley-LISS, New Jersy, 2003.

[27] Volkov, A. Contrast agents in magnetic resonance imaging, www.cc.utah.edu/~av6a51/mri.htm, 1997.

[28] Wang, L. V. and Wu, H.I. *Biomedical Optics: Principles and Imaging,* Wiley Interscience, Hoboken, 2007.

[29] Berezin, M. Y. and Achilefu, S. Fluorescence lifetime measurements and biological imaging, *Chem. Rev.* **110** (5), 2641-2684, 2010.

[30] Richards-Kortum, R. and Sevick-Muraca, E. Quantitative optical spectroscopy for tissue diagnosis, *Annu.Rev. Phys. Chem.***47**, 555-606,1996.

[31]Soliman, H., et. al. Functional imaging using diffuse optical spectroscopy of neo adjuvant chemotherapy response in women with locally advanced breast cancer, *Clin.Cancer Res.* **16** (9), 2605-2614, 2010.

[32] Solomon, M., et. al. Optical Imaging in Cancer Research: Basic Principles, Tumor Detection, and Therapeutic Monitoring, *Med.Princ.Pract.* **20** (5), 397-415, 2011.

[33] Lee, J. E., Lee, N., Kim, T., Kim, J. and Hyeon, T. Multifunctional mesoporous silica nanocomposite nanoparticles for theranostic applications, *Acc. Chem. Res.***44** (10), 893-902, 2011.

[34] Zhang, H., et al. Facile synthesis of monodisperse microspheres and gigantic hollow shells of mesoporous silica in mixed water-ethanol solvents, *Langmuir* **23** (3), 1107-1113, 2007.

[35]Koktysh, D., Bright, V. and Pham, W. Rapid turnaround scanning probe Nanolithography, *Nanotechnology* **22** (27), 275606(1)-275606(7), 2011.

[36] Salgueiriño-Maceira, V., et al. Composite Silica Spheres with Magnetic and Luminescent Functionalities, *Adv. Funct.Mater.* **16** (4), 509-514, 2006.

[37] He, R., et al. Core/shell fluorescent magnetic silica-coated composite nanoparticles for bioconjugation, *Nanotechnology* **18** (31), 315601(1)-315601(7), 2007.

[38] Wolcott, A., et al. Silica-coated CdTe quantum dots functionalized with thiols for bioconjugation to IgG proteins, *J. Phys. Chem. B***110** (11), 5779-5789, 2006.

Chapter 2

Experimental details

2.1 Materials used:

Following chemicals were used during the entire study of the experiments. All are commercially available with reagent grade and were used without further purification

1. Stearic acid [$C_{18}H_{36}O_2$]
2. Iron (III) nitrate 9-hydrate [$Fe(NO_3)_3.9H_2O$]
3. Tetrahydro furan [$C_4H_4O_5$]
4. Ascorbic acid [$C_6H_8O_6$]
5. Disodium platinum hexachloride [$Na_2PtCl_6.6H_2O$]
6. Sodiumboro hydride [$NaBH_4$]
7. Tetramethyl ammonium hydroxide [$N(CH_3)_4^+OH^-$]
8. 2′,7′-dichlorofluorescin diacetate [$C_{24}H_{16}Cl_2O_7$]
9. Sodium hydroxide [NaOH]
10. Phosphate buffer [$C_6H_8O_6$]
11. Tris-HCl buffer
12. Hydrogen peroxide [H_2O_2]
13. Cadmium chloride [$CdCl_2$]
14. Sodium tellurite [Na_2TeO_3]
15. Mercapto succinic acid [$C_4H_6O_4S$]
16. Borax [$Na_2B_4O_7.10H_2O$]
17. Manganese chloride [$MnCl_2$]
18. Rhodamine 6G
19. Oleylamine [$C_{18}H_{37}N$]
20. Glutaraldehyde [$C_5H_8O_2$]
21. Ethanol [C_2H_5OH]
22. Cetyl-trimethyl ammonium bromide [$C_{19}H_{42}BrN$]
23. Tetraethylorthosilicate [$SiC_8H_{20}O_4$]
24. Ammonia solution 25% [NH_4OH]
25. Aminopropyl trimethoxysilane [$C_9H_{23}NO_3Si$]
26. Dimercapto succinic acid [$C_4H_6O_4S_2$]
17. Bovine serum albumin
18. Citric acid [$C_6H_8O_7$]

2.2 Synthesis techniques:

Iron oxide nanoparticles

- Thermal decomposition of iron nitrate 9-hydrate
- Phase change by ligand addition

Iron platinum nanoparticles

- Facile, one-pot, aqueous chemical route

Pristine and Manganese doped Cadmium telluride quantum dot

- Colloidal synthesis: size tuning by refluxion

Organic fluorescent dye

- Schiff base formation

Silica based Magneto-fluorescent hybrid

- Template-free method
- Templated method

2.3 Analytical equipment:

1. **X-ray diffractometry:** The phase composition of the nanoparticles were examined by powder X-ray diffraction analysis (Rigaku diffractometer with CuKα radiation).

2. **UV-Visible absorption:** The optical properties were studied by UV-Visible absorption spectrometry (Shimadzu, UV-2450).

3. **PL spectroscopy:** The emission properties were measured by PL spectroscopy (Perkin Elmer, LS55).

4. **Fourier Transform Infra-red spectroscopy:** The surface functionalities of the nanoparticles were examined by FTIR spectroscopy (Nicolet Impact I-410).

5. Transmission Electron Microscopy: The microstructural properties were studied by high resolution TEM and associated selected area diffraction (SAED) method (Jeol JSM-2200FS operated at 200KV)

6. Scanning Electron Microscopy: Scanning Electron Microscopy was done on JEOL 6390 LV operated at 30 KV.

7. EDX: The compositional characterizations were done with energy dispersive X-ray microanalysis (EDX 7582, Oxford Instrument, UK).

8. Vibrating sample magnetometer: The magnetic characterization was done with vibrating sample magnetometer (Lakeshore 7410).

9. Atomic Force Microscopy: AFM study has been performed in tapping mode using Nanonics Multiview 2000.

10. Fluorescence Microscopy: The fluorescence images were taken by a fluorescence microscope (LEICA DMI6000B).

11. Thermogravimetric analysis: TGA was performed with TGA-50 (Shimadzu).

12. Gas Chromatograpy Mass spectroscopy: Unknown compound was identified with GC-MS scpectroscopy (Perkin Elmer).

13. ICP-OES: The compositions were determined with the help of ICP-OES (Perkin Elmer).

14. Streaming potential measurement: The surface charge of the nanoparticles were determined by using the charge titration system stabilizer (Particle Metrix GmbH, Germany).

15. X-ray Photoelectron Spectroscopy: The compositions and surface characteristics were measured by X-ray photoelectron spectroscopy (XPS, Quantum 2000, Physical electronics, USA). For XPS analysis, particle dispersions were placed on a freshly cleaned silicon wafer and the solvent was evaporated. The spectra were measured using a monochromatic Al Kα source (hν = 1486.6 eV) at 45° take off angle and pass energies of 23.5 eV and 93.9 eV for the high resolution and survey spectra, respectively Calibration of the binding energy (BE) of the measured spectra was performed at the C1s peak of the adsorbed hydrocarbons (BE = 285 eV) as internal reference.

16. SAXS: SAXS experiments have been performed using the SAXS goniomter mounted on a rotating anode X-ray source at Bhabha Atomic Research Centre, Trombay.

17. SANS: SANS experiments have been performed using a double crystal-based small-angle neutron scattering instrument at the Guide Tube Laboratory of Dhruva reactor. BARC, Trombay.

18. MRI: Contrast agent efficiency of magnetic nanoparticles for MRI application has been tested both *in vivo* and *in vitro* using Wide Bore 600 MHz (14T) NMR Micro-imaging and Spectroscopy facility in CCMB, Hyderabad.

19. NMR: Unknown compound identification is done by NMR spectroscopy (Jeol, 400 MHz).

Chapter 3

Magnetic nanoparticles

3.1 Introduction:

Magnetic materials find a wide range of applications in many present day technologies. While the permanent magnets are used in industrial applications, the soft magnetic materials, with high saturation magnetization, larger permeability and very small energy dissipation are used in telecommunication and electronics [1]. Nanosized magnetic particles have come forth as versatile materials for different applications with better efficiency than their bulk counterparts. Magnetic nanoparticles with high remanence magnetization find applications in magnetic storage [2] while the superparamagnetic nanoparticles i.e. with zero remanence and coercivity, are the most suitable candidate for biomedical application [3]. Magnetic nanoparticles have been prepared by variety of methods viz. sonochemical reactions [4], hydrothermal synthesis [5], thermolysis of precursors as well as coprecipitation technique [6]. In this study, the stearic acid capped iron oxide nanoparticles are synthesized by a non-aqueous, thermal decomposition method [7] and the ascorbic acid capped iron platinum nanoparticles by a simple, one-pot, aqueous method [8].

3.2 Superparamagnetic nanoparticles:

Coercivity of magnetic nanoparticles is an important characteristic as depending on it, application of magnetic nanoparticles vary from field to field. The coercivity of fine particles is dependent on their size [9].

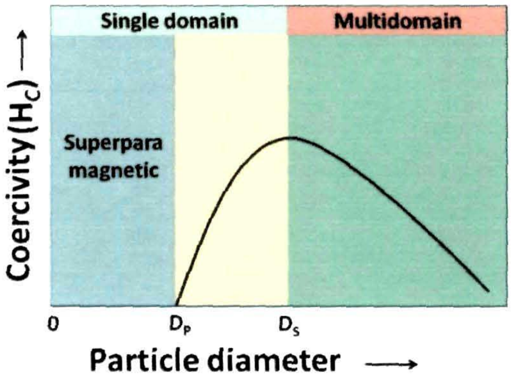

Figure 3.1 Variation of coercivity with particle diameter.

As depicted in Figure 3.1, below a critical diameter (D_P), the coercivity becomes zero because of thermal effects, which can spontaneously demagnetize a previously saturated assembly of particles. Such particles are known as superparamagnetic particles.

To illustrate the phenomenon let us consider, an assembly of uniaxial, single-domain particles, each with energy density, $E=K \sin^2\theta$, where, K is the anisotropy constant and θ the angle between M_S and the easy axis. Then according to Néel-Arrhenius Law, the relaxation time is given by an equation of the form: $\tau=\tau_0 \exp (KV/K_BT)$ [10], where, V is the volume of each particle, K_B is the Boltzmann constant and T is temperature. Now for reversing its magnetization, the energy barrier that has to be overcome is $\Delta E=KV$. According to Néel, if single-domain particles become small enough, KV would become so small that thermal fluctuations could overcome the anisotropy forces and spontaneously reverse the magnetization of a particle from one easy direction to the other, even in the absence of an applied field. Hence, paramagnetic behavior is exhibited by the particle assembly; the applied magnetic field will tend to align the moments of the particles, whereas thermal energy will tend to break the alignment in them. However, because of the enormously higher magnetic moment associated with a particle consisting of no of atoms than the magnetic moment per atom of normal paramagnetic atom or ion, the former is termed as superparamagnetic.

Part A

3.3 Synthesis of iron oxide nanoparticles:

For developing the iron oxide nanoparticles, a method that has been used by our group since long, is applied with slight modification [11]. Briefly, 0.7932 gm (2.8 mmole) of stearic acid is taken in a 20 ml beaker and heated to melt at 70°-80° C. Then 1 gm (2 mmole) of $Fe(NO_3)_3.9H_2O$ are added to it in stepwise fashion and the temperature is raised to 125°C with mechanical stirring. The motivation behind increasing the stearic acid content in the synthesis technique is to obtain particles with lower dimension. Heating is continued till evolution of brown fumes of NO_2 gas stops indicating completion of decomposition process. A dark brown viscous mass is obtained which is allowed to cool for 24 hrs. The solid material is crushed down to fine powders and treated with tetrahydrofuran of a volume four times more than that of the bed volume of the powder. The purification with THF and subsequent centrifugation is done 2-3 times to remove excess stearic acids and undecomposed iron precursor. The precipitate is dried in hot air oven at 70°C and then heat treated at 250°C with 30 min holding, in a tube furnace to obtain the nanoparticles.

3.4Surface modification of stearic acid capped iron oxide nanoparticle:

Surface modification by dimercapto succinic acid (DMSA) addition over iron oxide nanoparticles is done by a direct method [7]. For that 20mg of stearic acid capped iron oxide nanoparticles are mixed with 5 ml of water by sonication and 4.5 mg of DMSA with another 5 ml of water by stirring. Both are mixed and kept for overnight standing. Then the mixture is sonicated for 3 X 15 min and pH adjustment is done with tetramethyl ammonium hydroxide (TMAOH) from pH 4.06 to 11. Again it is adjusted to physiological pH with 0.6 M HNO_3. The mixture is sonicated for 24 hrs using a bath sonicator and then centrifuged. The obtained precipitate is dried in oven and is found to form stable aqueous dispersion in the whole pH range.

3.5 Results and discussion:

The microstructural characterization results of the two samples are presented in Figure 3.2. From the XRD pattern of the two samples, two prominent peaks are identified as the peaks corresponding to the planes (311) and (440) of maghemite (γ-Fe_2O_3) phase at $2\theta \sim 35.6°$ and $62.9°$ respectively [JCPDS File no. 89-5892] [Figure 3.2 (a) and (b)]. Moreover, some low intensity peaks are observed at $2\theta \sim 30°$, $43°$, $53°$ and $56°$ for the magnetite (Fe_3O_4) phase which are indicated by black squares in the figure [JCPDS File no. 89-0950]. The average crystallite sizes are determined by a pattern decomposition procedure using a pseudo-Voigt profile shape function and subsequent single-line analysis, based on the equivalent Voigt representation, and found to be ~ 2.8 nm. From the M-H plot of Figure 3.2 (c) and (d), it is observed that the iron oxide nanoparticles are superparamagnetic in nature and the surface modification has not caused any alteration to the magnetic property. The HRTEM images presented in Figure 3.2(e) and (f) show the spherical morphology of both the stearic acid capped and DMSA functionalized iron oxide nanoparticles. Almost similar average particle size for both the samples (~ 3 nm) is observed from the size distribution plot of the TEM images. However, the particle distribution has been changed on surface modification as the DMSA molecules become interlinked with neighboring molecules through disulfide bond formation whereas this favors the stability of the colloidal dispersion [12]. The EDX patterns of both the SPIONs are presented in Figure 3.2(g) and (h). The EDX pattern of stearic acid capped SPION [Figure 3.2(g)] clearly shows the presence of only Fe, O and C in the sample without any impurity peak while that of DMSA modified SPION [Figure 3.2(h)] shows the presence of S in the sample along with the other elements after surface modification with DMSA. The Pt peak is coming from the coating over the sample for EDX study.

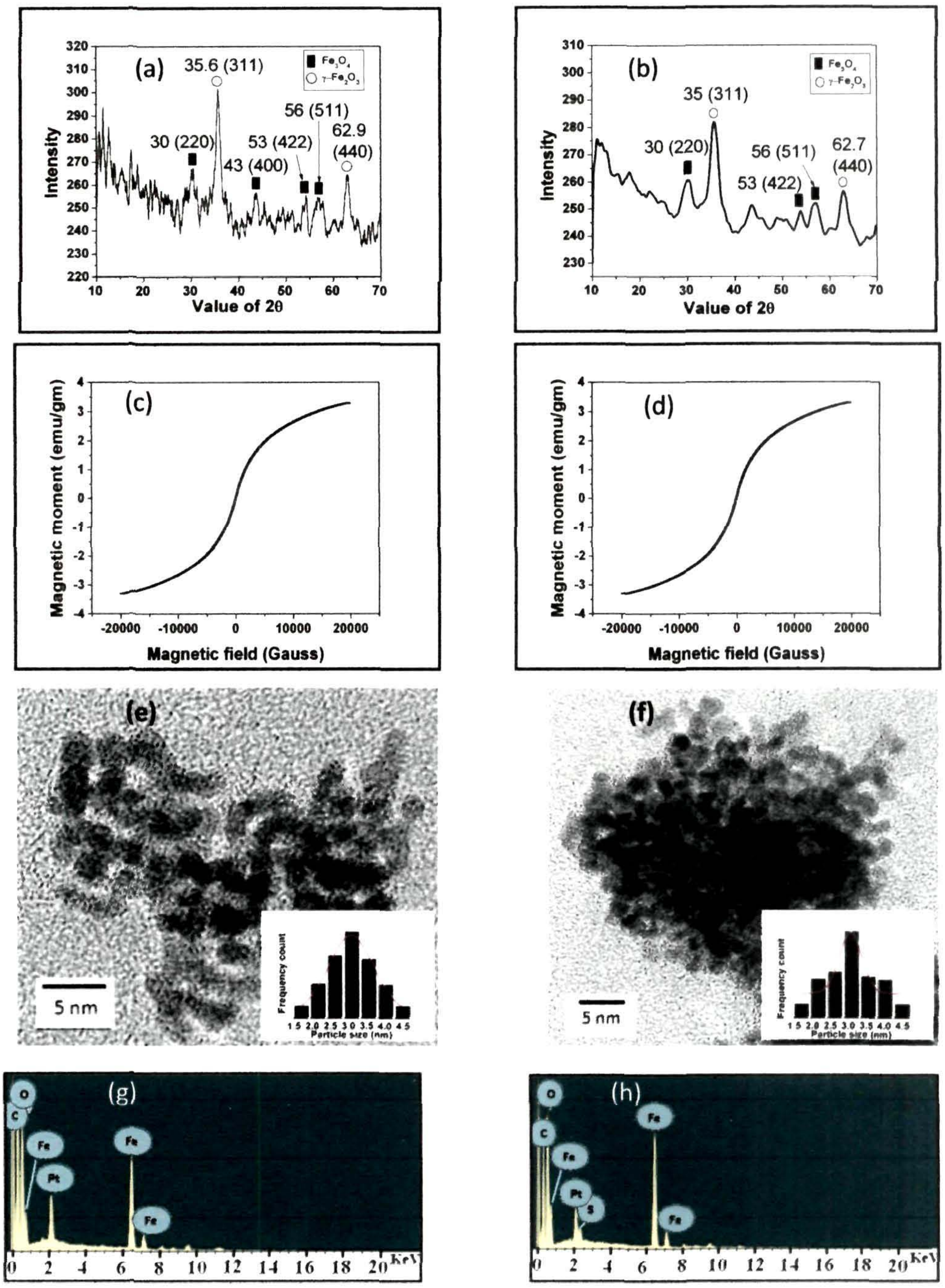

Figure 3.2 XRD patterns (a) and (b), VSM curves (c) and (d), HRTEM images (e) and (f), EDX patterns (g) and (h) of stearic acid capped and DMSA functionalized SPIONs respectively.

To investigate the surface functionalities before and after surface modification, XPS characterization is carried out with both SPIONs. Figure 3.3 presents the C1s, O1s and Fe2p XPS spectra for stearic acid capped SPION sample. Figure 3.3 (a) shows a composition of the C1s peak, where 3 different components are present. Aliphatic carbon from stearic acid is present at 285 eV [13]. Two peaks at higher binding energies, 286.6 eV and 288.3 eV are for the carbon atoms of –C-O group and for COO^- or COOH groups respectively [14-15]. The O1s region contains two components which are easily distinguishable; among them the peak at 530.1 eV is due to oxygen bound to Fe atoms as oxide [16] [Figure 3.3 (b)]. Another peak at 531.5 eV is due to the presence of –OH groups [16] which may come from the iron oxyhydroxides (FeOOH) as by thermal decomposition of $Fe(NO_3)_3.9H_2O$, initially FeOOH is formed which later yields maghemite phase of iron oxide on heat treatment. The XPS spectra of Fe 2p peak shown in Figure 3.3 (c) gives the evidence of presence of $Fe2p_{3/2}$ peak at 710.8 eV [17] along with satellite peaks at 713.5 eV [18] and 719.4 eV [19]. Besides the presence of $Fe2p_{1/2}$ peak at 724.6 eV point towards the Fe^{3+} state of γ-Fe_2O_3 phase in the sample [20].

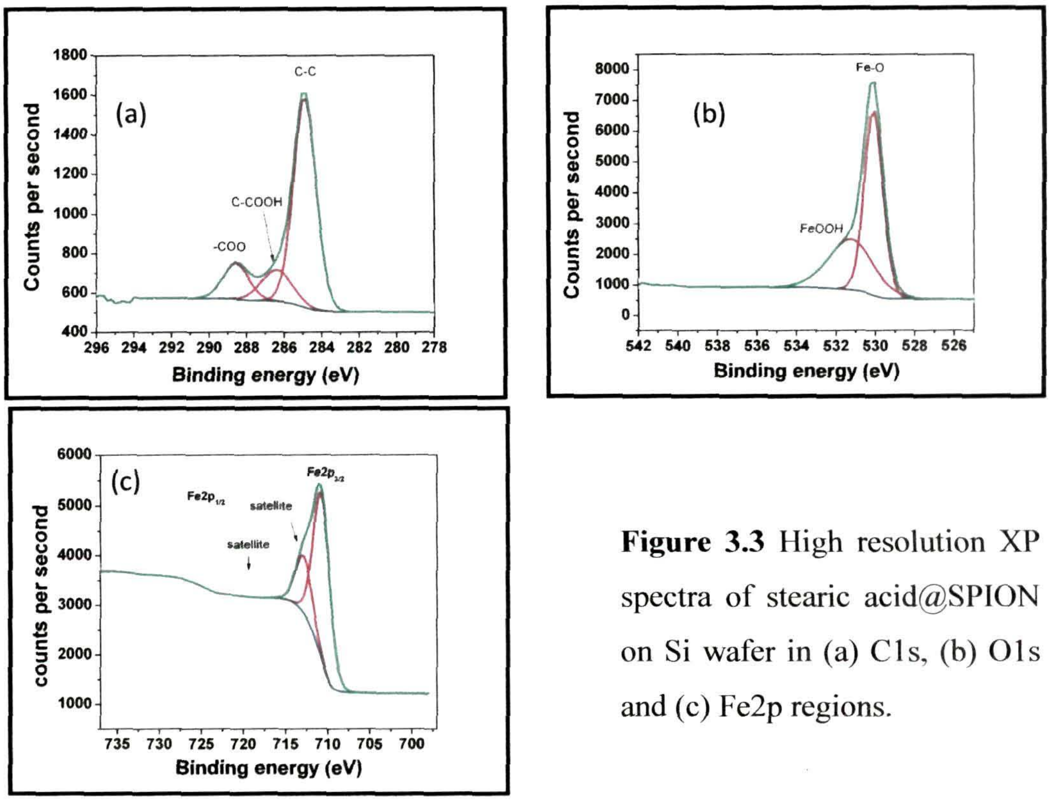

Figure 3.3 High resolution XP spectra of stearic acid@SPION on Si wafer in (a) C1s, (b) O1s and (c) Fe2p regions.

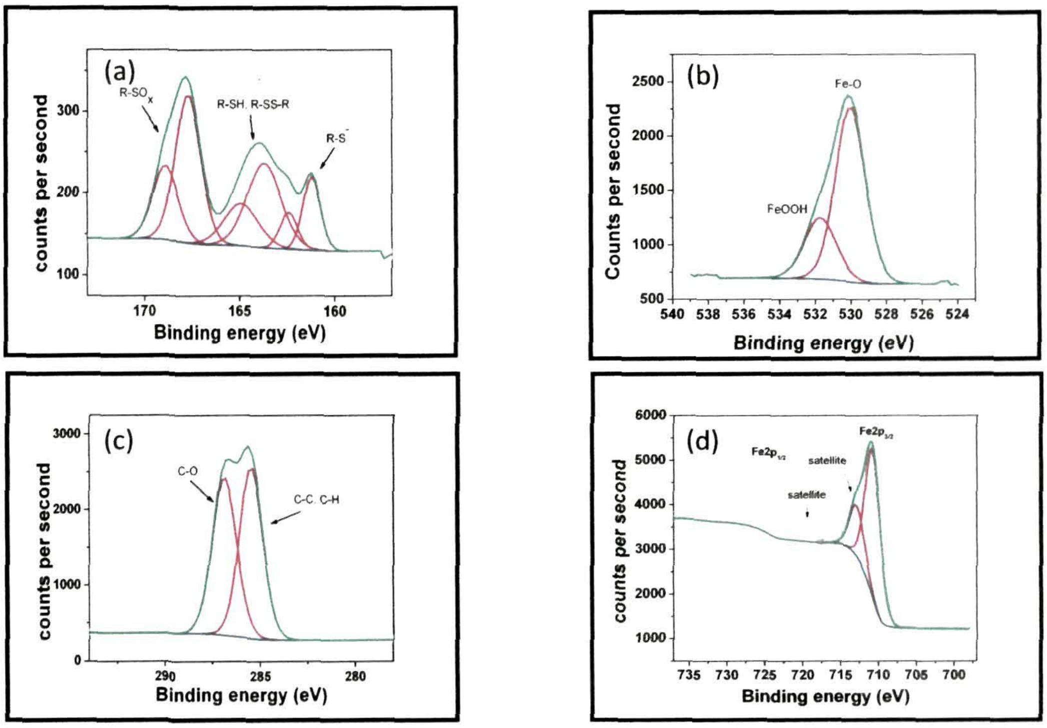

Figure 3.4 High resolution XP spectra of DMSA@SPION on Si wafer in the (a) S2p, (b) O1s, (c) C1s and (d) Fe2p regions.

Figure 3.4 shows the XPS spectra of (a) S2p, (b) O1s, (c) C1s and (d) Fe2p of DMSA modified SPION. For sulfur, three different species can be distinguished. From the peak positions, they are assigned to bound thiols (160.8/162 eV; $-S^-$), unbound thiols and disulfides (163.2/164.4 eV; -SH and -S-S-) and oxidized thiol groups (167.3/168.4 eV; -SO$_x$H) [21, 22, 23]. Part of the –SH groups become oxidized to form –SO$_x$H, may be because of the use of HNO_3 during pH adjustment or air exposure [24]. For carbon, the C1s region shows two components present in equal amounts, one of them (285 eV) typical for aliphatic carbon, the other one (286.5 eV) for carbon of –C-O- group [14-15]. Equal intensity of the two components and the absence of free COOH signature in the C1s spectra of this sample point towards the absence of stearic acid in the sample. Because in case of long carbon chain molecule of stearic acid, the C1s signature from C-C bond (285 eV) should have emerged out with higher intensity as observed in Figure 3.3 (a) for stearic acid capped SPION. However, the O1s spectra shows same peak positions as in Figure 3.3 (b) for stearic acid@SPION. In the raw XPS spectra of this sample, there is the evidence of N1s peak whose existence is quantified from the FTIR spectra presented hereafter.

To see any influence of pH adjustment on the characteristics of SPION, FTIR is done with stearic acid@SPION under two conditions. Sample A is the stearic acid@SPION powder, whose pH is found to be 3 when tried to make a suspension in water by prolonged sonication. Sample B is the solution of stearic acid@SPION in alkaline water of pH 11. In acidic pH, free carbonyl stretch is observed over the SPION surface characterized by the 1713 cm^{-1} peak appearing as a shoulder peak [from the inset of Figure 3.5(a), it is seen clearly]. On the other hand, the broad peak at 1635 cm^{-1} for curve (i) consists of more than one peak. Comparing with curve (ii) the constituent peaks of curve (i) can be identified as 1635 cm^{-1} peak for $O\text{-}H_{bending}$ vibration of surface adsorbed water molecules [25-26] and 1534 cm^{-1} peak for $COO_{antisymmentric}$ vibration [27]. All these signatures point towards the presence of strongly bonded stearate over SPION surface linked through COO group as well as weakly bonded stearic acid molecules interpenetrated between strongly bonded layer by tail to tail hydrophobic interaction. Other than that, the peaks identified in curve (i) are 546 cm^{-1} for Fe-O bond vibration [28], 1386 cm^{-1} for $C\text{-}H_{bending}$, 2856 cm^{-1} and 2922 cm^{-1} for antisymmetric and symmetric $C\text{-}H_{stretching}$ modes of CH_2 group of stearic acid. While the $O\text{-}H_{stretching}$ band has appeared at ~3400 cm^{-1}, the small peak at 2350 cm^{-1} is because of atmospheric CO_2. FTIR bands at 796 and 892 cm^{-1} in Figure 3.5(a) for stearic acid@SPION are assigned to Fe-OH.....H bending vibrations. In curve (ii) the extra peaks observed at1064 cm^{-1}, 1326 cm^{-1} and 1481 cm^{-1} are due to $C\text{-}O_{stretching}$, $C\text{-}N_{stretching}$ [29] and $COO_{symmentric}$ vibrations [27] respectively. It is worthwhile to mention here that pH adjustment to pH value 11 is carried out by the addition of tetramethyl ammonium hydroxide (TMAOH). With this, ionization of the carboxylic acid group of weakly bonded stearic acid is assumed to be occurring, resulting in the dispersibility of the SPION in aqueous medium along with the formation of ammoniumstearate. This fact is corroborated by the absence of free C=O peak at 1713 cm^{-1} and appearance of $C\text{-}N_{vibrational}$ mode in curve (ii).

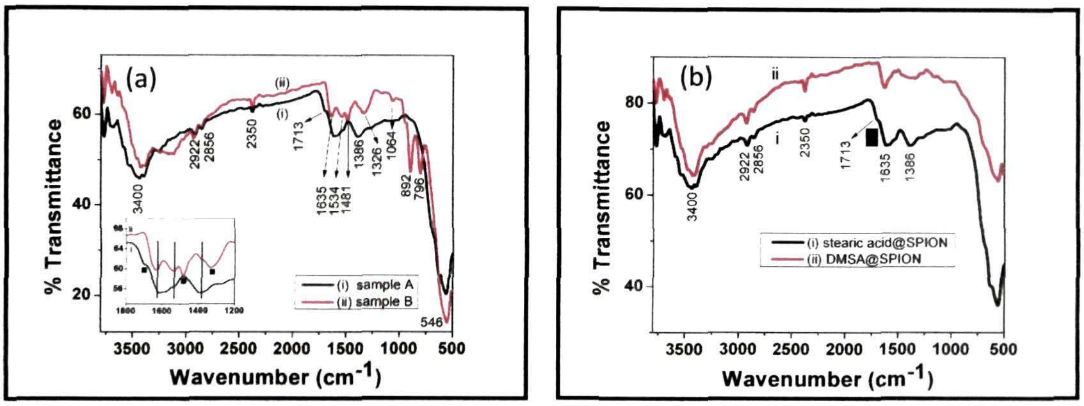

Figure 3.5 FTIR spectra of (a) stearic acid@SPION at pH 3 (curve i) and 11 (curve ii) and (b) stearic acid@SPION (curve i) and DMSA@SPION (curve ii). The inset of (a) shows the enlarged plot of the two samples in the wavenumber range 1800-1200 cm^{-1}.

Figure 3.5(b) shows the FTIR spectrum of DMSA@SPION and stearic acid@SPION samples. The major difference observed is that the free C=O peak at 1713 cm^{-1} is absent in the former. Moreover, the 1386 cm^{-1} peak for $C\text{-}H_{bending}$ has decreased in intensity and become broadened. This broad peak and the antisymmetric peak at 1635 cm^{-1} are assumed to be masking the antisymmetric and symmetric COO stretches of DMSA at 1457 cm^{-1} and 1523 cm^{-1} respectively.

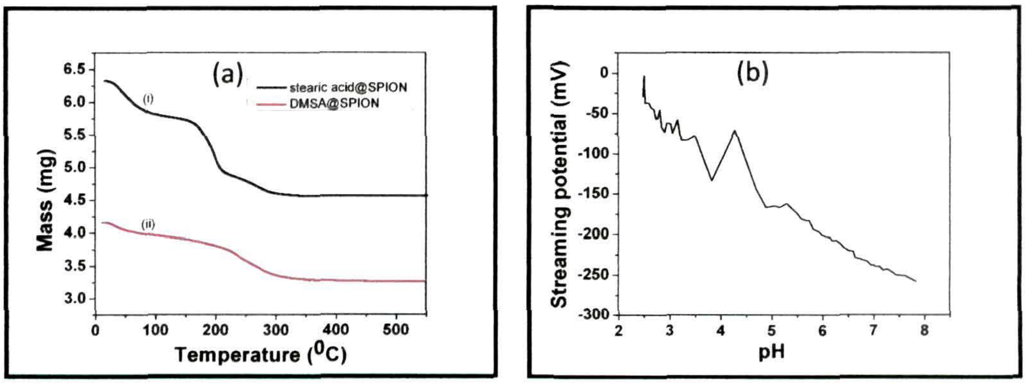

Figure 3.6 (a) TGA plot of stearic acid@SPION (curve i) and DMSA@SPION (curve ii) and (b) Streaming potential plot of DMSA@SPION.

To have a better idea of the nature of interaction of stearic acid surfactant with the nanoparticle surface, TGA analysis of the stearic acid capped and DMSA functionalized SPIONs have been done. In Figure 3.6(a), curve (i) presents the typical TGA curve of stearic acid@SPION revealing three distinct mass losses. The first dip in curve (i) near 100°C is due to loss of water molecules while the other two well defined dips are over temperature ranges from 160°C to 212°C and from 220°C to 300°C *respectively. For all surfactant capped particles with both strongly bonded and weakly* bonded surfactants, the heating curves are characterized by mass losses with two distinct steps, revealing a different pattern from that observed for monolayer surfactant coated particles [27, 30]. It is worthwhile to mention here that the nature of the interactions affects the deviation of the inflection temperature of the same surfactant [31]. Stronger chemical interactions can be responsible for the higher inflection temperature in case of the second mass loss and hence the fraction of mass loss (6.2%) centered at ~250°C is attributed to desorption and subsequent evaporation of the strongly bonded stearate to the nanoparticle surface through carboxylate head groups [30]. In the meanwhile, the higher % of mass loss (13.2%) centered at 170°C is due to the dissociation and evaporation of weakly bonded stearic acid molecules. On the other hand, TGA plot of DMSA@SPION [curve (ii) of Figure 3.6(a)] is characterized by two mass losses: one at ~100°C is due to loss of water and the second one (12.2%) at 250°C is due to the decomposition of DMSA ligands over the SPION surface.

Figure 3.6 (b) shows the streaming potential of the DMSA modified SPION. The streaming potential of it, measured in a Teflon capillary is found to be negative in the whole pH range from 2-11. At physiological pH, it is quite stable in solution form as found by its high streaming potential of -231 mV. The streaming potential measurement points out that the surface of stearic acid capped SPION is efficiently modified with the ligand DMSA.

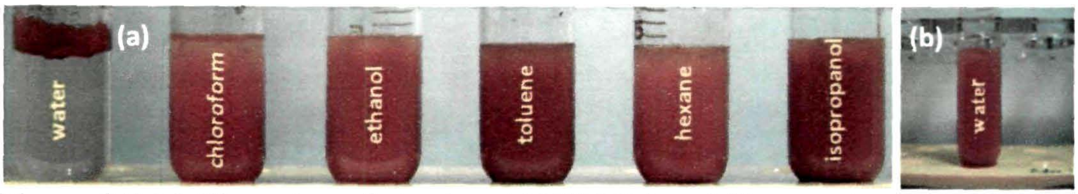

Figure 3.7 (a) Dispersion of stearic acid@SPION in different solvents and (b) in water at pH 11.

To check the dispersibility of stearic acid@SPION, it is tried to disperse in organic solvents and in acidic as well as alkaline aqueous medium and these are found to be dispersible in all organic solvents and in highly alkaline water [Figure 3.7(a) and (b)]. Based on the above findings and observations, surface model is developed comprising of the multilayer coating of stearic acid on SPION and for SPION surface modified with DMSA ligand. However, the number of surfactant layers cannot be predicted exactly. In case of the alkaline water soluble SPION, the stearic acid is strongly bonded on the nanoparticle surface through COO groups, leaving behind the tails towards outward. Since excess stearic acids are present in the reaction mixture so some of them remain as intercalated layer by physisorption through tail to tail hydrophobic interaction with the strongly bonded layer as depicted in Figure 3.8A. The remaining free stearic acid molecules are washed out during THF washing for several times. Now, in aqueous medium, the added TMAOH for making the pH highly alkaline (pH 11), ionizes the carboxylic group of weakly bonded layer to produce COO^- ions which may combine with $(CH_3)_4N^+$ ions to form ammonium carboxylate (Figure 3.8B). Because of this, in highly alkaline water, the stearic acid@SPIONs become dispersible as evident from Figure 3.7(b). Now, during surface modification with DMSA ligand, the highly alkaline pH weakens the hydrophobic force between the weakly bonded and strongly bonded layers due to strong hydration of carboxylate groups [32]. Simultaneous agitation in the form of sonication leads finally to the detachment of the weakly bonded layer and subsequently dithiol molecule of DMSA having higher affinity for iron replaces the strongly bonded stearic acids on SPION surface. Analyzing the EDX [Figure 3.2(h)], XPS [Figure 3.4(a)] and FTIR results [Figure 3.5(b)] of DMSA@SPION, it is understood that DMSA molecules are present as bound, unbound thiols, disulfides as well as adsorbed species on SPION surface through carboxyl heads. This whole arrangement of DMSA molecules over SPION surface results into their prolonged stability in water medium. In this regard, it is worthwhile to mention that disulfide bonds enhance stability [12]. The schematic diagram of DMSA@SPION is depicted in Figure 3.8C.

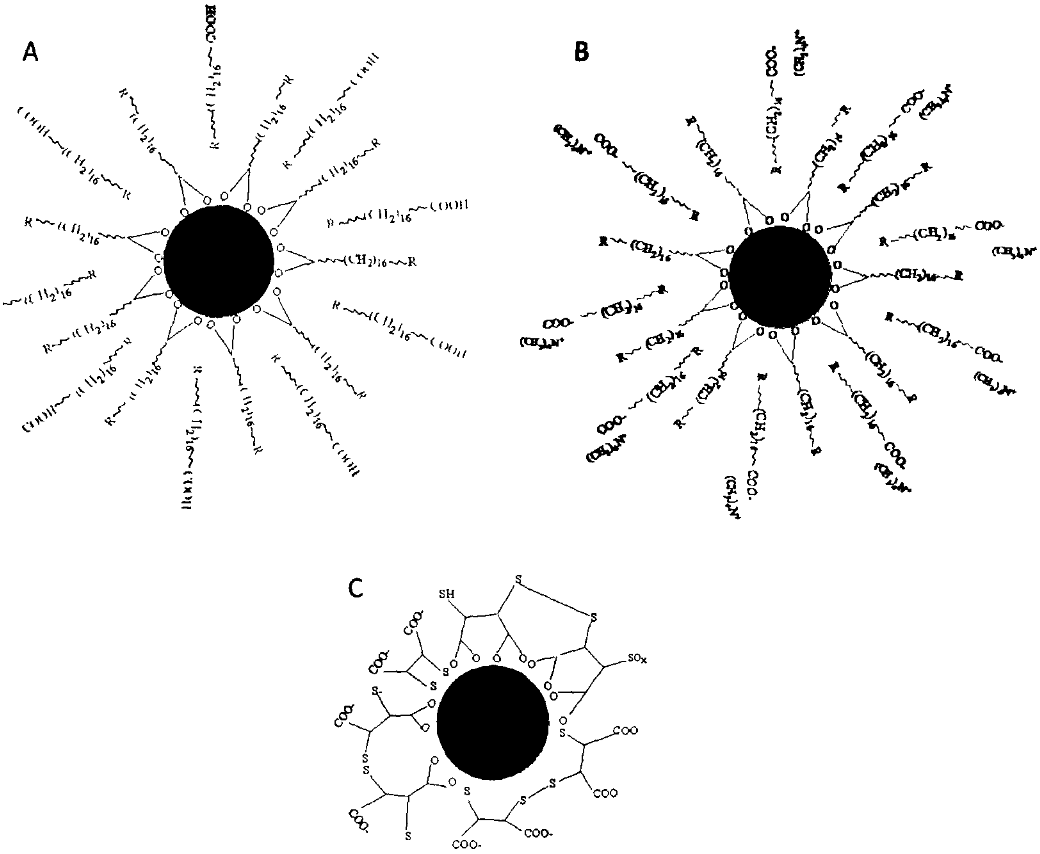

Figure 3.8 Schematic diagram of (A) multilayer coating of stearic acids on SPION surface, (B) deprotonation of weakly bound stearic acids in highly alkaline aqueous medium and (C) DMSA functionalization over SPION surface.

Part B

3.6 Synthesis of Iron-Platinum nanoparticles:

The synthesis technique used to develop iron platinum nanoparticles is a facile, aqueous, thermo-free, one-pot chemical route using vitamin C as both capping agent and reducing agent.Three samples were prepared varying the reduction method, pH of the reaction mixture and sequence of precursor addition. The samples were named as P1, P2 and P3.

P1:A typical direct aqueous synthesis procedure is performed as follows.Ascorbic acid ($C_6H_8O_6$) (10 mL, 0.1M) was dissolved in water and mixed with $Fe(NO_3)_3.9H_2O$ (2 mL, 0.033M in water) solution at room temperature by magnetic stirring. After 1.25 hr, $Na_2PtCl_6.6H_2O$ (2 mL, 0.005M in water) was added to the above mixture in a dropwise fashion and then the reaction mixture was aged for 24 h without stirring. Afterwards, the black precipitate was obtained by centrifugation at 14000 RPM for 15 min. Purification of the product was done by washing with water, ethanol and acetone for several times.

P2: To see the effect of coreduction method in the synthesis of nanoparticles, a secondary reducing agent, $NaBH_4$ was introduced along with ascorbic acid. Hence, keeping the molar ratios of precursors same as before (P1 synthesis), only $NaBH_4$ (0.033 M, 0.2548 gm) was newly introduced to the reaction mixture after all other precursors are added.

P3: In this method, $C_6H_8O_6$ (10 ml, 0.1M) and $Fe(NO_3)_3.9H_2O$ (2 ml, 0.033M) solutions were mixed at room temperature. This mixture was kept on stirring for 20 min and then 0.2548 gm or 0.033M of $NaBH_4$ was added to it. Instantly, black colored ppt was formed which was characterized to be iron particles from EDS spectra [Figure 3.9 (d)]. But, this reaction continued for very short period of time and the solution became completely clear within 30 min i.e. the formed iron particles dissolute. After that the platinum precursor, $Na_2PtCl_6.6H_2O$ (2 ml, 0.005M) was added to the above mixture dropwise. The reaction mixture was left as such for 24 hrs and then the black precipitate was obtained by centrifugation at 14000 RPM for 15 min. The purification of the ppt was done by water, ethanol and acetone washing for several times.

To evaluate the effect of pH during synthesis, on the composition of the resulting FePt nanoparticles, P3 synthesis is carried out at alkaline pH. In the method, ascorbic acid (10 mL, 0.1M) and $Fe(NO_3)_3.9H_2O$ (2 mL, 0.033M) are mixed at room temperature. The pH of the mixture is found to be ~2.3 which is adjusted to 10 by dropwise addition of tetramethyl ammonium hydroxide (TMAOH). This mixture is kept on stirring for 20 min. Subsequently, 14 mL 0.033M of $NaBH_4$ is added. Instantly, black precipitates are formed in a vigorous reaction which are confirmed to be Fe particles later from EDX characterization. The pH of this solution remained at 10. Unlike in the synthesis of P3, the solution does not become clear within 30 min. Then platinum precursor, $Na_2PtCl_6.6H_2O$ (2 mL, 0.005M) is added to the above mixture dropwise. The reaction mixture is left as such for 24 h. Finally black precipitate was obtained by centrifugation at 14000 RPM for 15 min. The purification of the product is done by water, ethanol and acetone washing for several times.

A naturally occurring vitamin, ascorbic acid is used as reducing agent to synthesize metal nanoparticles due to its high water solubility, biodegradability and low toxicity. Because of significant difference in their standard reduction potential, ascorbic acid is a good reducing agent for noble metal precursors [E° (Pt^{2+}/Pt) = +1.2 V, E° (ascorbic acid) = +0.06 V]. While acting as a reducing agent, its oxidized form is coordinated to the nanoparticle surface which serves to act as a capping agent. However, ascorbic acid also plays the role of antioxidant by scavenging the free radicals during nuclei formation [33]. In samples P2 and P3, ascorbic acid and $NaBH_4$ perform coreduction in which nucleation is initiated by the action of $NaBH_4$, while growth is followed by the synergistic reduction by ascorbic acid at room temperature. P2 synthesis consists of simultaneous reduction of Fe and Pt precursors while in P3, Fe particles are formed initially and re-dissolve before addition of the Pt precursor due to the acidic pH of the reaction medium, which is substantiated by the disappearance of black precipitate followed by formation of a clear solution within 15 min. The initial pH of the ascorbic acid and $Fe(NO_3)_3$ solution mixture is found to be 3, while after $NaBH_4$ addition, pH is increased to 4. Studies on pH dependent dissolution of iron particles reveal the possibility of dissolution at such pH [34]. Therefore, when the Pt precursor is added to the reaction mixture containing the reducing agent, rapid formation of Pt particles occurs, while Fe particles slowly reform after initial dissolution.

3.7 Results and discussion:

Compositional analysis of the nanoparticles is done with the aid of energy dispersive X-ray spectroscopy (EDS) and results are shown in Figure 3.9. The average Fe and Pt atomic compositions for the three samples as determined from 5-6 different locations are found to be $Fe_{0.04}Pt_{0.95}$ (P1), $Fe_{0.14}Pt_{0.86}$ (P2) and $Fe_{0.12}Pt_{0.88}$ (P3) respectively. The composition of the P3 sample synthesized at alkaline pH is found to be $Fe_{0.88}Pt_{0.12}$ [EDX spectrum is shown in Appendix A]. Figure 3.9 (d) shows the EDS spectra of Fe particles formed during P3 synthesis.

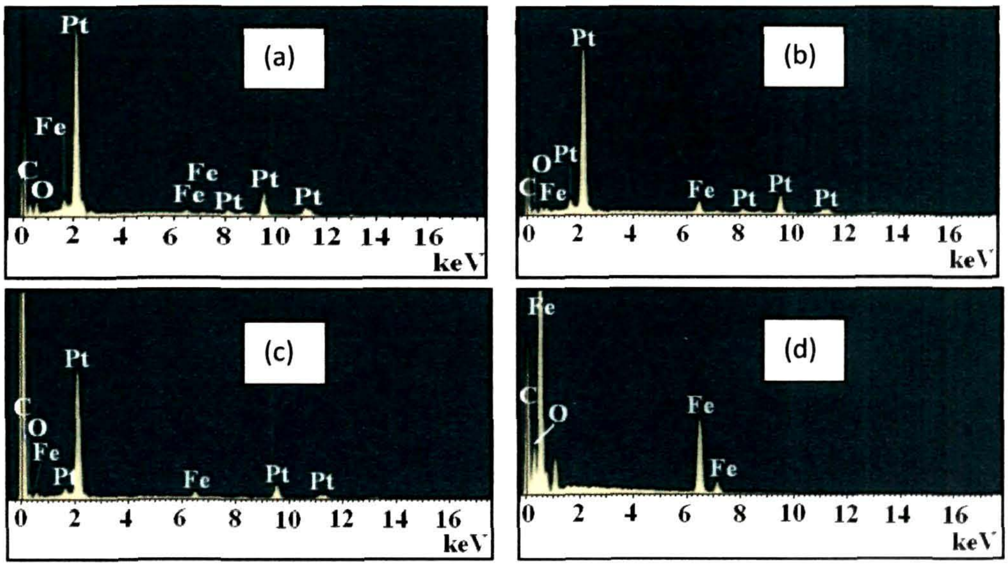

Figure 3.9 EDS spectra of (a) P1, (b) P2, (c) P3 samples and (d) Fe particles formed during P3 synthesis.

The XRD pattern of all three samples show the highest intensity peak ~39° for 2θ assigned to (111) planes of cubic Pt phase [PDF: 88-2343]. The XRD pattern of P1, shown in Figure 3.10, indicates the presence of both tetragonal $L1_0$ and cubic A1 phases of FePt along with cubic Pt phase. But in samples P2 and P3, the $L1_0$ phase of FePt is not observed. Ascorbic acid is a good reducing agent for the synthesis of noble metals [35] and hence the reduction of the noble metal precursor becomes faster in case of P1. Under the condition of rapid reduction, there will be sufficient Pt atoms leading to fast surface growth (as evident from microstructural analysis) and also resulting in evolution of ordered $L1_0$ phase in P1 sample. P2 synthesis incorporates the simultaneous reduction of Fe and Pt precursors resulting in less intense and broad XRD peaks for cubic Pt phase as seen in Figure 3.10. The reaction conditions of sample P3 is similar to sample P1 but the coreduction by ascorbic acid and $NaBH_4$ may be responsible for the absence of $L1_0$ FePt phase, in contrast to sample P1. Only peaks for A1 FePt phase along with cubic Pt phase are observed in the XRD spectra of P3. The XRD analysis of three samples is presented in Table 3.1.

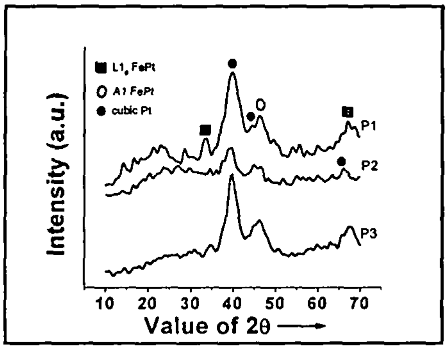

Figure 3.10 XRD patterns of three samples.

Table 3.1 Analysis of XRD patterns of three samples

Value of 2θ	Plane	System	Reference PDF
33°	110	$L1_0$ FePt	65-4674
39°	111	Cubic Pt	88-2343
44°	200	Cubic Pt	87-0644
46°	200	A1 FePt	65-2868
65.9°	220	Cubic Pt	88-2343
67°	220	$L1_0$ FePt	89-2051

To assess the magnetic property of the samples, M-H characterization of the three samples was done and the results are presented in Figure 3.11. The coercivity of magnetic nanoparticles is mainly dependent on two factors: (i) particle size and (ii) ordering [36]. The P1 sample is soft ferromagnetic in nature, as observed from its M-H curve with coercivity of ~240.5 G [Figure 3.11(a)]. The ferromagnetic behavior is quite obvious since the ordered $L1_0$fct phase of FePt is present in this sample, along with the A1 fcc FePt with disorder in lattice site occupation, and cubic Pt phases. It is worthwhile to mention here that pure Pt particles were synthesized following the same procedure and their magnetic properties were checked. From Figure 3.11(a), the diamagnetic behavior of pristine Pt particles is clearly visible. Therefore, the cubic Pt phase in the nanoparticle should not contribute to the soft ferromagnetic property of the nanoparticles. The M-H curve of P1 sample is replotted within magnified X and Y range around the origin [Figure 2.11(b)]. From this plot, shifting of the hysteresis loop away from the origin is observed which is the signature of the exchange bias phenomenon [10]. As estimated from the M–H plot, the exchange bias field is 47.5 G for P1. From this, formation of antiferromagnetic $L1_2$ $FePt_3$ phase can also be assumed due to the utilization of ascorbic acid as reducing agent leading to the Pt rich phase. Sample P2 is superparamagnetic by nature with negligible coercivity as evident from its magnetization curve [Figure 3.11(c)]. The superparamagnetic behavior in this iron-platinum nanoparticle can be attributed to their ultrafine dimension. Most interestingly, sample P3 is paramagnetic [Figure 3.11(a)]. In alloys like FePt, the magnetization decreases as the atomic percentage of Pt increases in the overall composition. Therefore, it can be inferred that Pt acts as a diluent of magnetization. In such dilute conditions, Fe atoms (magnetic) are much far apart and hence the exchange interaction is unable to align the spins of nearest neighbor Fe atoms in parallel arrangement, resulting in paramagnetic behavior as a whole.

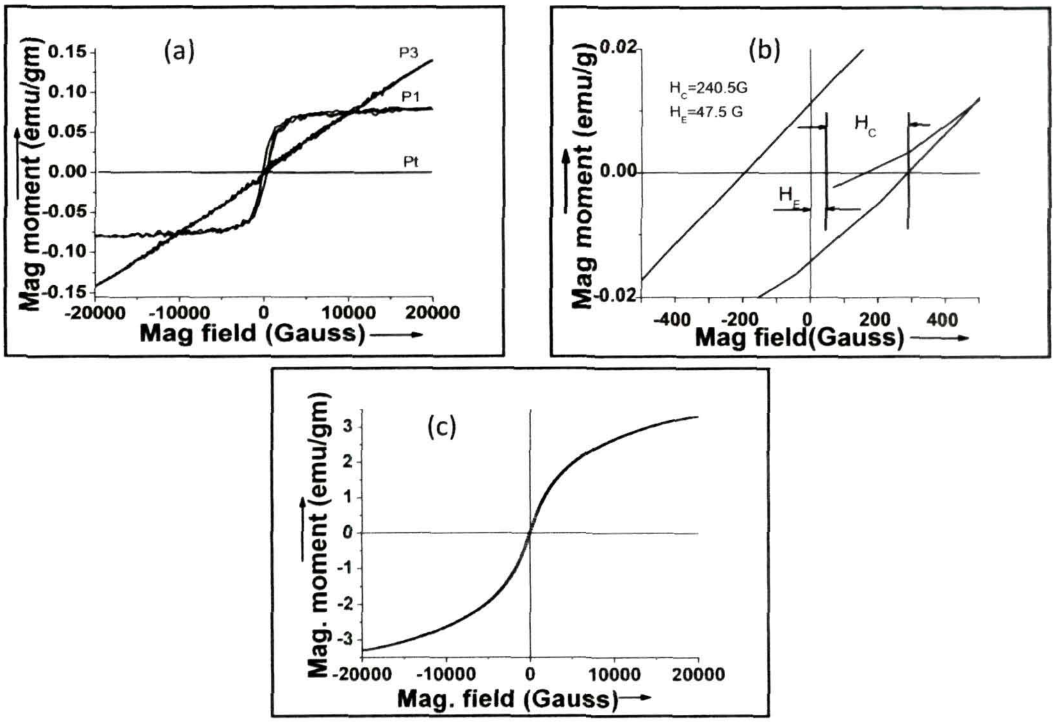

Figure 3.11 (a) M-H curves of P1, P3 and Pt particles, (b) The enlarged magnetization curve of P1 sample near origin and (c) M-H curve of P2 sample.

HRTEM images along with size distribution histograms of three samples are shown in Figure 3.12(a, c, e). From the HRTEM micrographs the size distribution curves were prepared. Average particle sizes are found as ~ 2.3 nm, 1.9 nm and 1.7 nm for P1, P2 and P3, respectively. The selected area electron diffraction (SAED) pattern of P1 [Figure 3.12(b)] clearly shows the bright spots of (110) plane, which is a fingerprint of the L1$_0$ FePt phase. Moreover, (200) and (210) planes of A1 phase of FePt and (111) plane for pure Pt are identified from the SAED patterns of P1, P2 and P3 [Figure 3.12 (b), (d), (f)].

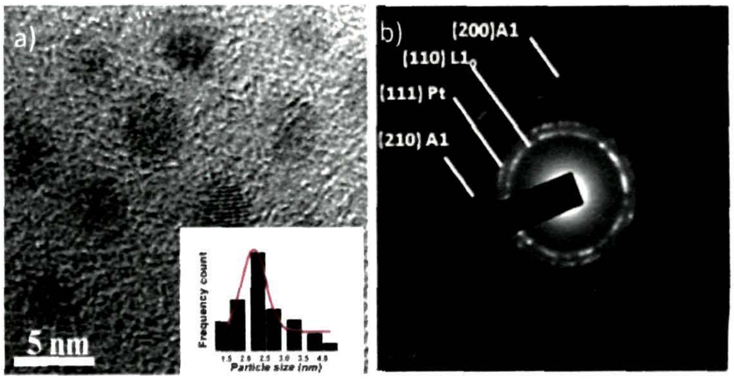

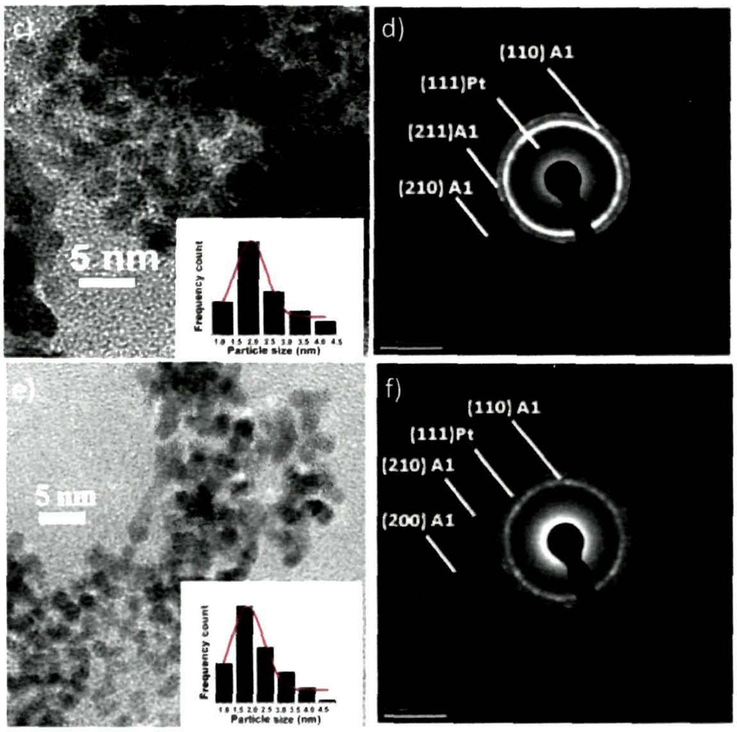

Figure 3.12 (a), (c) and (e) HRTEM images with size distribution histograms in inset and (b), (d) and (f) show the SAED patterns of P1, P2 and P3 samples, respectively.

The surface characteristics of the synthesized samples are examined through Fourier transform infrared spectroscopy (FTIR) and streaming potential measurements. The FTIR spectra and streaming potential plots of three samples are shown in Figure 3.13.

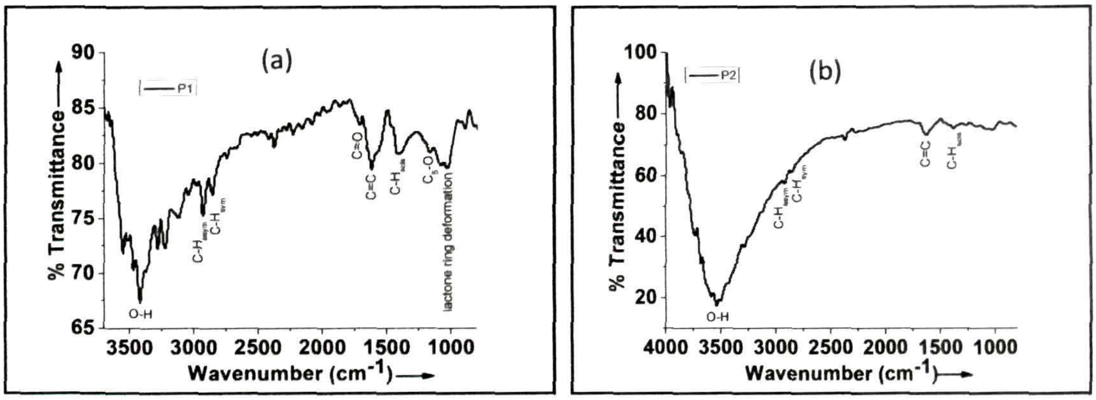

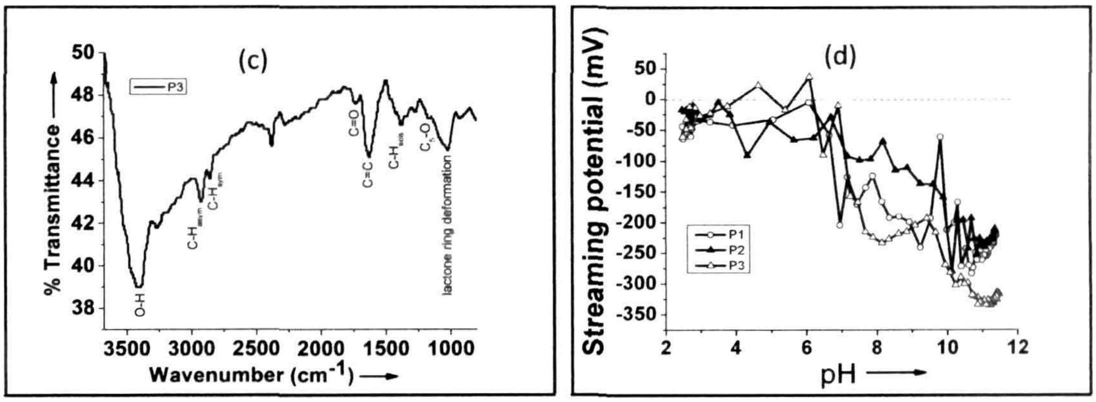

Figure 3.13 (a), (b), (c) FTIR spectra and (d) Streaming potential plot of P1, P2 and P3.

As observed from Figure 3.13 (a), (b) and (c), the typical bands for ascorbic acid in the fingerprint region are present in all the samples. In case of P1 and P3 samples, almost similar bands are observed in the FTIR spectra [Figure 3.13(a) and (c)]. As described earlier, ascorbic acid acts as a reducing agent by oxidizing its C=C double bond as well as its oxidized form, dehydroascorbic acid, acts as a capping agent through the interaction of its carbonyl group with the FePt nanoparticles [37]. This fact is corroborated by the absence of $C{=}C_{stretching}$ band at ~1650 cm^{-1} and the presence of a band at 1626 cm^{-1} due to the adsorption of dehydroascorbic acid carbonyl to the nanoparticle surface [37]. Another band observed at 1725 cm^{-1} is due to the oxidated ester carbonyl of dehydroascorbic acid [38]. However, the scissoring, symmetric and antisymmetric stretching of $C{-}H_{vibrational}$ bands are observed at 1474, 2853 and 2924 cm^{-1} respectively [39]. Also the bands corresponding to lactone ring deformation as well as C_5-O stretching vibration are observed at 1030 and 1165 cm^{-1} respectively [40]. In the spectra of P3 sample, a band at 1379 cm^{-1} is observed corresponding to C–O–H bending vibration [Figure 3.13(c) [39]. In case of P2 sample, only the 1630 cm^{-1} band is observed prominently corresponding to the coordination of dehydroascorbic acid to nanoparticles [Figure 3.13(b)]. Furthermore, presence of strong $O{-}H_{stretching}$ mode at around ~ 3300 cm^{-1} confirms the presence of hydroxyl groups in all three samples, which provide hydrophilicity to the nanoparticles increasing their water solubility. As observed from Figure 3.13 (d), all the three samples show negative streaming potential almost over the whole pH range starting from 2 to 12. The above findings corroborate to the organic functionalization of the nanoparticles. The schematic diagram of bonding of dehydroascorbic acid to nanoparticle is depicted in Figure 3.14.

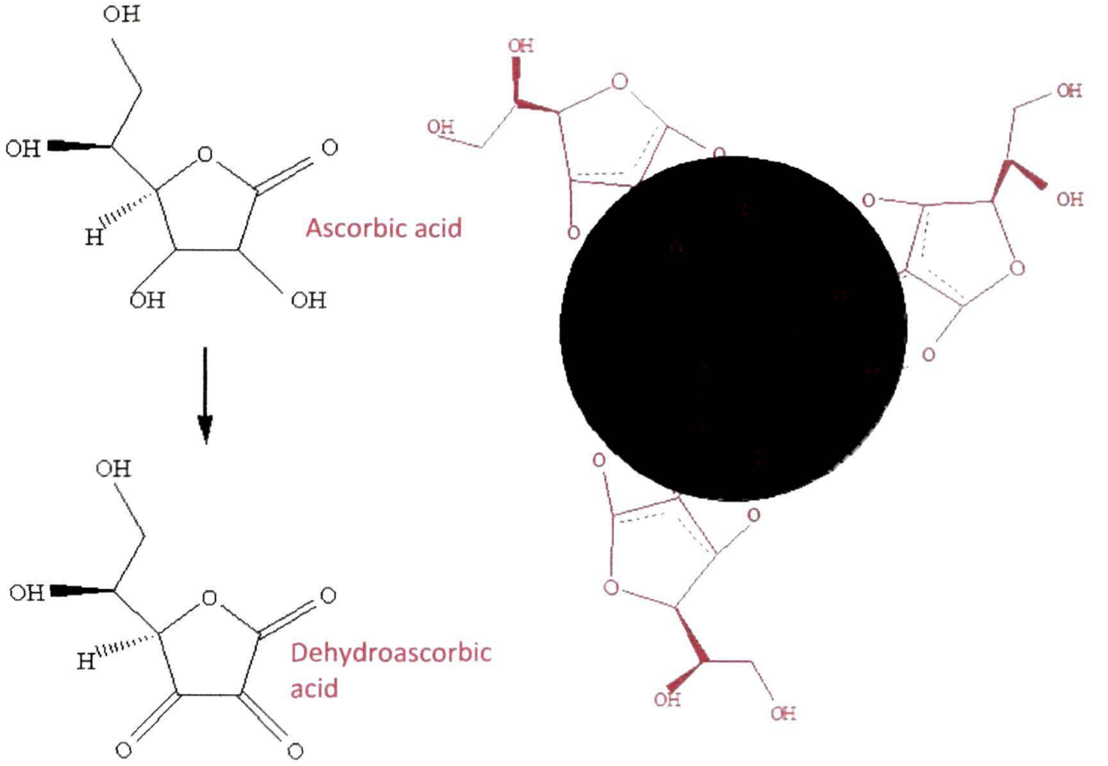

Figure 3.14 Schematic diagram of interaction of oxidized form of ascorbic acid with nanoparticle surface.

Being superparamagnetic in nature, sample P2 is carried forward for examining multifunctionality in a single system; suitable in biomedical application. Surface analysis of P2 sample has been carried out by X-ray photoelectron spectroscopy (XPS). Figure 3.15 (a) shows the XPS spectra of Pt 4f peak of sample P2. The binding energy (BE) position for Pt $4f_{7/2}$ peak in bulk Pt^0 state is at 71.2 eV which is observed at 70.9 eV in this case [41]. This negative shift in BE for nanoparticles of size <7 nm is obvious [42]. One of the reasons behind it is the increase of core electron BE values with reduced cluster size and the other is the interaction between organic capping agent (in this case ascorbic acid) and Pt atoms. Also, it is to be noted that if Pt atoms act as electron acceptor in the interaction, then its BE decreases [42]. The other peak at BE 74.3 eV is for Pt $4f_{5/2}$ of metallic Pt [43]. It is observed from Figure 3.15(b), the C1s peak consists of three components, among which the 285 eV peak is due to aliphatic carbon and the 286.5 eV peak is assigned to carbon of —C–O group [7], while the peak at 288.8 eV is because of —C=O group [44]. Figure 3.15(c) shows that the O1s spectra consists of two peaks at 530.3 eV and 531.8 eV which correspond to the O atoms of FeOOH and C=O or O-H respectively [45-46]. Figure 3.15(d) shows the XPS spectra for Fe $2p_{3/2}$ peak. The peak for Fe^0 state has been shifted from 706.6 eV to 704.4 eV [47] while the peak at 711.5 eV is for Fe^{III} [48].

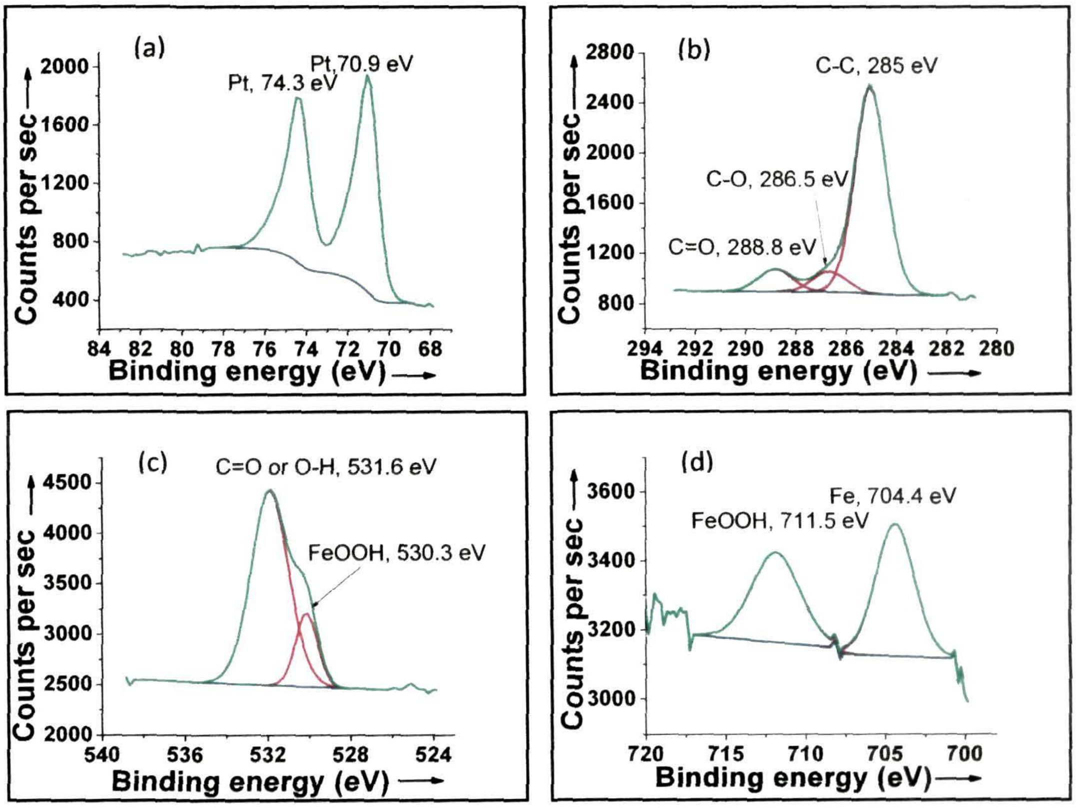

Figure 3.15 XPS spectra of (a) Pt $4f_{7/2}$ and Pt $4f_{5/2}$, (b) C1s, (c) O1s and (d) Fe 2p peaks for P2 sample.

3.8 Conclusion:

Both the iron oxide and iron platinum nanoparticles are superparamagnetic in nature which make them suitable for biomedical application. The ultrastable surface hydrophilic SPIONs are obtained through controlled displacement of stearic acid by DMSA without any alteration in particle microstructure. SPIONs with average diameter of ~3 nm were synthesized using stearic acid as surfactant. Presence of strongly and weakly bound stearic acid layers over SPION surface is evidenced from characterization results. With these particles, stable dispersions in organic solvents as well as in aqueous medium at high pH can be obtained. Controlled replacement by DMSA enabled the generation of stable aqueous dispersions over a wide range of pH values. On the other hand, the iron platinum nanoparticles are obtained by a simple, aqueous, one-pot chemical route whereas the ascorbic acid coating renders hydrophilicity and biocompatibility characteristic to the nanoparticles. Optimized reaction condition has been determined to produce iron platinum nanoparticles with superparamagnetic characteristic.

References:

[1] du Trmolet de Lacheisserie, E., Gignoux, D. and Schlenker, M. (Eds.) *Magnetism: Materials and Applications*, Springer, Boston, 2003.

[2] Sun, S., et al. Monodisperse FePt Nanoparticles and Ferromagnetic FePt Nanocrystal Superlattices, *Science* **287** (5460), 1989-1992, 2000.

[3] Gupta, A. K. and Gupta, M. Synthesis and surface engineering of iron oxide nanoparticles for biomedical applications, *Biomaterials* **26** (18), 3995-4021, 2005.

[4] Bang, J. H. and Suslick, K. S. Sonochemical Synthesis of Nanosized Hollow Hematite, *J. Am. Chem. Soc.* **129** (8), 2242-2243, 2007.

[5] Giri, S., et al. Magnetic properties of α -Fe_2O_3 nanoparticle synthesized by a new hydrothermal method, *J. Magn. Magn. Mater.* **285** (1-2), 296-302, 2005.

[6] Kang, Y. S., et al. Synthesis and characterization of nanometer- size Fe_3O_4 particles and γ-Fe_2O_3 particles, *Chem. Mater.* **8** (9), 2209-2211, 1996.

[7] Gogoi, M., et al. Direct monophasic replacement of fatty acid by DMSA on SPION surface, *Appl. Surf. Sci.* **258** (24), 9685-9691, 2012.

[8] Gogoi, M., et al. Single moiety, multifunctional Iron-Platinum nanoparticles synthesized by facile aqueous route (communicated).

[9] Cullity, B. D. and Graham, C. D., *Introduction to magnetic materials*, Wiley, New Jersey, 2009.

[10] Guimarães, A. P., *Principles of Nanomagnetism*, Springer, New York, 2009.

[11] Deb, P., et al. Anomalous agglomeration characteristics observed in iron oxide nanoclusters, *Philos. Mag. Lett.* **86** (8), 491-499, 2006.

[12] Soler, M. A. G., et al. Spectroscopic study of maghemite nanoparticles surface-grafted with DMSA, *J. Phys. Chem. A* **115** (6), 1003-1008, 2010.

[13] Beamson, G. and Briggs, D. *High Resolution XPS of Organic Polymers: The Scienta ESCA 300 Database*, Wiley, New York, 1992.

[14] Xie, F. Y., et al. Surface structure characterization of nanodiamond thin film for electronic field emission applications, *J. Vac. Sci. Technol. B* **26** (1), 102-105, 2008.

---

[15] Bou, M., Martin, J. M. and Mogne, T. L. Chemistry of the interface between aluminium and polyethyleneterephthalate by XPS, *Appl. Surf. Sci.* **47** (1), 149-161, 1991.

[16] Barr, T. L. An ESCA study of the termination of the passivation of elemental metals, *J. Phys. Chem.* **82** (16), 1801-1810, 1978.

[17] Kishi, K. and Ehara, Y. Interaction of acetic acid with ethylenediamine on a Ni(111) surface studied by XPS, *Surf. Sci.* **176** (3), 567-577, 1986.

[18] Bogatyrev, V. M., et al. Synthesis and characterization of Fe_2O_3/SiO_2 nanocomposites, *J. colloid Interface Sci.* **338** (2), 376-388, 2009.

[19] Castro, V.D. and Ciampi, S. XPS study of the growth and reactivity of FeMnO thin films, *Surf. Sci.* **331-333** (Part A), 294-299, 1995.

[20] Gao, Q., et al. The study of novel Fe_3O_4@γ-Fe_2O_3 core/shell nanomaterials with improved properties, *J. Magn. Magn. Mater.* **321** (8), 1052-1057, 2009.

[21] Sun, F., Castner, D.G. and Grainger, D.W. Ultrathin self-assembled polymeric films on solid surfaces. 2. Formation of 11-(n-Pentyldithio)undecanoate-bearing polyacrylate monolayers on gold, *Langmuir* **9** (11), 3200-3207, 1993.

[22] Castner, D.G., Hinds, K. and Grainger, D.W. X-ray photoelectron spectroscopy Sulfur 2p study of organic thiol and disulfide binding interactions with Gold surfaces, *Langmuir* **12** (21), 5083-5086, 1996.

[23] Nuzzo, R.G., Zegarski, B.R. and Dubois, L.H. Fundamental studies of the chemisorption of organosulfur Compounds on Au(111). Implications for molecular self-assembly on Gold surfaces, *J. Am. Chem. Soc.***109** (3), 733-740, 1987.

[24] Cremlyn, R.J.W. *An Introduction to Organosulfur Chemistry*, John Wiley & Sons Ltd, UK, 1996.

[25] Bertie, J.E. and Lan, Z. Infrared intensities of liquids XX: the intensity of the OH stretching band of liquid water revisited, and the best current values of the optical constants of $H_2O(l)$ at 25°C between 15,000 and 1 cm^{-1}, *Appl. Spectrosc.* **50** (8), 1047-1057, 1996.

[26] Eshaghi, A., Pakshir, M. and Mozaffarinia, R. Photoinduced properties of nanocrystalline TiO_2 sol-gel derived thin films, *Bull. Mater. Sci.* **33** (4), 365-369, 2010.

[27] Yang, K., Peng, H., Wen, Y. and Li, N. Re-examination of characteristic FTIR spectrum of secondary layer in bilayer oleic acid-coated Fe_3O_4 nanoparticles, *Appl. Surf. Sci.* **256** (10), 3093-3097, 2010.

[28] Krehula, S. and Musić, S. The influence of platinum (IV) ions on the formation of iron oxides in a highly alkaline medium, *J. Mol. Struct.* **993** (1-3), 382-389, 2011.

[29] Kalsi, P.S. *Spectroscopy of Organic Compounds*, New Age International Publishers, Delhi, 2007.

[30] Viali, R. W., et al. Investigation of the Molecular Surface Coating on the Stability of Insulating Magnetic Oils, *J. Phys. Chem. C* **114** (1), 179-188, 2010.

[31] Shen, L., Laibinis, P. E. and Hatton, T. A. Bilayer Surfactant Stabilized Magnetic Fluids: Synthesis and Interactions at Interfaces, *Langmuir* **15** (2), 447-453, 1999.

[32] Lan, Q., et al. Synthesis of bilayer oleic acid-coated Fe_3O_4 nanoparticles and their application in pH-responsive Pickering emulsions, *J. colloid Interface Sci.* **310** (1), 260-269, 2007.

[33] Dang, T. M. D., et al. Synthesis and optical properties of copper nanoparticles prepared by a chemical reduction method, *Adv. Nat. Sci.: Nanosci. Nanotechnol.* **2** (1), 015009(1)- 015009(6), 2011.

[34] Shi, Z., et al. Iron dissolution kinetics of mineral dust at low pH during simulated atmospheric processing, *Atmos. Chem. Phys.* **11** (3), 995-1007, 2011.

[35] Pradeep, T. and Anshup, Noble metal nanoparticles for water purification: A critical review, *Thin Solid Films*, **517** (24), 6441-6478, 2009.

[36] Joseyphus, R. J., et al. Composition controlled synthesis of fcc-FePt nanoparticles using a modified polyol process, *J. Mater. Sci.* **43** (7), 2402-2406, 2008.

[37] Xiao, L., et al. Water-soluble superparamagnetic magnetite nanoparticles with biocompatible coating for enhanced magnetic resonance imaging, *ACS Nano* **5** (8), 6315-6324, 2011.

[38] Xiong, J., Wang, Y., Xue, Q. and Wu, X. Synthesis of highly stable dispersions of nanosized copper particles using L-ascorbic acid, *Green Chem.* **13** (4), 900-904, 2011.

[39] Panicker, C. Y., Varghese, H. T. and Philip, D. FT-IR, FT-Raman and SERS spectra of Vitamin C, *Spectrochimica Acta Part A: Molecular and Biomolecular Spectroscopy* **65** (3-4), 802-804, 2006.

---

[40] Davies, M. B., Austin, J. and Partridge, D. A. *Vitamin C: Its Chemistry and Biochemistry,* The Royal Society of Chemistry, Cambridge, 1991.

[41]Wagner, C. D. X-ray photoelectron spectroscopy with x-ray photons of higher energy, *J. Vac. Sci. Technol.* 15 (2), 518-523.

[42] Qiu, L., et al. Evidence of a unique electron donor-acceptor property for Platinum nanoparticles as studied by XPS, *Langmuir* **22** (10), 4480-4482, 2006.

[43] Tu, W., et al. Interface effect on the electronic structure of alkanethiol-coated Platinum nanoparticles, *J. Phys. Chem. B* **107** (37), 10134-10140, 2003.

[44] Clark , D. T. and Thomas, H. R. Applications of ESCA to polymer chemistry. X. Core and valence energy levels of a series of polyacrylates, *J. Poly. Sc. : Poly. Chem. Ed.* **14** (7), 1671-1700, 1976.

[45] McIntyre, N. S. and Zetaruk, D. G. X-ray Photoelectron spectroscopic studies of iron oxides , *Anal. Chem.* **49** (11), 1521-1529, 1977.

[46] Méndez-Vilas, A. and Déaz, J. (Eds.), *Microscopy: Science, Technology, Applications and Education,* FORMATEX, Spain, 2010.

[47] Mills, P. and Sullivan, J. L. A study of the core level electrons in iron and its three oxides by means of X-ray photoelectron spectroscopy, *J. Phys. D: Appl. Phys.* **16** (5), 723-732, 1983.

[48] Konno, H. and Nagayama, M. X-ray photoelectron spectra of hexavalent iron, *J. Elect. Spec. Rel. Pheno.* **18** (3), 341-343, 1980.

Chapter 4

Fluorescent probe

4.1 Introduction:

Optical detection or imaging in life science is obtained by the interaction of biomolecules with fluorescent probes and hence is dependent on physicochemical properties of the same. Fluorescent probes can be broadly divided into three groups: — (i) molecular systems with defined structures (e.g. organic dyes, metal-ligand complexes), (ii) nanocrystal chromophores with size-dependent optical and physicochemical properties [e.g. II-VI and III-V semiconductor quantum dots (QD)] and (iii) nanometer to micrometer sized particles with size-independent properties (e.g. carbon nanoparticles, polymer beads etc.). Optical properties of QDs are controlled by constituent material, particle size and surface chemistry, particularly number of dangling bonds favoring nonradiative deactivation [1]. Often surface passivation is done in QDs to prevent heavy metal ion leakage either by growing a shell or by using capping agent [2]. The fluorescence property of organic dyes originate either from optical transition delocalized over the whole molecule or from intramolecular charge transfer transition [3].

QDs have advancements over organic dyes in having absorption and emission properties tunable by particle size, known as quantum-size effect [4]. This leads to multiplexing detection i.e. simultaneous analysis of different analytes which are obtained by single wavelength excitation of a size series of QDs. However, monoexponential decay kinetics of organic dyes makes them suitable in lifetime measurement [5]. Also, solubility of the probes in relevant media is important, for which QD dispersibility is taken care by chemical nature of surface coating while in case of organic dyes substitution is done without affecting optical properties. But regarding the bioconjugation aspect to the fluorescent probe, the quantum yield decreases both in case of QDs and organic dyes. However, stability of the fluorescent probe under relevant condition is another important aspect to be concerned. In this regard, it is worthwhile to mention that adequately surface-passivated QDs possess thermal and photochemical stability, where organic dyes experience limitations. Considering the cytotoxicity of fluorescent probes for in vivo imaging, organic dyes do not exhibit major problem but in case of QDs, cytotoxicity was observed due to leaking of heavy metals, presence of cytotoxic surface ligands and/or nanoparticle aggregation [6-7]. Efforts are put forwarded to prevent these aspects by growing shell or functionalizing biocompatible ligand over the QD surface or by synthesizing III-V QDs doped with Mn^{2+} [8].

Part A

4.2 Synthesis of undoped and doped CdTe quantum dots (QDs):

The pristine CdTe QDs are prepared by following a reported procedure [9]. To describe it briefly, a buffer is prepared initially by mixing 25 ml of 15 mM $Na_2B_4O_7$ and 25 ml of 15 mM citric acid of pH 7.2. The precursor solution is prepared by mixing a solution of 10 ml of each $CdCl_2$ (1mM), Na_2TeO_3 (0.25 mM) and MSA (3 mM) in the above buffer solution in a two-necked flask at room temperature. To ensure complete mixing of precursors, the reaction mixture is put under vigorous stirring for 5 min followed by rapid addition of 20 mg of $NaBH_4$. After 5 min, the flask is attached to a condenser and put under refluxion at 100°C under open-air condition. Samples are collected from the room temperature reaction as well as from the refluxing solution with 1 hr interval to obtain a size series of QDs.

To synthesize Mn^{2+} doped CdTe QDs, the above procedure is repeated and Mn dopant is added to the CdTe nuclei formed, just after the reaction is put under refluxion at 100°C. A molar ratio of 1:22 is maintained between the precursors of Mn dopant and Cd precursor. For the synthesis of doped QDs, initially the dopant, $Mn(St)_2$ is synthesized from $MnCl_2$ and stearic acid [10]. To describe it briefly, initially three precursors are prepared by mixing 5.7 gm of steraic acid in 30 ml of methanol (20 mmol), 1.44 ml of TMAOH in 10 ml of methanol (20 mmol) and 1.62 gm of $MnCl_2$ in 10 ml of methanol (10 mmol). The first precursor is melted at 50-60 °C for complete dispersion. Then second precursor is added to it and stirred for 15 min. The third precursor is then added dropwise with vigorous stirring and stirring is continued for another 30 min. White precipitate is separated and washed with hot water and hot methanol to remove formed NH_4Cl and free stearic acids.

4.3 Results and discussion:

4.3.1 CdTe QDs:

The X-ray diffraction and HR-TEM image of the MSA@CdTe QDs along with the fast Fourier transform (FFT) pattern, particle size distribution and singular particle are shown in Figure 4.1. The average crystallite size is estimated as ~1.5 nm from the XRD pattern analysis using a pseudo-Voigt profile shape function and subsequent single-line analysis, based on the equivalent Voigt representation. The XRD reflections of CdTe QDs synthesized under prolonged refluxing in the presence of mercaptosuccinic acid are intermediate between the values of pure cubic CdTe and a pure cubic CdS crystal [Figure 4.1 (a)]. Table 4.1 shows the 2θ values for the planes in both the crystals in their bulk form while the same are obtained for the developed QDs at 27.05 and 43.78 respectively. Due to the small size of the dots, the background intensity is very high in this case and hence the obtained data do not provide unambiguous evidence for CdTe and CdS. Analyzing the FFT from the particle, the SOLZ (second order Laue zone) and HOLZ (higher order Laue zone) rings are found to be corroborating to the planes of cubic CdTe (indexing is done according to International Center for Diffraction Data, PDF No. 00-010-0207). But, for the FOLZ (first order Laue zone) ring, the d-spacing is found to be 0.264 nm which is not matching exactly with CdTe or CdS phases. However it is very close to that of the (101) plane of cubic CdTe (0.26368 nm, JCPDS, File No.

658076). These results indicate that the particles consist of cubic CdTe phase only and no any CdS formation occurs even after prolonged refluxion at moderate temperature.

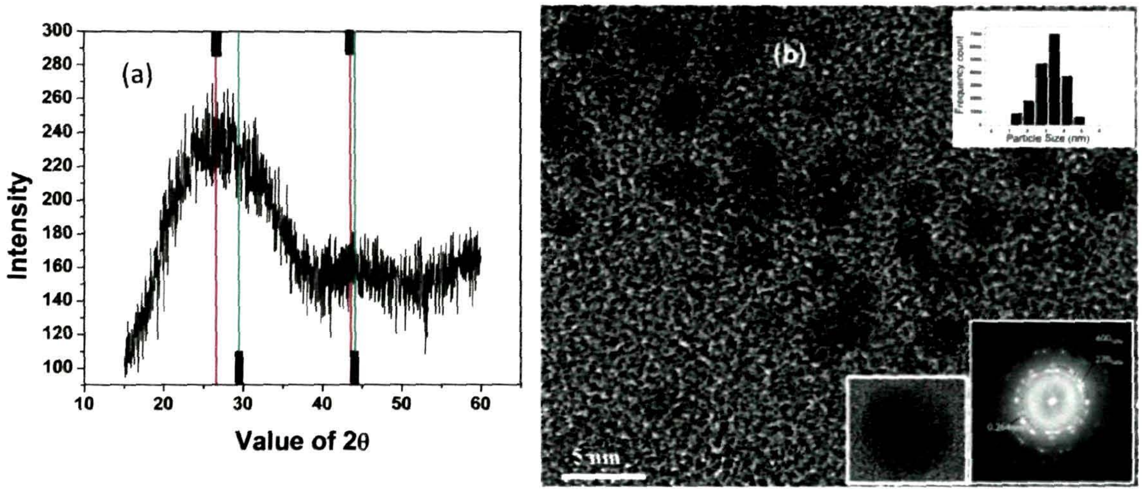

Figure 4.1 (a) XRD pattern of CdTe quantum dots. The red line shows the exact peak positions of CdS and green line shows that of CdTe crystals, (b) HRTEM image of CdTe QD along with insets showing the single particle, Fast Fourier Transform (FFT) from it and size distribution of QDs as estimated from HRTEM image.

Table 4.1 Standard XRD peaks of CdTe and CdS bulk crystals

CdTe (cubic)		CdS (cubic)	
Value of 2θ	(hkl)	Value of 2θ	(hkl)
29.49	001	26.45	111
43.93	101	43.88	220

HR-TEM investigations of 4 hr refluxed MSA@CdTe QDs corroborate XRD analysis results. As observed from Figure 4.1(b), the thiol capped CdTe QDs are monodispersed and well separated from each other. The average particle size of the QDs after 4 hr of refluxing is found to be 3.5 nm from the estimated size distribution graph from HR-TEM image as shown in inset of Figure 4.1(b). Another inset of this figure shows the singular particle with spherical morphology.

Figure 4.2 shows the FTIR spectra of representative MSA@CdTe QDs. The broad peak observed at 3432 cm^{-1} is due to O-H$_{stretch}$ vibration and the sharp peak at 1700 cm^{-1} is due to free C=O$_{stretch}$ vibration of mercaptosuccinic acid [11]. Absence of S-H$_{stretch}$ peak at 2500 cm^{-1} and presence of free carbonyl peak indicates that MSA is adsorbed to CdTe surface through S atom.

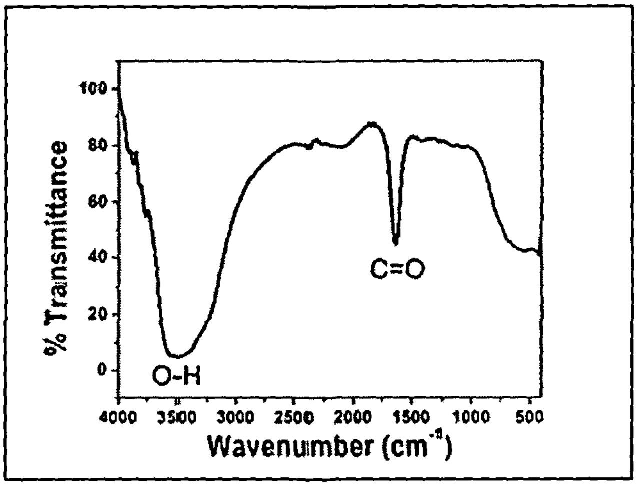

Figure 4.2 FTIR spectra of MSA@CdTe QD.

Figure 4.3(a) shows typical absorption spectra of the size series of CdTe QDs. The spectra were measured on as prepared QD colloidal solution as well as on the samples taken out from the refluxing reaction mixture at an hr interval of time. All samples show well distinct single absorption peak, tuneable in the range from 469 nm to 591 nm. The peak has been assigned the excitonic transition $1S_{3/2}$-$1S_e$ [12-13]. Inset of Figure 4.3(a) shows the plot of calculated particle size of each fraction taken out from the refluxing mixture. It is obvious that the quantum dots are in the strong confinement regime since the largest size is lesser than the exciton Bohr radius in bulk, a_B = 7.3 nm [14]. Figure 4.3(b) shows size dependent extinction coefficient (ε) values per mole of the nanocrystals of each size fraction and the plot of energy band gap values. The sizes and the extinction coefficient (ε) values of the CdTe QDs were calculated according to the method proposed by Peng *et al.* in 2003 [15]. The diameter of the CdTe QDs can be estimated from the relationship.

$$D = (9.8127 \times 10^{-7})\lambda^3 - (1.7147 \times 10^{-3})\lambda^2 + (1.0064)\lambda - (194.84) \qquad (1)$$

where λ is the wavelength of first excitonic absorption peak.

Then the extinction coefficient of the CdTe QDs are calculated from the equation

$$\varepsilon = 10043\,(D)^{2.12} \qquad (2)$$

Though it was predicted theoretically that the oscillator strength or ε values per mole of the particle are independent of particle size [16-17] but the proposed relation between extinction coefficient and particle size by a definite power law (Equation 2) has also been supported by the fact that the oscillator strength of the relevant optical transition increases with the size of the crystallite as long as the excited state is coherent [18]. In this case, the exciton energy is greater than the electron and hole size-quantization energies.

The HOMO-LUMO gap is calculated as a function of particle size applying the formula based on effective mass approximation combined with the Coulomb interaction within the strong confinement regime for quantum dot [19].

$$\Delta E_{g,\mathrm{eff}} = E - E_g + R_y = (\hbar^2\pi^2)/2\mu R^2 - (1.786e^2)/\epsilon' R + 0.752R_y \qquad (3)$$

where, E_g = 1.606 eV is the band gap energy of bulk CdTe, R is the radius of the dot, $\mu = 0.0774m_0$ is the reduced mass of an electron mass $m_e^* = 0.096m_0$ and a hole mass $m_h^* = 0.4m_0$, $\epsilon' = 7.1$ is the dielectric constant and $R_y = 10$ meV is the exciton Rydberg energy.

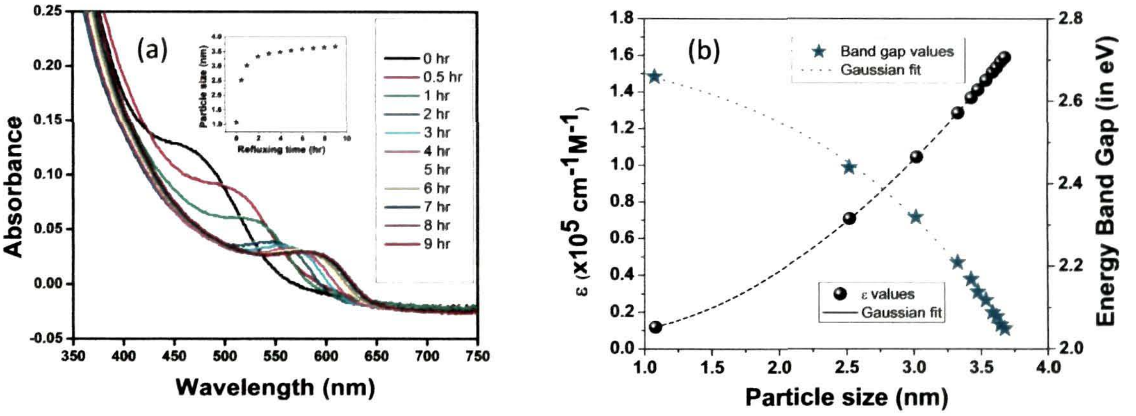

Figure 4.3 (a) UV-Visible absorption spectra and inset shows the estimated particle sizes and (b) extinction coefficient and band gap energy of size series of CdTe QD.

From Figure 4.3(b), it is observed that the largest size fraction of 3.68 nm quantum dot possesses the smallest band gap of 2.05 eV while the bulk CdTe has the band gap of 1.44 eV only, at room temperature. This blue shift of band gap energy as well as the absorption edge [Figure 4.3(a)], with decreasing particle size is due to the quantum confinement effect. The change in kinetic energy due to quantum confinement effect will increase the band gap and the energy separation of allowed transitions near the absorption edge [20].

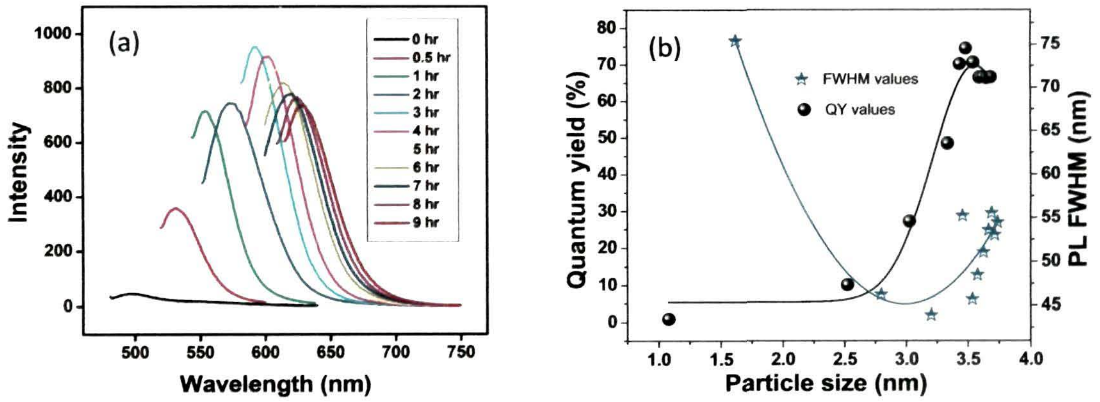

Figure 4.4 (a) PL spectra (b) Quantum yield and PL FWHM values for the size series of quantum dots (The black line is to guide the eye).

As evident from Figure 4.4(a), the PL spectra of the CdTe QDs are tuneable in the emission range from 497 nm to 628 nm. The QD emitting at 592 nm (size 3.48 nm), obtained after refluxing for 4 hours is found to possess the highest emission efficiency of ~74% as observed from Figure 4.4(b) [Quantum efficiencies are calculated by comparing with Rhodamine 6G] [21]. This can be explained on the basis of the dynamic growth process of quantum dots. When growth and dissolution are in equilibrium, the nanocrystals possess the highest photoluminescence quantum efficiencies and the best photostability because those particles are supposed to have zero growth rate and highly ordered surfaces [22]. In contrast, the nanocrystals grown under conditions far away from the equilibrium, are supposed to possess a rougher surface with various defects giving rise to nonradiative recombination pathways [23]. However, the PL FWHM values [Figure 4.4(b)] are in the range of 44-75 nm indicating the narrow size distribution of the QDs.

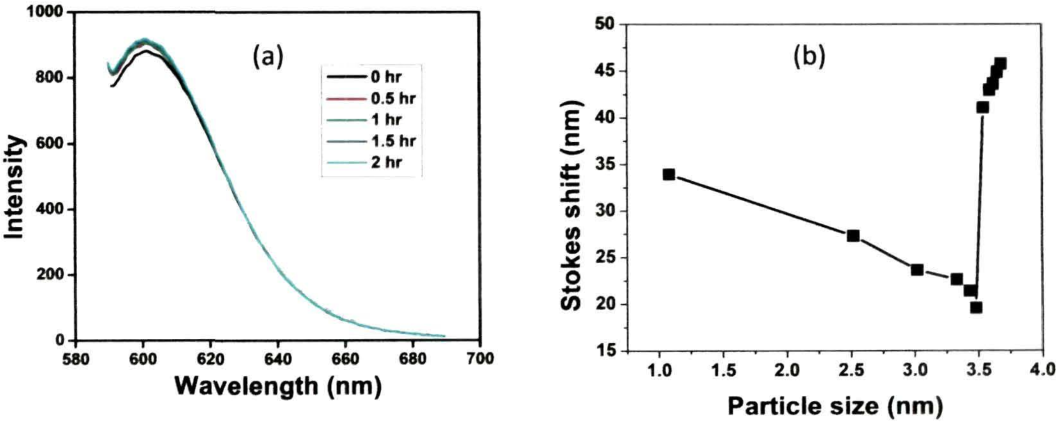

Figure 4.5 (a) Photostability study of highest QY size fraction QD and (b) Stokes shift values of the size series of QDs. The black line is to guide the eye.

Photoetching study was carried out with the highest PL efficiency fraction of QD and enhanced photoluminescence is observed with increase in photoetching time [Figure 4.5(a)]. This increase can be attributed to the fact that UV irradiation is useful in removal of dangling bond associated with unsaturated Te atoms present on the surface which act as a hole trap through annealing [22]. But no blue shift in PL spectra of photo etched QD is observed in this case which confirms the prior better quality surface of the QD with lesser defects. Moreover, it is observed that the PL spectra got red shifted with respect to absorption spectra which indicates that emission is from radiative recombination in shallow surface states. To examine this, we have plotted the Stoke's shift graph with respect to particle size [Figure 4.5(b)]. It is seen that the size fraction of QD having the highest PL efficiency is having the smallest Stokes shift which can be related to a detrapping of carriers from extremely shallow trap levels. On the other hand, wider distribution of trap states in the other QDs leads to stronger nonradiative energy dissipation due to unfair surface quality, resulting in higher Stokes shift [24-25].

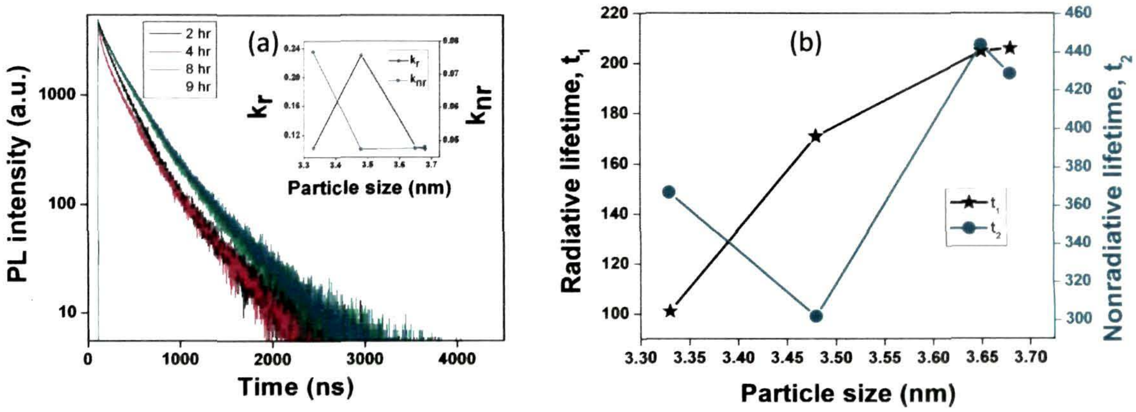

Figure 4.6 (a) PL decay curves measured at the respective emission peak wavelengths for four different sized CdTe QDs. The inset shows the plot between decay rate constants against particle size and (b) Decay lifetimes of the four QDs.

To see the radiative or nonradiative decay time of the excited states of the quantum dots, time resolved photoluminescence (TRPL) characterization has been carried out. Figure 4.6(a) shows decay curves of four different sized QDs. The curve of each sample is fitted with chi^2=1, using a biexponential function, resulting in a shorter lifetime equal to 101-206 ns, and longer one equal to 302-444 ns. The fitted equation is:

$$y = y_0 + A_1 \exp(-x/t_1) + A_2 \exp(-x/t_2) \tag{4}$$

The shorter lifetime can be attributed to the intrinsic radiative recombination of excitons while the longer lifetime can be associated with involvement of surface states in the exciton recombination process leading to non radiative emission [26]. Figure 4.6(b) shows the plot of both radiative and non radiative decay time of the same four different sized QDs. From the figure, it is evident that the QD fraction of size 3.48 nm, exhibiting the smallest Stoke's shift [Figure 4.5(b)], is having the smallest non radiative lifetime also. To obtain a quantitative information about recombination processes of luminescence of QDs, the radiative (k_r) and nonradiative rate constants (k_{nr}) have been calculated out by taking into account the quantum efficiencies (QY) and decay lifetime (τ) of the QDs. The equations used are [24]:

$$\frac{1}{\tau} = k_\mathrm{r} + k_\mathrm{nr} \tag{5}$$

$$\mathrm{QY} = \frac{k_\mathrm{r}}{k_\mathrm{r} + k_\mathrm{nr}} \tag{6}$$

$$k_\mathrm{r} = \frac{\mathrm{QY}}{\tau} \tag{7}$$

The inset of Figure 4.6(a) shows the plot of both radiative and nonradiative rate constants against the four QD sizes. From this figure, it is clear that the QD size fraction of 3.48 nm, obtained after 4 hr of refluxion, is having the minimum nonradiative decay rate which is corroborating to the PL quantum efficiency and Stoke's shift results. This confirms the presence of least amount of surface defects on it to behave as trap for excitons due to its formation at the equilibrium of growth and dissolution processes as explained before.

4.3.2 Mn doped CdTe QDs:

With the ICP technique the amount of Mn and Cd in the Mn:CdTe d dots is determined. From this result the Mn/Cd at. % is found to be 7 which is ~3 times lower than the targeted value of 22 at. %.

Figure 4.7(a) presents the EDX graph of $Mn(St)_2$ showing the presence of only Mn, C and O and impurities like Cl, N are absent in it. Figure 4.7(b) is the UV-Visible absorption spectra of Mn:CdTe d dots. The absorption corresponds to the excitonic absorption in the QDs. Here, refluxion was done upto 18 hr. An interesting behaviour is observed in the absorption spectra of the d dots. After usual red shifting of the absorption peak position with increasing refluxion time of the dots, there appears a lower wavelength peak in the absorption spectra along with the initial peak. With further refluxion, the initial peak starts decreasing in intensity and finally disappears while the new peak starts red shifting. We have observed that as prepared CdTe fraction shows the absorption at 460 nm and after Mn addition and then on refluxing upto 7 hr, this peak has been shifted to 600 nm. But in the 8 hr sample's spectra, a hump appears at 400 nm and the peak at 615 nm gets detensified. With further refluxed samples the newly observed peak is the only peak and shows red shifting upto 430 nm in 16 hr sample. But again a new peak at 274 nm appears in the spectra of the sample of 17 hr refluxion and the earlier peak diminishes which is observed in 18 hr sample too.

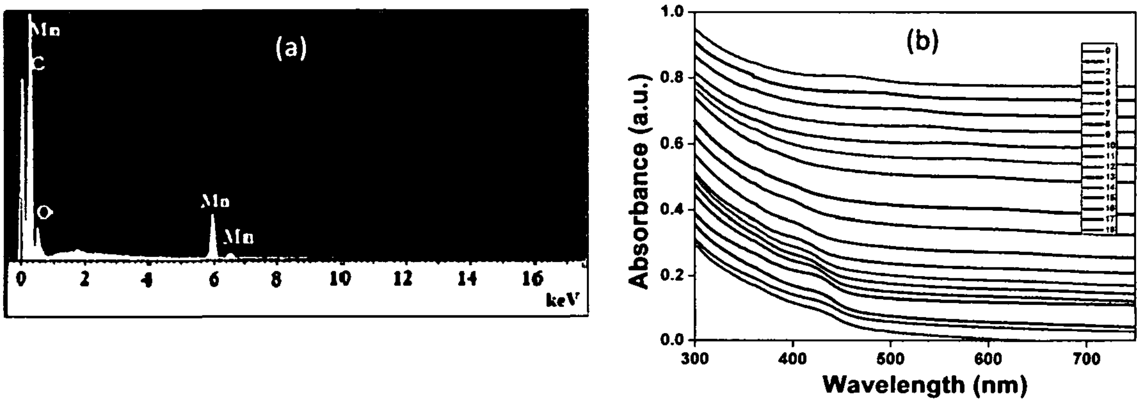

Figure 4.7 UV-Visible absorption spectra of Mn:CdTe QD.

In the above spectra [Figure 4.7(a)], it is observed that the higher wavelength peak diminishes on appearance of the lower wavelength peak with continuous red shifting instead of coexistence of the two. Presence of more than one peak in the absorption spectra in case of ZnSe quantum dots was reported as discontinuous growth [27]. But complete disappearance of one peak on evolution of the second one leads to the assumption of disintegration followed by saturation in growth. This kind of growth and disintergration of nanocrystals was observed earlier also by our group in case of iron oxide nanoparticles with heat treatment holding time [28]. To have a better account of the phenomenon, the variation of size (obtained theoretically) w.r.t. refluxing time is plotted in Figure 4.8(a). The sizes of the samples were calculated using Equation 1. For all the samples, emerging peak positions are counted for size calculation rather than the diminishing peaks. Though the calculated sizes are not obtained as exact value [indicated by negative values in Figure 4.8(a)], but the trend of growth, disintegration and again growth is clearly observed. To see the possibility of nanocrystal disintegration with increase in refluxion time in case of pristine CdTe the same refluxing procedure is carried out for 18 hr but no such behaviour is observed other than saturation in growth after sometime.

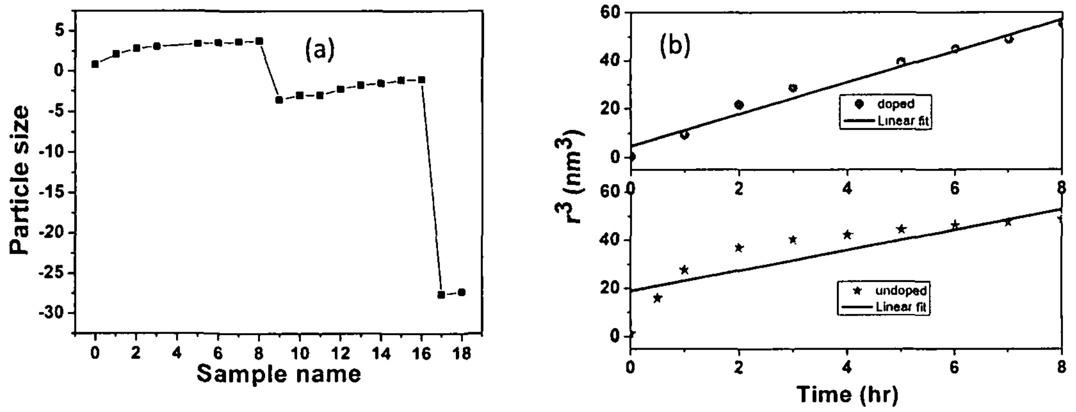

Figure 4.8 (a) Estimated particle sizes and (b) LSW plot of Mn:CdTe QD with refluxing time variation.

To explain the phenomenon of growth and disintegration, two points are worthy to be mentioned beforehand: (i) lower activation energy is required for diffusion of atoms in liquid phase solution and (ii) smaller size of Mn atom as compared to Cd, facilitates the diffusion of Mn atoms towards the surface of the growing nanocrystals by self purification method [29]. Moreover, the mercaptosuccinic acid ligand has similar affinity towards Cd and Mn as both of these are in +2 oxidation state. Hence there is the maximum probability of the presence of surface adsorbed Mn atoms in the d dots which is thought to be the origin of this unusual behavior. To have a quantified explanation of it, we have drawn the LSW plot for both doped and undoped CdTe QDs refluxed upto 8 hr [Figure 4.8(b)]. From the slopes of the LSW plots of d dot and q dots, the ripening reaction coefficients (K values) are obtained as 6.5618 and 4.2223 respectively. LSW plots are developed according to Equation 8, shown below [30]:

$$r^3 - r_0^3 = Kt \qquad (8)$$

where, r_0 is the average initial size of the original nanocrystals before ripening occurs, r is the average size of nanocrystals after ripening occurs, K is the ripening rate coefficient and t is the ripening time. It is seen that surface adsorbed Mn promotes ripening of the d dots as well as disintegration into smaller fraction after saturation in growth occurs. Increase in strain experienced by the dopant ions due to lattice mismatch during the growth of the host crystal structure may be thought of as the reason behind it.

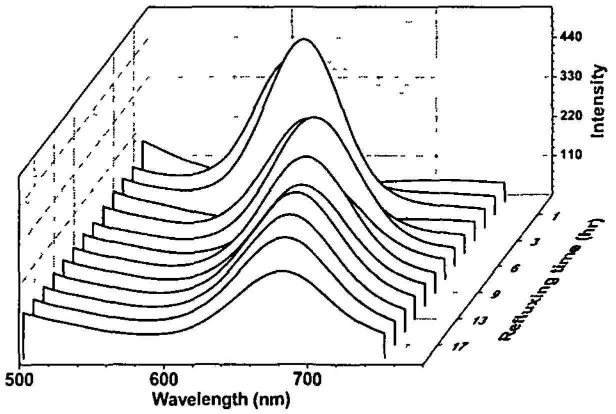

Figure 4.9 PL spectra of Mn:CdTe d dots.

In case of d dots, the absorption peak is due to the excitonic absorption of the host materials but the emission peak may not correspond to it. Because the excited electrons undergo transition to 3d states of Mn^{2+} ions and hence are responsible to Mn^{2+} d-emission assigned as $^6A_1 \longleftarrow {}^4T_1$ transition but because of the smaller orbital spread of atomic like states of Mn^{2+} than the NC size, there is no significant effect of NC size on dopant emission [31]. The PL spectra shown in Figure 4.9 for the synthesized d dots exhibits a continuous red shift of emission peak with increase in refluxion time of the samples. The observed red shift is from 610 nm to 678 nm for samples with 1-18 hr refluxion. But, it is not in agreement with the absorption spectra (Figure 4.7) as there is blue shift in the absorption peak at intervals of refluxing period, and hence assigning the emission peak as only excitonic emission is difficult. So, this emission peak can be considered as the surface-adsorbed Mn^{2+}-related emission. And the continuous red-shifting of emission peak is attributed to increasing symmetry of the lattice field around the surface Mn atoms with growth of the host crystal on refluxing. Because of this the d-orbitals of the Mn centre experience less electric field difference along different directions and hence a lesser crystal field splitting [10].

From the PL intensity plot of the d dots (Figure 4.10), it is observed that sample 2 possesses the highest intensity emission peak. Here, sample 0 is the as prepared CdTe fraction collected before refluxing while sample 1 is the fraction just after addition of Mn dopant. Sample 2 is Mn:CdTe collected after 1 hr refluxion and hence sample 19 is the fraction with 18 hr refluxion. This observation again points towards the assumption of the PL emission peak originating from surface-adsorbed Mn^{2+} ions as just after the addition of dopant the adsorption of it at the NC surface will be the highest. With increase in refluxion time, growth of the NC occurs via ripening and though by self purification mechanism Mn^{2+} ions (impurity) are pushed out towards surface still the number density of dopant ions on surface will be lower than the instant doping situation. On the other hand, the rest portion of the plot does not follow any regular trend due to unambiguous reason. One of the obvious cause is that NCs which are already in quantum confined region and hence have larger surface to volume ratio, have greater contribution from surface adsorbed Mn^{2+} emission for the higher sized NCs. From quantum yield calculation, sample 2 is found to be possessing the highest emission efficiency among Mn:CdTe as ~58%.

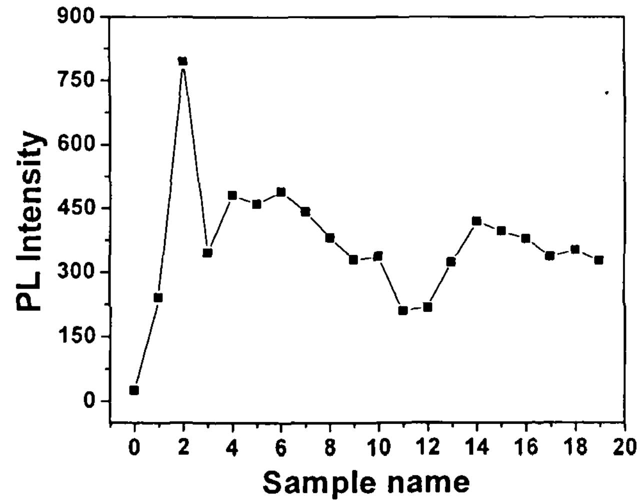

Figure 4.10 PL intensity plot of Mn:CdTe d dots.

From TRPL plot of the d dots shown in Figure 4.11(a), it is evident that the PL emission is not due to core doped Mn^{2+} ions as decay lifetime associated with such sp-d transition is of msec order [32]. The PL decay curve of the samples show biexponential decay behavior. The extremely short lifetime corroborates to the presence of surface adsorbed Mn^{2+} ions in the d dots. Because when the excited defect states (mainly surface states) and the Mn^{2+} ions coexist, then there is the probability of nonradiative energy transfer from the excited defect states to the Mn states [33] and results to rapid decay via surface adsorbed d emission. The schematic diagram of probable electronic transitions in this regard is depicted in Figure 4.11(b).

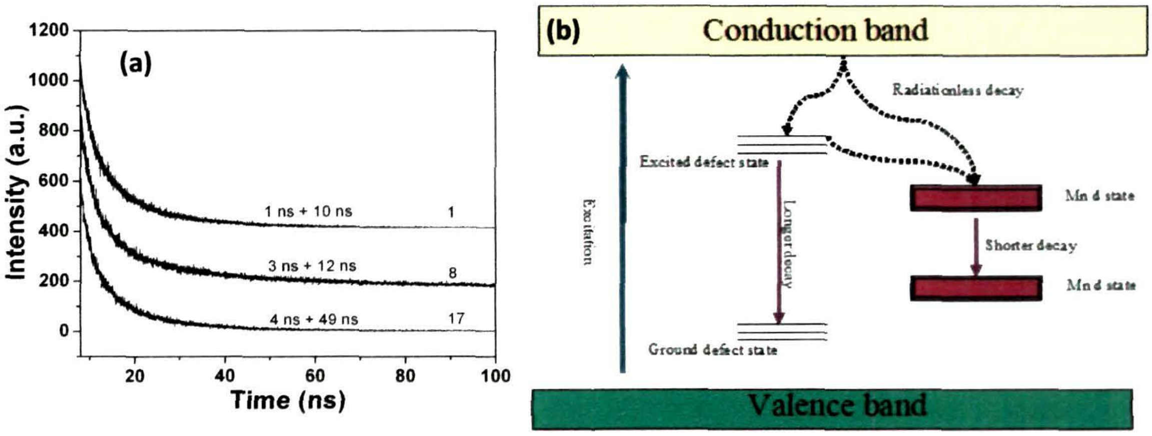

Figure 4.11 (a) TRPL of three Mn:CdTe d dots representative of different refluxion times and (b) schematic diagram of probable electronic transitions in this case.

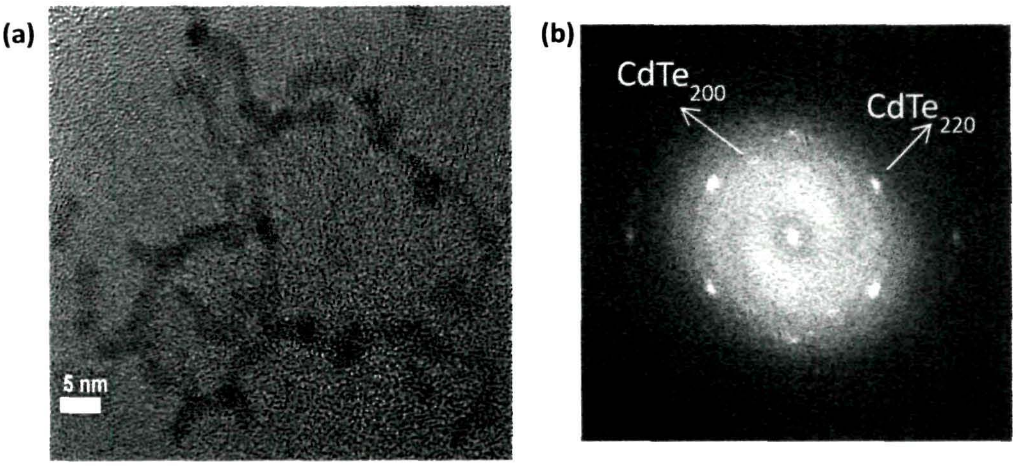

Figure 4.12 HRTEM images of (a) 12 hr refluxed Mn:CdTe d dots and (b) SAED pattern.

From the HR-TEM images (Figure 4.12), pearl necklace aggregates of Mn:CdTe d dots are observed, while for pristine CdTe no such feature is evidenced [refer Figure 4.1(b)]. Pearl necklace formation in CdTe and Mn doped CdTe after partial removal of stabilizer, was earlier assumed to be due to dipole-dipole interaction between nanocrystals [33-34]. In the present experiment, this kind of self assembly is observed without performing any stabilizer removal process. Presence of surface-adsorbed Mn^{2+} ions may have some role in it, which requires extensive studies on crystallographic and magnetic properties of the system. On the other hand, from the SAED pattern, the spots are identified as diffraction spots of (200) and (220) planes of cubic CdTe phase.

Part B

4.4 Synthesis of organic dye:

The dye is prepared by mixing 0.5 ml of ethanol, 10 μL of glutaraldehyde and 17 μL of oleylamine in a 20 ml beaker. It is allowed to stand for 24 hr without stirring. Next day, clear wine red solution of the dye is obtained.

4.5 Identification of the dye:

Glutaraldehyde is well known as cross linker used from earlier [35-36]. The structure of glutaraldehyde is dependent on the pH of the aqueous solution [37] for example; it remains as free aldehyde, in hydrated form or as its cyclic hemiacetal form in acidic or neutral pH conditions. But in alkaline aqueous solution, glutaraldehyde exists as polymer or as the hydrated form of the polymer. Also there is the evidence of formation of dimer of glutaraldehyde by aldol condensation between two molecules with the elimination of one water molecule in alkaline aqueous medium [38]. From the GC-MS data of our dye molecule (Figure 4.13), the major mass fraction is obtained to be $m/z=170$, which corresponds to the dimer of glutaraldehyde (structure I) formed by aldol condensation. This is possible in the less polar solvent ethanol in the presence of amine bases. Hence the plausible mechanism for crosslinking of glutaraldehyde with oleylamine will be through Michael addition reaction.

Such adducts (structure II) are stable and no reduction is necessary to stabilize [37]. The reactions of dimer formation of glutaraldehyde and then its addition with oleylamine are shown in Figure 4.14. The structure II is named as oleylamine complex or O-complex.

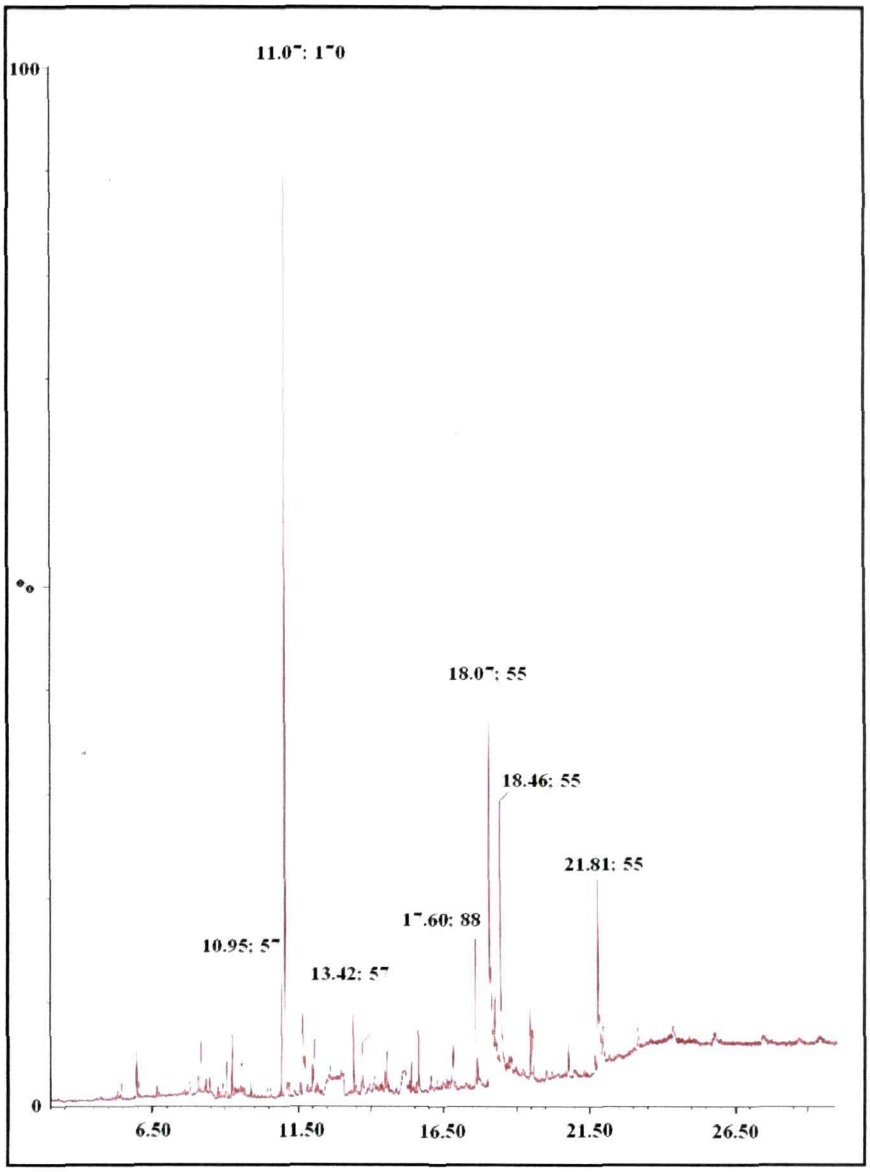

Figure 4.13 GC-MS spectrum of O-complex.

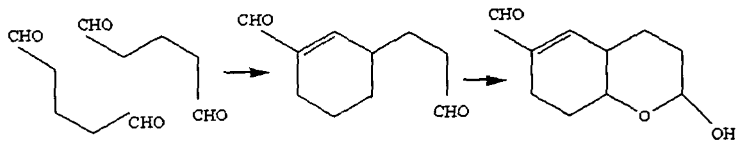

Structure I

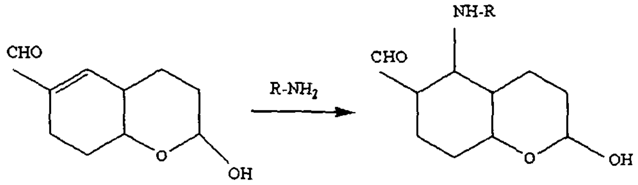

Structure II

Figure 4.14 Glutaraldehyde dimer (structure I) formation and Michael-type addition of glutaraldehyde with oleylamine (structure II). R-NH_2 is oleylamine molecule.

4.6 Result and discussion:

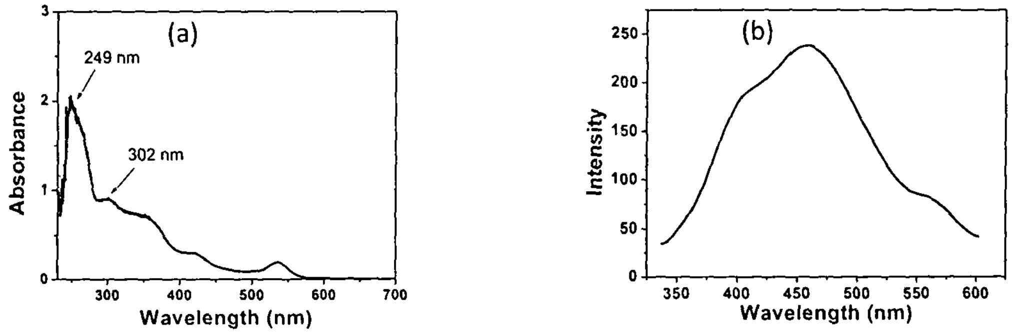

Figure 4.15 (a) UV-Visible absorption and (b) PL spectra of O-complex.

The optical properties of the O-complex are studied with the help of absorption and PL spectroscopy. From the UV-Visible spectra of the O-complex in Figure 4.15(a), the characteristic peaks of glutaraldehyde are seem to be present at 249 nm and 302 nm corresponding to $n \rightarrow \sigma^*$ and $n \rightarrow \pi^*$ transitions for aldehydic group respectively

[38-39].The PL peak of the O-complex is broad and asymmetric, characteristic of organic dye emissison peak [Figure 4.15(b)].

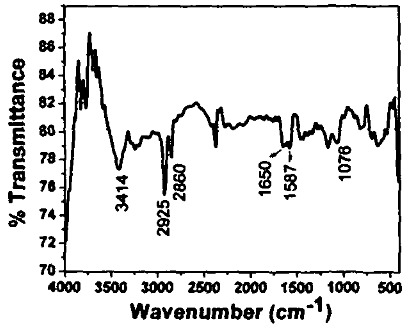

Figure 4.16 FTIR spectra of O-complex.

From the FTIR spectra of O-complex, the bands for oleylamine are distinctly observed (Figure 4.16). The single N–H$_{\text{stretching}}$ band at 3414 cm^{-1} and N–H$_{\text{scissoring}}$ band at 1587 cm^{-1} confirm the secondary amine character of oleylamine conjugated to glutaraldehyde (structure II). Also the bending modes of N–H are observed in the range 600-900 cm^{-1} [40]. Other than that, the C–H$_{\text{stretching}}$, C=C$_{\text{stretching}}$and C–N$_{\text{stretching}}$ modes are observed at 2860, 2925, 1650and 1076 cm^{-1} [40-41]. But the characteristic peaks of aldehyde moiety (i. e. the carbonyl feature) are not observed may be due to the long chain of oleylamine molecules have masked the glutaraldehyde part of O-complex.

4.7 Conclusion:

The fluorescent probes obtained from both inorganic and organic compounds have been studied in depth. The size controlled optical property tunability and its mechanistic understanding has been carried out on undoped and doped CdTe QDs. We find that the size fraction of pristine CdTe formed at the equilibrium of growth and dissolution processes possesses the highest luminescence efficiency at room temperature. The same size fraction exhibiting luminescence enhancement on photoetching, smallest Stokes shift and minimum nonradiative decay rate correlates to their prior better quality surface. On doping these CdTe QDs with Mn^{2+}, it is observed from UV-Visible absorption spectra that surface-adsorbed Mn^{2+} promotes faster growth rate of the d dots and then disintegration into smaller fraction after reaching saturation in growth with refluxing time. PL emission of the d-dots can be controllably tuned in a narrow optical window. TRPL measurements show extremely short lifetime, confirming emission due to surface-adsorbed Mn^{2+} states. On the other hand, the organic dye synthesized in a very simple method is named as O-complex formed by Michael type addition between oleylamine and dimer of glutaraldehyde molecules. The fluorescence property of O-complex is found to be governed by electronic transitions basically. Based on the characterization results, optimized size fraction of the undoped CdTe QD and O-complex are carried forward for developing hybrid along with magnetic nanoparticles.

References

[1] Dabbousi, B.O., *et al.* (CdSe)ZnS core-shell qds: synthesis and characterization of a size series of highly luminescent nanocrystallites. *J. Phys. Chem. B* **101** (46), 9463-9475, 1997.

[2] He, Y., et al. Microwave synthesis of water-dispersed CdTe/CdS/ZnS core-shell-shell quantum dots with excellent photostability and biocompatibility, *Adv. Mater.* **20** (18), 3416-3421, 2008.

[3] Mason, W.T. *Fluorescent and luminescent probes for biological activity*, 2nd ed. Academic Press, London, 1999.

[4] Gao, X., et al. In vivo molecular and cellular imaging with quantum dots, *Current Opinion in Biotechnology* **16** (1), 63-72, 2005.

[5] Resch-Genger, U., et al. Quantum dots versus organic dyes as fluorescent labels, *Nature Methods* **5** (9), 763-775, 2008.

[6] Derfus, A.M., Chan, W.C.W. and Bhatia, S.N. Probing the cytotoxicity of semiconductor quantum dots. *Nano Lett.* **4** (1), 11-18, 2004.

[7] Kirchner, C., et al. Cytotoxicity of colloidal CdSe and CdSe/ZnS nanoparticles. *Nano Lett.* **5** (2), 331-338, 2005.

[8] Pradhan, N., Battaglia, D. M., Liu, Y. and Peng, X. Efficient, stable, small and water-soluble doped ZnSe nanocrystal emitters as non-Cadmium biomedical labels, *Nano Lett.* 7 (2), 312-317, 2007.

[9] Ying, E., Guo, S., Dong, S. and Wang, J. Synthesis and bio-imaging application of highly luminescent mercaptosuccinic acid-coated CdTe nanocrystals, *PLoS ONE* **3** (5), e2222(1)-e2222(7), 2008.

[10] Pradhan, N. and Peng, X. Efficient and color-tunable Mn-doped ZnSe nanocrystals emitters: control of optical performance via greener synthetic route, *J. Am. Chem. Soc.* **129** (11), 3339-3347, 2007.

[11] Angelome′, P. C., et al. Hybrid non-silica mesoporous thin films, *New J. Chem.* **29** (1), 59-63, 2005.

[12] Kapitonov, A. M., et al. Luminescence properties of thiol-stabilized CdTe nanocrystals, *J Phys. Chem. B* **103** (46), 10109-10113, 1999.

[13] Rawalekar, S., et al. Ultrafast charge carrier relaxation and charge transfer dynamics of CdTe/CdS core-shell quantum dots as studied by femtosecond transient absorption spectroscopy, *J Phys. Chem. C* **114** (3), 1460-1466, 2010.

[14] Ma, S. M., et al. Ultrafast time-resolved DFWM of CdTe quantum dots in toluene, *J. of Physics: Conference series* **109** (1), 012025(1)-012025(4), 2008.

[15] Yu, W. W., et al. Experimental determination of the extinction coefficient of CdTe, CdSe, and CdS nanocrystals, *Chem. Mater.* **15** (14), 2854-2860, 2003.

[16] Rajh, T., Mićić, O. I. and Nozik, A. J. Synthesis and characterization of surface-modified colloidal CdTe quantum dots, *J Phys. Chem.* 97 (46), 11999-12003, 1993.

[17] Kayanuma, Y. Quantum-size effects of interacting electrons and holes in semiconductor microcrystals with spherical shape, *Phys. Rev. B* **38** (14), 9797-9805, 1988.

[18] Vossmeyer, T., et al. CdS nanoclusters: synthesis, characterization, size dependent oscillator strength, temperature shift of the excitonic transition energy, and reversible absorbance shift, *J Phys. Chem.* **98** (46), 7665-7673, 1994.

[19] Masumoto, Y. and Sonobe, K. Size-dependent energy levels of CdTe quantum dots, *Phys. Rev. B* **56** (15), 9734-9737, 1997.

---

[20] Patra, S. and Pradhan, S. K. Microstructure and optical characterization of CdTe quantum dots synthesized in a record minimum time, *J Appl. Phys.* **108** (8), 083515(1)-083515(9), 2010.

[21] Demasa, J. N. and Crosby, G. A. The measurement of photoluminescence quantum yields. A review, *J Phys. Chem.* **75** (8), 991-1024, 1971.

[22] Talapin, D. V., et al. Dynamic distribution of growth rates within the ensembles of colloidal II-VI and III-V semiconductor nanocrystals as a factor governing their photoluminescence efficiency, *J. Am. Chem. Soc.* **124** (20), 5782-5790, 2002.

[23] Chao, W., Qiang, M. and Xingguang, Su. Synthesis of CdTe nanocrystals with mercaptosuccinic acid as stabilizer, *J Nanosci. Nanotechnol.* **8** (9), 4408-4414, 2008.

[24] Byrne, S. J., et al. Optimisation of the synthesis and modification of CdTe quantum dots for enhanced live cell imaging, *J. Mater. Chem.* **16** (28), 2896-2902, 2006.

[25] Rogach, A. L., et al. Aqueous synthesis of thiol-capped CdTe nanocrystals: state-of-the-art, *J. Phys. Chem. C* **111** (40), 14628, 2007.

[26] Nonoguchi, Y., Nakashima, T. and Kawai, T. Temperature-dependent exciton recombination dynamics of CdTe nanocrystals, *J. Phys. Chem. C* **112** (49), 19263-19267, 2008.

[27] Zanella, M., Abbasi, A. Z., Scaper, A. K. and Parak, W. J. Discontinuous growth of II- VI semiconductor nanocrystals from different materials, *J. Phys. Chem. C* **114** (14), 6205-6215, 2010.

[28] Deb, P., et al. Anomalous agglomeration characteristics observed in iron oxide nanoclusters, *Phil. Mag. Lett.* **86** (8), 491, 2006.

[29] Bhattacharya, S., Zitoun, D. and Gedanken, A. Magnetic properties of $Cd_{1-x}Mn_xTe/C$ nanocrystals, *Nanotechnology* **22** (7), 075703(1)-075703(7), 2011.

[30] Sung, Y. M., Kwak, W. C. and Kim, T. G. Coarsening kinetics of Mn-doped CdSe nanocrystals, *Crystal Growth & design* **8** (4), 1186-1190, 2008.

[31] Nag, A., et al. Size-dependent tuning of Mn^{2+} d emission in Mn^{2+}-doped CdS nanocrystals: bulk vs surface, *J. Phys. Chem. C* **114** (43), 18323-18329, 2010.

[32] Sapra, S., et al. Emission properties of Manganese-doped ZnS nanocrystals, *J. Phys. Chem. B* **109** (5), 1663-1668, 2005.

[33] Tang, Z., Kotov, N. A. and Giersig, M. Spontaneous organization of single CdTe nanoparticles into luminescent nanowires, *Science* **297** (5579), 237-240, 2002.

[34] Ramasamy, P., Mamum, S. I., Jang, J. and Kim, J. Dopant induced diameter tuning of Mn-doped CdTe nanorods in aqueous solution, *Cryst. Eng. Comm.* **15** (11), 2061-2066, 2013.

[35] Nimni, M. E., Cheung, D., Strates, B., Kodama, M. and Sheikh, K. Chemically modified collagen: A natural biomaterial for tissue replacement, *J. Biomed. Mater. Res.* **21** (6), 741-771, 1987.

[36] Walt, D. R. and Agayn, V. I. The chemistry of enzyme and protein immobilization with glutaraldehyde, *Trends in Analytical Chemistry* **13** (10), 425-430, 1994.

[37] Migneault, I., Dartiguenave, C., Bertrand, M. J. and Waldron, K. C. Glutaraldehyde: behavior in aqueous solution, reaction with proteins, and application to enzyme crosslinking, *Biotechniques* **37** (5), 790-802, 2004.

[38] Tashima, T., et al. Structure of a new oligomer of glutaraldehyde produced by aldol condensation reaction, *J. Org. Chem.* **56** (2), 694-697, 1991.

[39] Manna, U., Dhar, J., Nayak, R. and Patil, S. Multilayer single-component thin films and microcapsules via covalent bonded layer-by-layer self-assembly, *Chem. Commun.* **46** (13), 2250-2252, 2010.

[40] Gerung, H., et al. Anhydrous solution synthesis of germanium nanocrystals from the germanium(II) precursor $Ge[N(Si)Me_3)_2]_2$, *Chem. Comm.* (14), 1914-1916, 2005.

[41] Shukla, N., Liu, C., Jones, P. M. and Weller, D. FTIR study of surfactant bonding to FePt nanoparticles, *J. Magn. Magn. Mater.* **266** (1-2), 178-184, 2005.

Chapter 5

Magneto-fluorescent hybrid nanosystems

5.1 Introduction:

Nanomaterials with novel engineered structures assure applications in many fields such as biological applications [1], superconducting materials [2], nanocatalysis [3], energy [4], environmental remediation [5] etc. Such exciting and potential applications have inspired the development of hybrid nanostructure having multifunctional attribute. Qunatum dots (QD) and magnetic nanoparticles are two prominent examples of such kind which have found enormous potential applications because of their advantageous properties. QDs possess excellent properties viz. photostability, narrow emission profile with broad excitation range, size dependent emission characteristic etc. for which they are of great interest in biomedical applications [6]. Also, organic dyes are used as optical imaging probe in this field and both QDs and organic dyes have some advantages and disadvantages as well. Similarly, magnetic nanoparticles possessing superparamagnetic property find immense importance in biomedical applications by facilitating magnetic resonance imaging [7], hyperthermia [8], magnetic separation [9] etc. Therefore, recent efforts have been directed towards designing nanocarriers that contain both fluorescent and magnetic nanocomponents producing a hybrid nanosystem with combined functionalities [10,11,12].These hybrids are hierarchical nanoarchitectures assembled from nanoscale units. SiO_2 and polymer are two potentially identified templates of hybrid nanosystems. However, silica based nanocarrier can lead to improved stability, low toxicity, higher biocompatibility of the hybrid and protects the nanocomponents against corrosion in the biological medium. In addition, the hydrolyzed silica surface contains a high coverage of silanol groups to which bioconjugation can be done conveniently. Above all these, the structure of silica can be tuned to porous structures which is beneficial in making the hybrid a potential carrier of drug and protein by embedding them in porous structures along with magneto-fluorescent bi-functionality. Studies have been carried out to understand the formation mechanism of the silica structure of the hybrid [13]. It is obvious that structure-property-application correlation study of hierarchically structured hybrid nanosystem is of immense importance along with its synthesis, to ensure its best applicability in any field.

Part A

5.2 Synthesis of hybrids of QDs and SPIONs:

5.2.1 Synthesis of silica hybrid of SPIONs:

Hybrid formation of SPION in silica was done by modified sol gel method [14], which involves hydrolysis and condensation of tetraethylorthosilicate (TEOS) into silica in alkaline condition at room temperature. First, 3.2 mg of stearic acid@SPIONs were dispersed in 0.5 ml chloroform and mixed with an aqueous solution of CTAB (30 mg in 3ml water). The mixture was stirred to make an emulsion and then heated at 60°C to evaporate chloroform. To a diluted amount of the aqueous iron oxide solution, 2ml of ethylacetate was added for better solubility. Then 0.48 ml of NH_4OH was added for making the solution alkaline followed by addition of 0.14 ml of TEOS with continuous stirring. After adding all these, the reaction mixture was stirred for 30 sec and aged for 3 hours. The precipitate was separated by centrifugation and washed with ethanol and water for three times. The obtained precipitate was dried in oven and then calcined at 540°C for 2 hr to remove the organic templates. This hybrid is named as A.

5.2.2 Synthesis of silica hybrid of SPIONs and CdTe QDs without template:

The silica hybrid of stearic acid@SPIONs and MSA@CdTe QDs is prepared without using any CTAB template. For the hybrid synthesis, initially the stearic acid coating of

SPIONs was replaced by DMSA ligand as described in Chapter 3, to make the nanoparticles hydrophilic. The synthesis of the silica hybrid comprises of mixing of equal volume of aqueous solutions of SPION and MSA@CdTe QDs (3.2 mg in 2 ml). Then the mixture was diluted with 40 ml water and put under magnetic stirring. Subsequently, ethylacetate (8 ml), NH_4OH (4.8 ml) and TEOS (0.8 ml) were added in sequence and the whole reaction mixture was stirred for ~ 6 hrs. After that a brown color gel was obtained by centrifugation which was washed three times with ethanol and water. It was dried in hot air oven first and then calcined at 540°C for 2 hr in furnace for removal of any organic material. This hybrid is named as B.

5.2.3 Synthesis of silica hybrid of SPIONs and CdTe QDs using template:

This procedure was accomplished in two steps. In the first step, MSA@CdTe QDs were functionalized with oleylamine to make them hydrophobic by following a glutaraldehyde cross-linking procedure [15]. For this, a solution was prepared by mixing 17 μL oleylamine and 10 μL glutaraldehyde in 0.5 ml ethanol. To it, 1 ml of carbonate buffer of pH 10 and 2 ml of aqueous MSA@CdTe QD were added and kept for 1 hr. After that, 200 μL of 0.6M $NaBH_4$ solution was added to it dropwise and left for 24 hr standing. Then, oleylamine functionalized CdTe QDs were found to be remained separated from the aqueous solution and were dispersible in chloroform. The hybrid synthesis procedure is same as that of hybrid A. The only difference is that CdTe is also CTAB stabilized and equal volume of both CTAB stabilized SPION and CdTe aqueous solutions are mixed together before hybrid formation. The precipitate formed was separated by centrifugation and washed with water and ethanol and dried in oven. The calcination was done at 540°C for 2 hr to remove the organic templates. This hybrid is named as C.

5.3 Results and discussion:

The schematic representation of magneto-fluorescent hybrid formation is shown in scheme 1. The hierarchical architecture leading to core shell structure of silica with nanoparticles in shell and hollow core of hybrids A and C is realized from the formation mechanism (Figure 5.1). The stearic acid@SPIONs in chloroform are entrapped in the hydrophobic core of the micelles formed by CTAB in aqueous solution. On drying at 60°C, chloroform gets evaporated forming a microemulsion. When this microemulsion is added with water, ethylacetate and TEOS; both ethylacetate and TEOS form droplets in alkaline aqueous medium, inside of which is hydrophobic with silicate. The hydrolysis of TEOS occurs at the water-TEOS interface and forms the shell. Therefore, TEOS and ethylacetate diffuse outward to get hydrolyzed while CTAB micelles, CTAB stabilized nanoparticles and water diffuse inward. However, since the core of the droplets are hydrophobic, so the hydrophilic species are confined in the Si-$(OH)_4$ network of the shell leaving the core empty. On drying, silanol groups are condensed to silica and calcination at high temperature (540°C) results in the removal of organic templates like CTAB, ethylacetate. Consequently, the hierarchical structure of mesoporous silica particles with nanoparticles in shell and hollow core are formed.

On the other hand, the nontemplated synthesis of magneto-fluorescent silica hybrid system i.e. hybrid B is based on the electrostatic forces of attraction between free Cd^{2+}, Fe^{3+} ions of nanoparticle surface and OH^{-} ions of silica surface as the MSA and DMSA coatings are assumed to be removed from QD and SPION surface during its synthesis due to stirring vigorrously for prolonged period (~6 hrs).

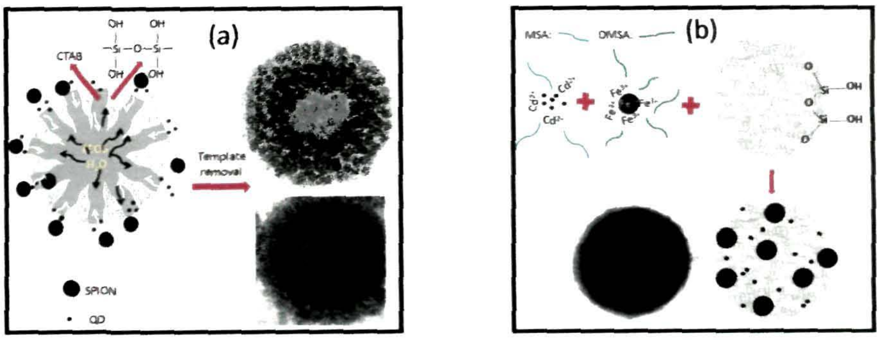

Figure 5.1 Schematic representation of formation of hierarchically structured hybrid (a) A and C and (b) B.

In order to substantiate the hierarchical architecture of the hybrids proposed through the above analysis, small angle X-ray scattering (SAXS) experiments were carried out with all the three hybrids. SAXS data has been analyzed in the light of multi component polydisperse spherical particle model. In such a case, the scattering intensity may be expressed by the cumulative contributions from various components

$$I_{total}(q) = I_{mag}(q) + I_{QD}(q) + I_{Pore}(q) + I_{grain}(q) \qquad (1)$$

where, *mag, QD, Pore* and *grain* refer to the magnetic nanoparticle, quantum dots, meso pores and overall grain i.e. silica particles, respectively. Each term in the RHS was expressed as

$$I_X(q) = C\int_0^\infty P_X(q,R)D_X(r)V_X^2(R)S_X(q,R)dR \qquad (2)$$

where, C is a scale factor that depends on the scattering contrast and the number density. $P_X(q,R)$ represents the form factor, $D_X(R)$, the radius distribution, $V_X(R)$, the volume of the particle of radius R and $S_X(q,R)$ represents the interparticle structure factor for the component X. The cross terms were neglected for simplicity. In order to estimate the overall grain size (i.e., the largest length scale), ultra small-angle neutron scattering (USANS) measurements were performed using the double crystal based medium resolution SANS instrument at the guide tube laboratory, Dhruva reactor, India. The average particle size was estimated by fitting polydisperse spherical particle model to the data. For sample C, two distributions in well separated length scale was observed.

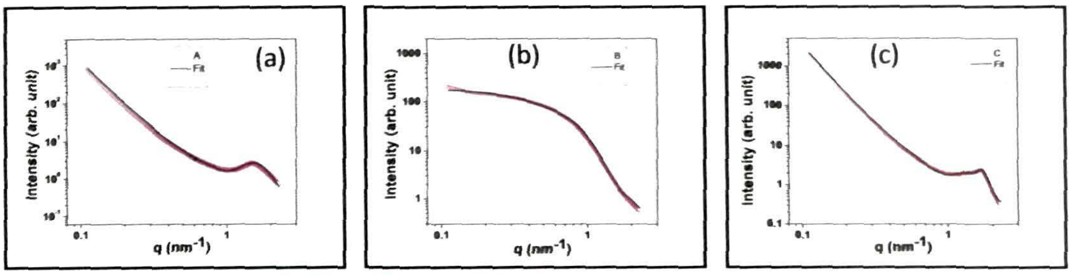

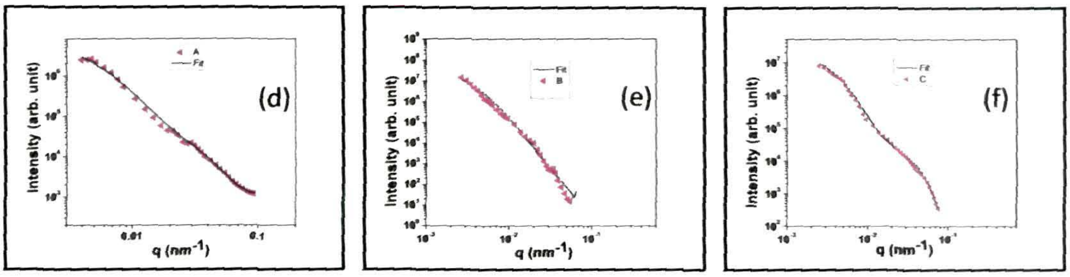

Figure 5.2 (a), (b), (c) SAXS and (d), (e), (f) USANS plots and the fittings of hybrid A, B, C respectively.

Table 5.1 The fitting parameters obtained from the fitting of model to SAXS data

Hybrid name	R_{SPION}	σ_{SPION}	$R_{Mesopor}$	$\sigma_{mesopore}$	$R_{Quantum\ dot}$	$\sigma_{Quantum\ Dot}$	R_{Grain}
A	4 nm	0.19	17 nm	0.259	—	—	94 nm
B	5 nm	0.20	—	—	2 nm	0.14	—
C	4.2 nm	0.54	16.2 nm	—	3.2 nm	0.27	—

Table 5.2 The fitting parameters obtained from the fitting of model to USANS data

Hybrid name	$R_{Grain\ 1}$	$\sigma_{Grain\ 1}$	$R_{Grain\ 2}$	$\sigma_{Grain\ 2}$
A	91 nm	0.25	170 nm	0.57
B	—	—	435 nm	0.67
C	110 nm	0.22	285 nm	0.59

Figures 5.2(a), (b), (c) show the small-angle X-ray scattering (SAXS) data measured for the powders of hybrids A, B, C respectively. The X-ray beam used is of

strength 8 keV and wavelength, λ = 1.5 Å. Hybrids A and C with hollow core and nanoparticles in the shell giving it an increased electron density, exhibit a stronger scattering, especially in the lower q region (< 0.1 nm^{-1}) predominant for the global core-shell structure [16]. Also, the SAXS patterns with shoulder at higher q region result from intraparticle interferences [17]. Here the scattering wave vector q is specified by $4\pi\lambda^{-1}\text{Sin }\theta$ (with 2θ as the scattering angle). In the higher q region, the scattering is mostly due to pores or is filled with nanoparticles. A model of multicomponent polydispersed spherical particle fits the data well. The fitted parameters include the overall grain size of 94 nm with mesopore of size 17 nm and SPION of 4 nm in hybrid A. While for hybrid C the analysis of fitted SAXS plot estimates SPION of 4.2 nm, QD of 3.2 nm and mesopore of size ~ 15 nm. The structure parameters so obtained are tabulated in Table 5.1 and are found to be consistent with those observed from following HR-TEM image analysis. In contrast, hybrid B, developed by without using any CTAB template, yields nonporous solid spheres whose size could not be determined from SAXS fitting parameters. Only the presence of the SPION of size 5 nm and QD of size ~2nm in the hybrids could be revealed from the analysis of hybrid B's SAXS plot.

Figures 5.2(d), (e) and (f) present the ultra small-angle neutron scattering (USANS) data of the threes hybrids A, B and C respectively. The neutron beam was monochromatized to a wavelength spread of 3.1Å. In order to check for possible aggregation in the samples, a q value as low as 0.003 nm^{-1} was reached. The samples were placed in Al container of diameter 1.5 cm and thickness 3 mm. From the figures, the extended SANS data to lower q are observed corroborating to the presence of aggregates in the samples. The fitting parameters of the SANS data as tabulated in Table 5.2 point towards the bimodal distribution of particles in hybrids A and C.

The hierarchical structure of the hybrids formed based on the nanoscale units like QD, SPION and mesopores have been revealed through above scattering analysis.

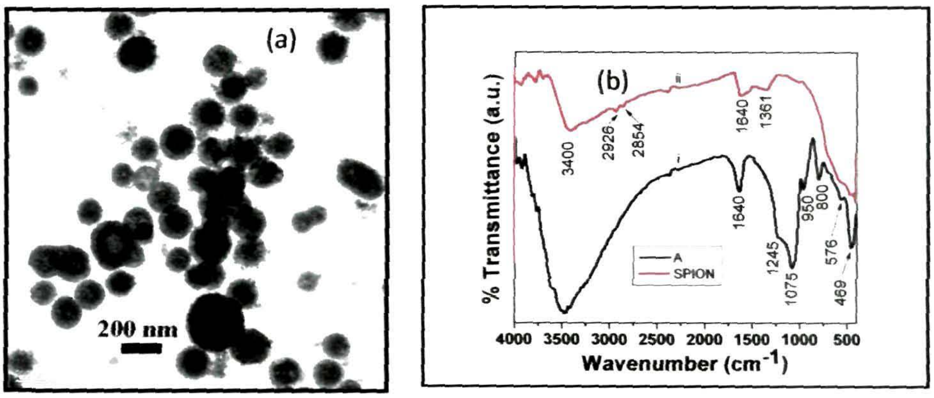

Figure 5.3 (a) HR-TEM image and (b) FTIR spectra of hybrid A (curve i) and stearic acid@SPION (curve ii).

Then the microstructural characterization of the three hybrids were carried out. From the HR-TEM image of hybrid A in Figure 5.3(a), the silica spheres with hollow core and thick shell with SPIONs (distinct by dark contrast) are observed. From the FTIR comparison curves between stearic acid@SPION and hybrid A in Figure 5.3(b), the silica embedment of iron oxide is distinct. For the stearic acid@SPIONs, apart from OH stretching band at 3400 cm^{-1} and Fe–O stretching band at 500 cm^{-1}, two intense bands appear at 1361 cm^{-1} and 1640 cm^{-1}. The earlier one is due to bending vibration of C-H in CH_3 group [18] and the later is assigned to O–H$_{\text{deformation}}$ [19] of stearic acid. The FTIR spectra of the hybrid exhibits the characteristic peaks for SiO_2. The sharp peak at 469 cm^{-1} is assigned to O–Si–O$_{\text{bending}}$, 800 cm^{-1} to Si–O–Si$_{\text{bending}}$ and 1075 cm^{-1} to Si–O–Si$_{\text{sym stretching}}$ vibration of SiO_2 [20]. Similarly, the 950 cm^{-1} band is due to the Si–OH$_{\text{stretching}}$ vibration of surface hydroxyl groups [20] and the shoulder peak at 1245 cm^{-1} may be the peak of optically weak oxygen antisymmetric stretch longitudinal-optic (LO) stretching mode [21]. The lower frequency bands at 576 cm^{-1} and 718 cm^{-1} are assigned to Fe–O$_{\text{stretching}}$ vibration and O–C–O$_{\text{bending}}$ vibrations respectively [22].

The results of the microstructural caharacterization of hybrids B and C are presented in Figure 5.4. In the FTIR spectra of hybrids B and C in Figures 5.4(a) and (d), almost same vibration bands of SiO_2 are observed as in case of hybrid A [refer

Figure 5.3(b)], confirming the presence of silica embedment. The FTIR spectra of MSA@CdTe QD and DMSA@SPION were explained in detail in the previous chapters.

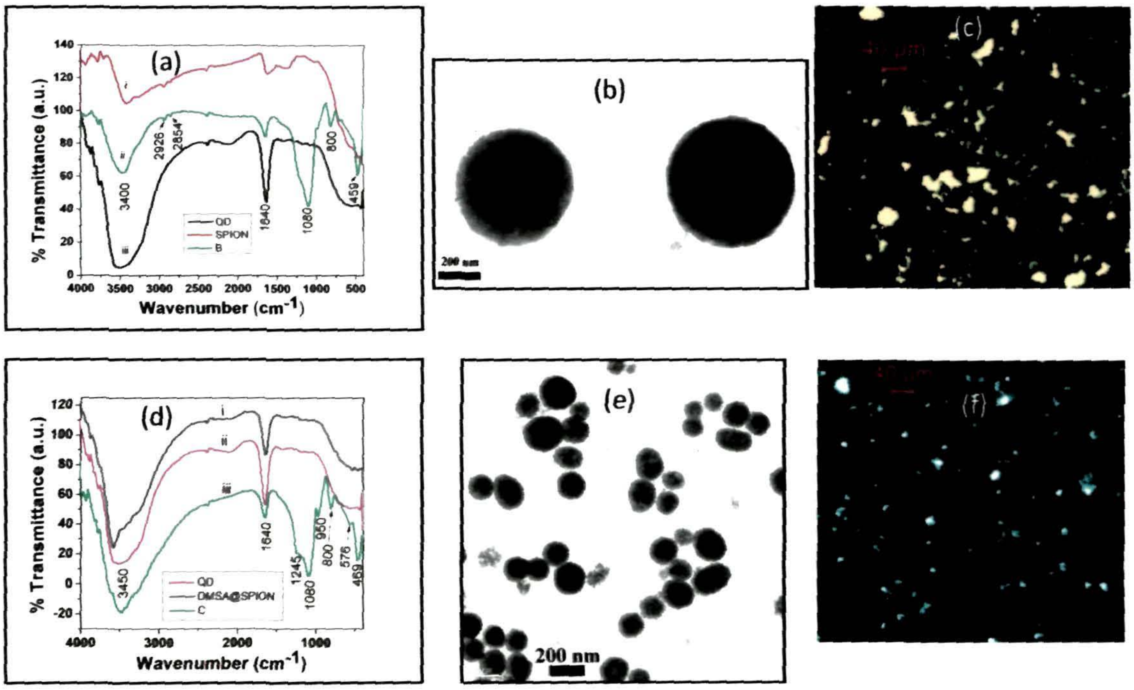

Figure 5.4 FTIR spectra of (a) stearic acid@SPION (curve i), hybrid B (curve ii), MSA@CdTe QD (curve iii), (d) DMSA@SPION (curve i), MSA@CdTe QD (curve ii), hybrid C (curve iii), HR-TEM images of (b) hybrid B and (e) hybrid C, Fluorescence microscopy images of (c) hybrid B excited with green light (Filter N2.1) and (f) hybrid C excited with UV light (Filter A).

From the HR-TEM image of Figure 5.4(b), the solid spherical silica particles of hybrid B of size ~ 400 nm are observed whereas from Figure 5.4(e), the silica particles of size ~ 200 nm of hybrid C are observed with nanoparticles present mostly at the shell. Grain 2 sizes obtained from SANS data match fairly with the corresponding HR-TEM investigation of the hybrids [refer Table 5.2]. On the other hand, the fluorescence microscopy images of hybrids B and C shown in Figures 5.4(c) and (f) respectively, corroborate to their fluorescent property.

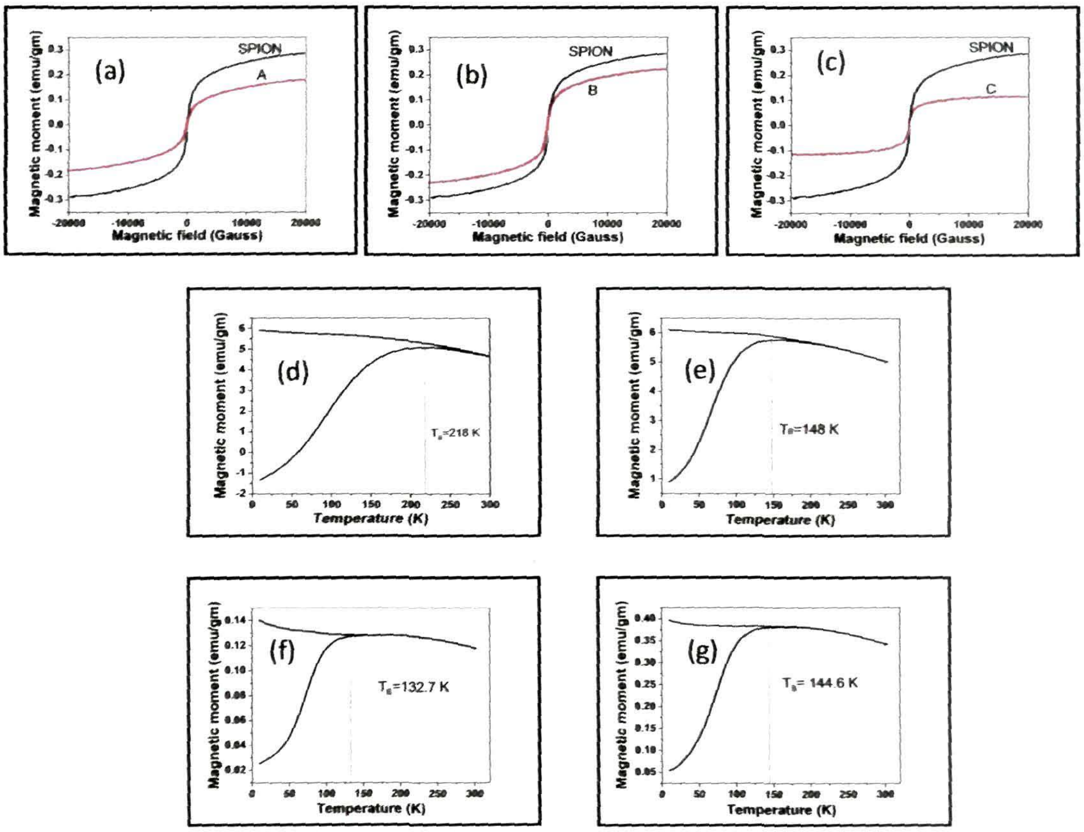

Figure 5.5 M-H characterization curves of hybrid (a) A, (b) B, (c) C with comparison to that of SPION. M-T characterization curves of (d) SPION, (e) A, (f) B and (g) C in presence of magnetic field 100 Oe.

A comparative magnetic property study of the SPION and its corresponding hybrids were done with the help of M-H and M-T characterization techniques. From the M-H characterization results, it is observed that the superparamagnetic character of SPION is retained after hybrid formation with SiO_2 and QDs though there is a decrease in the saturation magnetization after hybrid formation [Figures 5.5(a), (b) and (c)]. This is due to the diamagnetic contribution from the thick silica coating to the total magnetization of the hybrids.

From the M-T characterization plots of SPION as well as its hybrids with QDs and SiO_2, the irreversibility of ZFC and FC curves beyond irreversible temperature, T_{irr} and a maximum in the ZFC curve known as the blocking temperature, T_B are observed which further indicate to the superparamagnetic nature of the systems [23]. From Figures 5.5(d),(e), (f) and (g), it is observed that the T_B decreases with SiO_2 coating. This decrease is attributed to the reduction of the average effective volume, V_{eff} of the γ-Fe_2O_3 nanoparticles due to interfacial interaction between SiO_2 and outer layer of the iron oxide [23]. Whereas the reduction in V_{eff} is due to that the interaction may produce disordered Fe spins near the surface which should have a negligible contribution to the total magnetization of the sample. From the relation of Blocking temperature, $T_B = KV_{eff}/25k_B$, the decrease in T_B can be corroborated [24].

It is observed from the above study that magneto-fluorescent hybrids B and C do not differ much from each other as long as magnetic and fluorescent properties are concerned. Therefore, based on the detailed microstructural, magnetic and fluorescent property study of the developed systems, hybrid C is chosen for checking the multifunctional applicability in biomedical field due to their smaller size of around 200 nm, mesoporous structure and magneto-fluorescent characteristics. Prior to that, a compositional study of the hybrid has been carried out with XPS analysis.

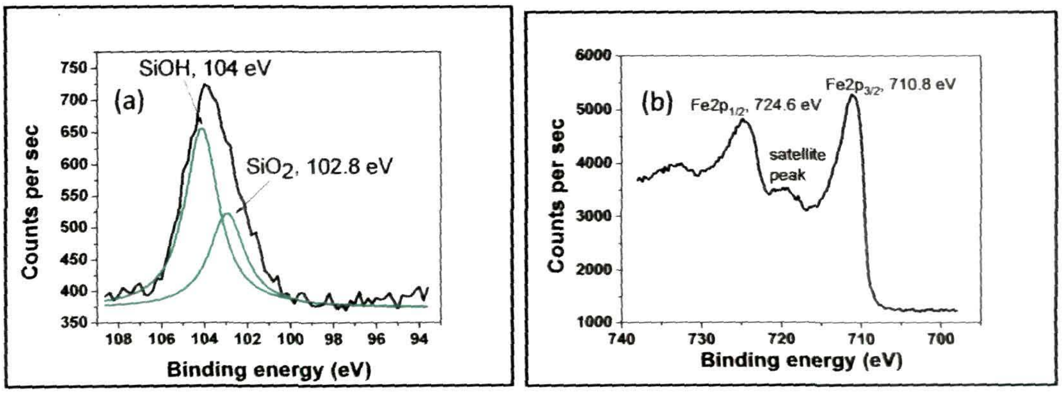

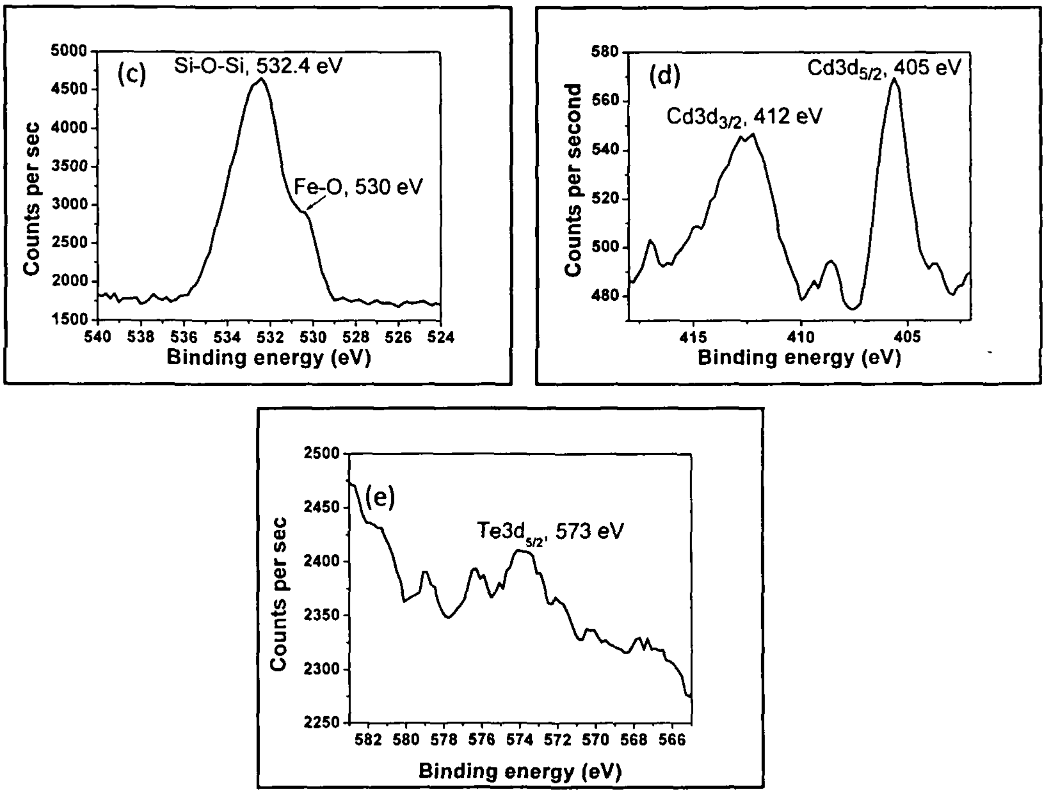

Figure 5.6 XPS spectra of (a) Si2p, (b) Fe2p, (c) O1s, (d) Cd3d and (e) Te3d peaks of hybrid C.

Figure 5.6(a) shows the XPS spectrum of Si 2p peak of hybrid C. The high binding energy peaks are observed for Si 2p due to oxidized species of Si. Among them, the peak at 102.8 eV is assigned to Si-O-Si groups whereas that at 104 eV to free Si-OH groups [25]. Presence of both Fe $2p_{3/2}$ peak at 710.8 eV and Fe $2p_{1/2}$ peak at 724.6 eV along with the satellite peak at 719.4 eV points towards the Fe^{3+} state of γ-Fe_2O_3 phase in the hybrid [Figure 5.6(b)] [26]. Two peaks are observed in the O 1s spectra at 532.4 eV and 530 eV [Figure 5.6(c)]. These are assigned to O atom bound to Si in SiO_2 and to Fe in γ-Fe_2O_3 respectively [26-27]. From Figure 5.6(d), Cd 3d lines are observed distinctly for Cd $3d_{5/2}$ at 405 eV and for Cd $3d_{3/2}$ at 412 eV which corroborates to the Cd^{2+} state of CdTe in the hybrid [28]. In accordance to it, the Te spectra shows the peak of Te $3d_{5/2}$ at 573 eV which confirms Te^{-2} state to be present in the form of CdTe [Figure 5.6(d)] [29].

Part B

5.4 Synthesis of silica hybrid of SPIONs and the fluorescent dye using template:

The preparation of the fluorescent dye has been described under the section 4.4 in chapter 4. The so obtained dye is dispersed in 0.5 ml of chloroform. Now in order to develop a hybrid of the dye and SPION in silica matrix, the individual components need to be stabilized with CTAB first. For that 3 ml solution of CTAB is made in water with a concentration of 1 mg/ml. Both CTAB and dye solutions are mixed and stirred vigorously for 1 hr. The formed emulsion is kept in oven for 15 min at 60°C to evaporate chloroform. Hence, an aqueous solution of CTAB stabilized dye is obtained. Also, the CTAB stabilization of stearic acid@SPION is done as explained in subsection 5.2.1.

Both the aqueous solutions of SPION and dye are mixed together and diluted with 20 ml water. After that 2 ml ethylacetate, 0.48 ml NH_4OH and 0.14 ml TEOS are added to it sequentially with stirring. Stirring is continued for another 30 sec and then the reaction mixture is allowed to stand for 12 hr. The pinkish precipitate is obtained by centrifugation and purification is done by washing with water and ethanol. To remove the organic templates viz. CTAB, ethylacetate etc., calcination cannot be done with this hybrid powder as it will lead to decomposition of the organic dye. Therefore, a novel extraction procedure is carried out to remove the water soluble templates. It comprises of mixing of 34 mg of hybrid in 15 ml of water by sonication for 30 min. Then, this solution is put under refluxion at 90°C for 12 hr with magnetic stirring. After that, refluxion is stopped and the product is separated by centrifugation.

5.5 Result and discussion:

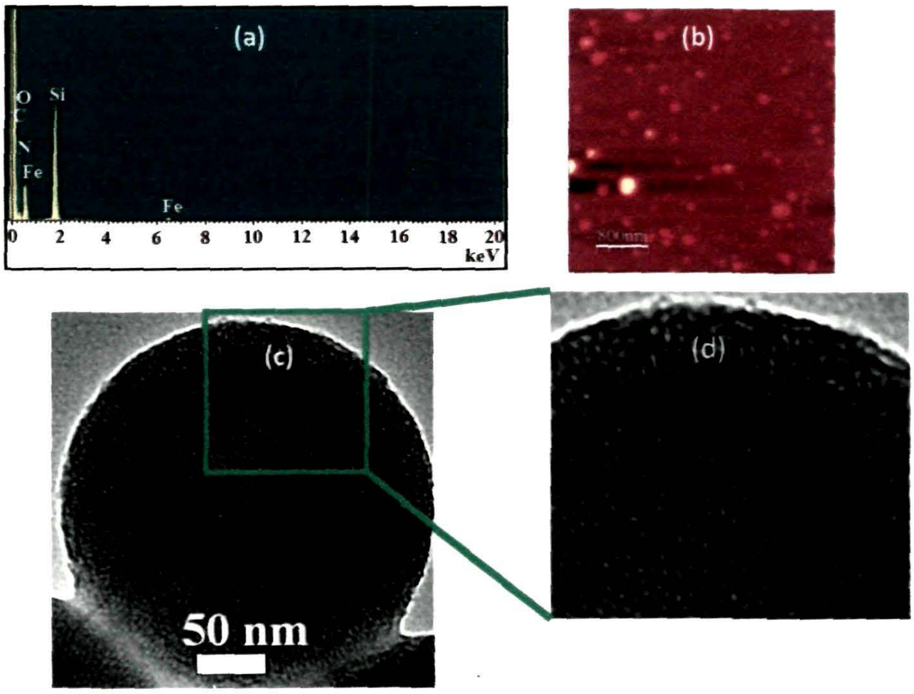

Figure 5.7 (a) EDX spectra and (b) AFM image of the hybrid, (c) HR-TEM image of one hybrid particle with radial distribution of pore channels and (d) the enlarged image of the small portion of (c).

In order to confirm the CTAB template removal by water extraction procedure, EDX characterization of the hybrid is performed. The EDX spectrum in Figure 5.7(a) shows no presence of Br which corroborates to the absence of CTAB in the hybrid. From the AFM image of the hybrid in Figure 5.7(b), a distribution of size is observed. However, most of the particles are seem to be in the size range of 100-150 nm which corroborates to the HR-TEM image in Figure 5.7(c). The enlarged image of the portion of (c) indicated by green box is shown in Figure 5.7(d), from which the radial distribution of the pore channels normal to the particle surface is clearly observed. To explain the evolution of such kind of microstructure of the hybrid, it is required to understand its formation mechanism. In this regard, the pictorial representation of the mechanism is illustrated in Figure 5.8. As depicted in Figure 5.8(a), the phase transformation of O-complex and SPION from oil to water phase is done with the help of cationic surfactant CTAB. Initially, an oil-in-water emulsion is formed by CTAB micelle formation [diagram 2 in Figure 5.8(a)] due to vigorous stirring of the mixture of chloroform solution of O-complex and CTAB solution. From this, the oil phase i.e. chloroform is evaporated out to obtain CTAB stabilized O-complex and SPION [diagram 3 in Figure 5.8(a)]. Next, during the silica hybrid formation, rod-like surfactant micelles containing nanoparticles in the core are formed in the reaction mixture due to vigorous agitation for C_{CTAB}>CMC [diagram 1 in Figure 5.8(b)] [30]. Then the negatively charged hydrolysis products of TEOS start attaching to the positively charged head groups of CTAB micelles and form a layer over it [as shown in the enlarged diagram 2 in Figure 5.8(b)]. These rod-like micelles coated with SiO_2 layer are organized into clusters under the influence of van der Waals forces to form silica particles of size ~ 100 nm [diagram 3 in Figure 5.8(b)] [30]. Then with CTAB removal by water extraction method, the micelles are washed out to yield the silica particles with radial distribution of pore channels, whereas the O-complexes and SPIONs remained attached to the walls of pores and in some cases the long chain molecules of O-complex can penetrate to the silica layer [diagram 4 in Figure 5.8(b)].

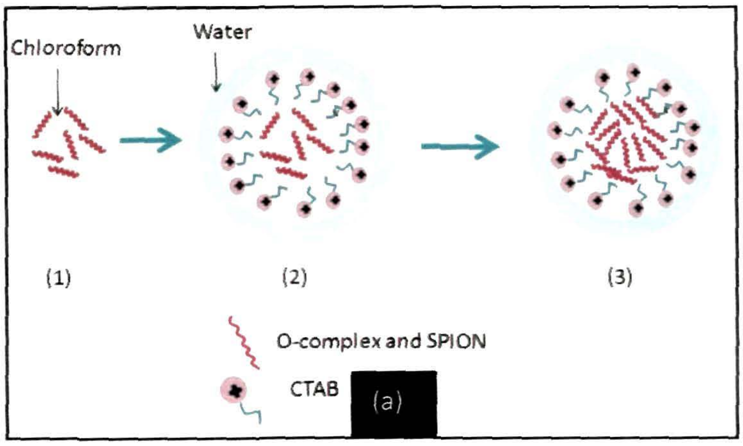

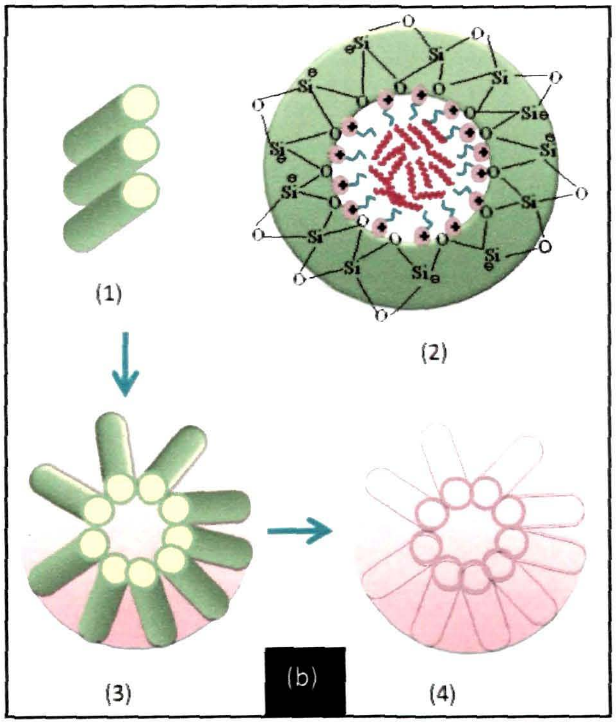

Figure 5.8 Schematic representation of (a) the phase transformation of the O-complex and SPIONs from oil to water phase and (b) the hybrid formation with radial distribution of pore channels.

To corroborate the porous morphology of the hybrids, pore size, BET surface area and pore volume were determined by using N_2-sorption technique at −196°C. The BET surface area was estimated using relative pressure in the range of 0.05 to 0.90. The pore size distribution was calculated from the adsorption branch by using Barett-Joyner-Halenda (BJH) method. Figure 5.9 (a) shows the N_2-sorption isotherm of the hybrid. The isotherm is observed to be of type II, indicating that the silica hybrid is mainly composed of microporous structures [31]. The BET surface area of the system is found to be 105.86 m^2/gm. The pore size distribution of the silica hybrids is depicted in Figure 5.9 (b). From this plot, the average pore diameter is observed to be ~ 2.4 nm and from the BJH data, average pore surface area and volume are obtained as 68.8 m^2/gm and 0.14 cc/gm respectively.

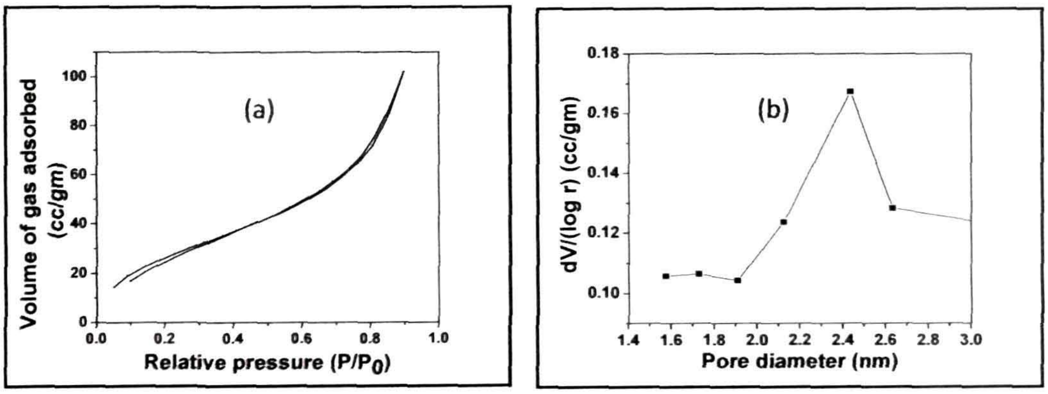

Figure 5.9 (a) N_2-sorption isotherm and (b) Pore size distribution plot of the hybrid.

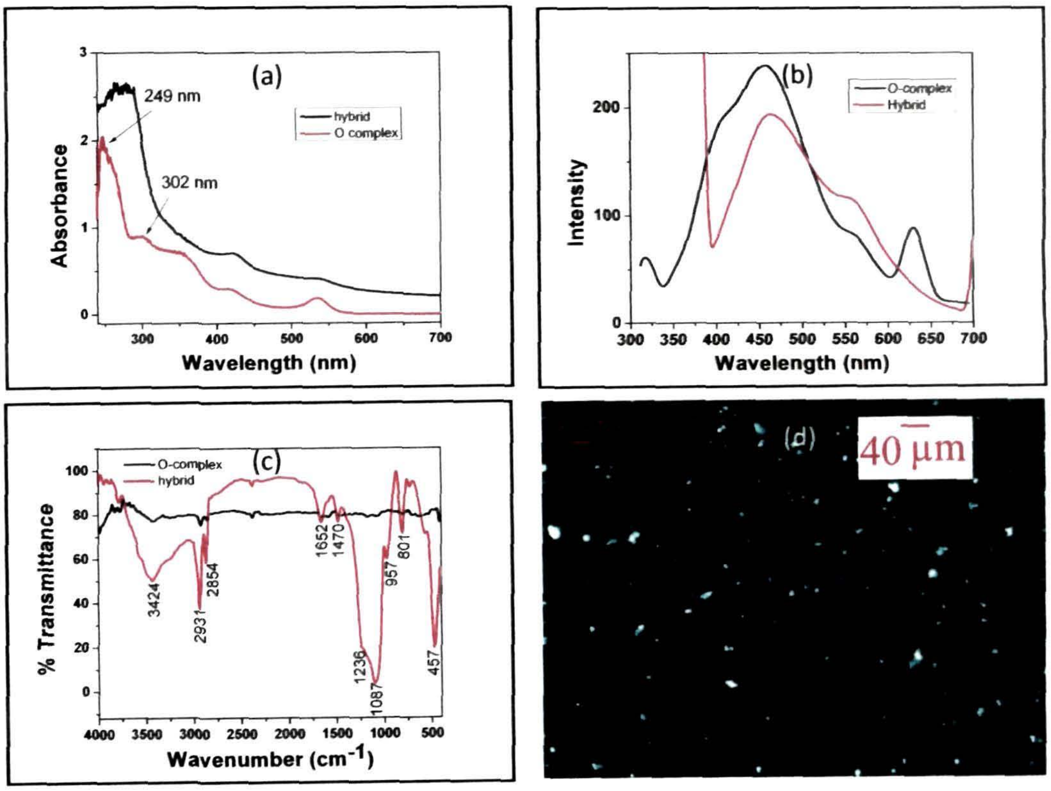

Figure 5.10 (a) UV-Visible absorption spectra, (b) Photoluminescence spectra, (c) FTIR spectra of O-complex and hybrid and (d) Fluorescence microscopy image of hybrid excited with UV-light (Filter A).

The optical and surface characteristics of the hybrid are studied and the results are shown in Figure 5.10. From the comparison plot of UV-Visible spectra of the O-complex and its hybrid in Figure 5.10(a), the characteristic peaks of glutaraldehyde are seem to be present in O-complex at 249 nm and 302 nm corresponding to $n \rightarrow \sigma^*$ and $n \rightarrow \pi^*$ transitions for aldehydic group respectively [32-33]. But in the hybrid these peaks have got suppressed due to the thick silica coating whereas the other peaks are intact. From the combined PL spectra of the dye and its hybrid, the broad emission peak is observed [Figure 5.10(b)]. This is the characteristic of dye molecule because of its complexity leads to line splitting producing broad absorption and emission curves. From the comparison, the hybrid emission peak seems to be quenched and slightly red shifted from that of the pristine dye. Intensity quenching is due to absorption of visible range wavelength by SPIONs and red shift is occurring may be because of nonradiative transition of electrons from excited dye molecules to new states on hybrid formation, before undergoing emission process. From the FTIR spectra of Figure 5.10(c), the characteristic silica peaks are observed as explained under the section 5.3 for silica hybrid A of SPION [refer Figure 5.2 (b)]. However, the broad peak at 3424 cm^{-1} is assigned to $N\text{-}H_{stretch}$ as it is weaker in strength as compared to $O\text{-}H_{stretch}$ while the 1652 cm^{-1} peak is assigned to the $N\text{-}H_{bend}$ vibration of amine group in the O-complex [34] The symmetric and antisymmetric $C\text{-}H_{stretch}$ and $C\text{-}H_{scissoring}$ bands of long alkyl chain of the O-complex are observed at 2854 cm^{-1}, 2931 cm^{-1} and 1470 cm^{-1} respectively [26]. Figure 5.10(d) shows the fluorescence microscopy image of the hybrid excited with UV light. From this, the bright fluorescent property of the hybrid is evidenced clearly which is beneficial in making the hybrid a potential optical imaging probe along with the magnetic functionality.

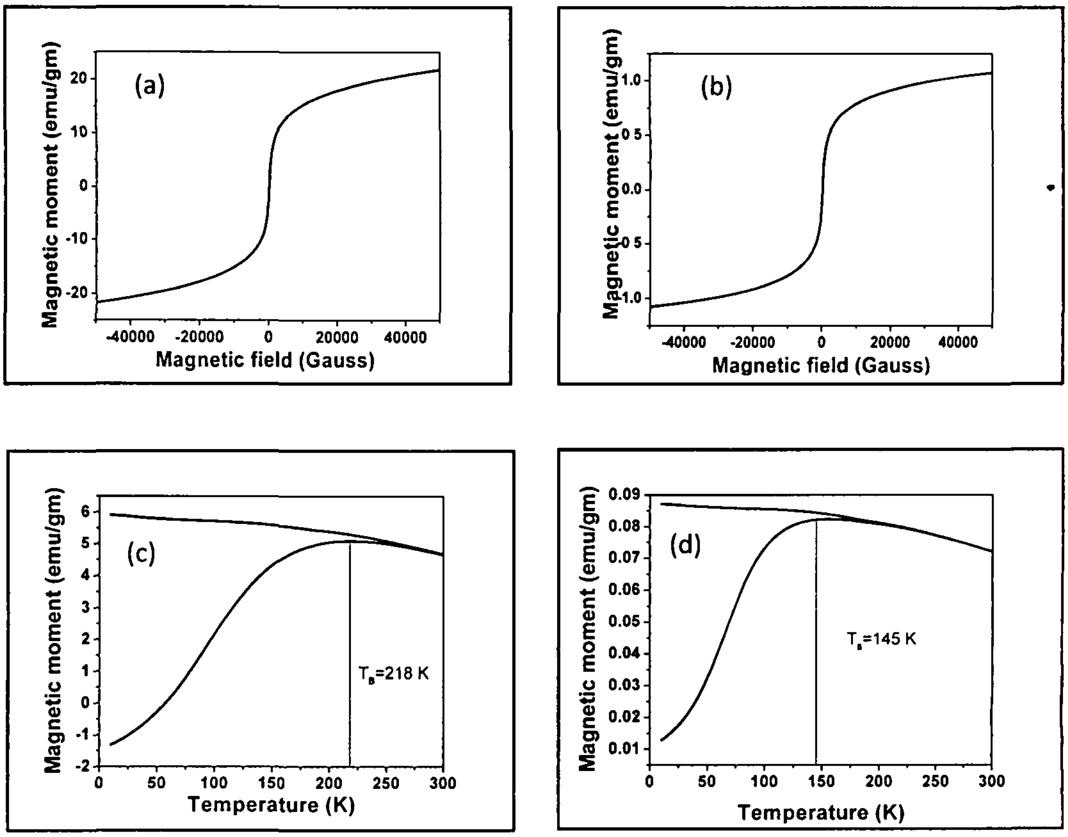

Figure 5.11 M-H curves of (a) SPION and (b) hybrid at 300 K. M-T curves of (c) SPION and (d) hybrid measured at 500 Oe.

The magnetic properties of the hybrid of the synthesized dye and SPION are studied through M-H and M-T characterization techniques. From the M-H characterization results, it is observed that the superparamagnetic character of SPION is retained after hybrid formation with silica and O-complex though there is a decrease in the saturation magnetization after hybrid formation [Figure 5.11 (a) and (b)]. This is due to the diamagnetic contribution from the thick silica coating as well as from the organic dye, O-complex. Also, it can be correlated with the surface spin disorder of SPION induced by silica coating [35]. From the M-T characterization curves of SPION and its hybrid, the superparamagnetic property is further confirmed with splitting of FC and ZFC curves at a temperature above Blocking temperature, T_B. It is also observed that T_B

of SPION decreases from 218 K to 145 K on hybrid formation. The decrease in T_B on silica hybrid formation can be justified due to similar reasons as explained already in case of hybrids A, B and C [refer Figures 5.5 (e), (f) and (g)].

5.6 Conclusion:

In summary, silica based magneto-fluorescent hybrids of QD and SPION have been synthesized by both templated and non-templated route. The hierarchically architectured structure of the hybrids based on nanocomponent units was studied by small angle X-ray and neutron scatterings. The SANS and SAXS results exhibit that the silica hybrids synthesized by templated route are mesoporous in nature and are of size range ~ 100 nm. This analysis corroborate to the findings obtained from microstructural property studies. A mechanistic understanding of the formation of both porous and nonporous hybrids is put forwarded with schematic. However, superparamagnetic and fluorescent characteristics are observed to be retained in both the hybrids without significant differences. Therefore, the magneto-fluorescent hybrid with mesoporous structure and of relatively smaller size has been carried forwarded for multifunctional applicability study and a detailed compositional analysis of it has been performed with X-ray photoelectron spectroscopy. The XPS results show the presence of Si-O-Si and free Si-OH groups, γ-Fe_2O_3 phase of SPION, Cd^{2+} and Te^{2-} states of CdTe in the hybrid. Also by the templated method, a second hybrid of the synthesized dye, O-complex and SPION is developed and its microstructural, optical and magnetic characteristics have been studied. To understand the evolution of the pore channels with radial distribution in the hybrid as evidenced from HR-TEM image, a mechanism has been described with schematic. The hybrid particles seem to be in the size range of 100-150 nm from AFM study. The N_2-sorption measurements reveal the microporous characteristics of the hybrid whereas the superparamagnetic and fluorescent properties have been corroborated from magnetic and optical property studies.

References

[1] Selvan, S. T., Patra, P. K., Ang, C. Y. and Ying, J. Y. Synthesis of silica-coated semiconductor and magnetic quantum dots and their use in the imaging of live cells, *Angew. Chem., Int. Ed.* 2007, **46** (14), 2448-2452.

[2] Bose, S., et al. Observation of shell effects in superconducting nanoparticles of Sn, *Nature Mater.* **9** (7), 550-554, 2010.

[3] Corma, A. and Garcia, H. Supported gold nanoparticles as catalysts for organic reactions, *Chem. Soc. Rev.* **37** (9), 2096-2126, 2008.

[4] Tu, Y. C., et al. Improving the electron mobility of TiO_2 nanorods for enhanced efficiency of a polymer-nanoparticle solar cell, *Cryst. Eng. Comm.* **14** (14), 4772-476, 2012.

[5] Goswami, R., et al. Removal of As(III) from aqueous solution using functionalized ultrafine iron oxide nanoparticles, *Separtion Science & Technology* **46** (6), 1017-1022, 2011.

[6] Wang G., et al. The synthesis of magnetic and fluorescent bi-functional silica composite nanopaticles via reverse microemulsion method, *J. Fluoresc.* **19** (6), 939-946, 2009.

[7] Atanasijevic, T., Shusteff, M., Fam, P. and Jasanoff, A. Calcium-sensitive MRI contrast agents based on superparamagnetic iron oxide nanoparticles and calmodulin, *Proc. Natl. Acad. Sci.* **103** (40), 14707-14712, 2006.

[8] Thomas, L. A., et al. Carboxylic acid-stabilized iron oxide nanoparticles for use in magnetic hyperthermia, *J. Mater. Chem.* **19** (36), 6529-6535, 2009.

[9] Xu, H., et al. Antibody conjugated magnetic iron oxide nanoparticles for cancer cell separation in fresh whole blood, *Biomaterials* **32** (36), 9758-9765, 2011.

[10] Gu, H. W., Zheng, R. K., Zhang, X. X. and Xu, B. Facile one-pot synthesis of bifunctional heterodimers of nanoparticles: A conjugate of quantum dot and magnetic nanoparticles, *J. Am. Chem. Soc.* **126** (18), 5664-5665, 2004.

[11] Gao, J. H., et al. Fluorescent magnetic nanocrystals by sequential addition of reagents in a one-pot reaction: A simple preparation for multifunctional nanostructures. *J. Am. Chem. Soc.* **129** (39), 11928–11935, 2007.

---

[12] Gao, J. H., et al. Intracellular spatial control of fluorescent magnetic nanoparticles. *J. Am. Chem. Soc.* **130** (12), 3710-3711, 2008.

[13] Suteewong, T,. et al. Ordered mesoporous silica nanoparticles with and without embedded iron oxide nanoparticles: structure evolution during synthesis, *J. Mater. Chem.* **20** (36), 7807-7814, 2010.

[14] Kim, J., et al. Magnetic fluorescent delivery vehicle using uniform mesoporous silica spheres embedded with monodisperse magnetic and semiconductor nanocrystals, *J. Am. Chem. Soc.* **128** (3), 688-689, 2006.

[15] Basiruddin, S. K., Saha, A., Pradhan, N. and Jana, N. R. Functionalized gold nanorod solution via reverse micelle based polyacrylate coating, *Langmuir* **26** (10), 7475-7481, 2010.

[16] Hunag, C. C., et al. Enhnacing transversal relaxation for magnetite nanoparticles in MR imaging using Gd^{3+}-chelated mesoporous silica shells, *ACS Nano* **5**(5), 3905-3916, 2011.

[17] Kim, C. J., et al. Synthesis and characterization of polystyrene chains on the surface of silica nanoparticles: comparison of SANS, SAXS and DLS results, *Colloid. Polym. Sci.* DOI 10.1007/s00396-013-2923-z, 2013.

[18] Silverstein, R. M., Bassler, G. C. and Morril, T. C. *Spectrometric identification of organic compounds*, John Wiley & Sons, Canada, 1981.

[19] Mahtab, F., et al. Fabrication of silica nanoparticles with both efficient fluorescence and strong magnetization, and exploration of their biological applications, *Adv. Funct. Mater***21** (9), 1733-1740, 2011.

[20] Rubio, F., Rubio, J. and Oteo, J. L. A FTIR study of the hydrolysis of tetraethylorthosilicate (TEOS), *Spectroscopy Letters* **31**(1), 199-219, 1998.

[21] Lambers, J. and Hess, P. Infrared spectra of photochemically grown suboxides at Si/SiO_2 interface, *J Appl. Phys.* **94** (5), 2937-2941, 2003.

[22] Mishra, M. K. and Misra, N. M. Thermal decomposition kinetics of labile chromium complex with benzoic acid, *E-journal of Chemistry* 8(2), 513-516, 2011.

[23] Park, K., et al. Structural and magnetic properties of gold and silica doubly coated γ-Fe_2O_3 nanoparticles, *J Phys. Chem. C* **111** (50), 18512-18519, 2007.

---

[24] Coskun, M., et al. Synthesis of SiO_2 coated $NiFe_2O_4$ nanoparticles and the effect of SiO_2 shell thickness on the magnetic properties *J. Appl. Phys.* **107** (9), 09B523(1)-09B523(3), 2010.

[25] Yoschelis, S., et al. Formation of Au-Silane bonds, *Journal of Nanotechnology* **2012** (1), 903761(1)-903761(8), 2012.

[26] Gogoi, M., et al. Direct monophasic replacement of fatty acid by DMSA on SPION surface, *Appl. Surf. Sci.* **258** (24), 9685-9691, 2012.

[27] Barr, T. L. Recent advances in X ray photoelectron studies of oxides, *J. Vac. Sci. Technol. A* **9** (3), 1793-1805, 1991.

[28] Calareso, C., Grasso, V. and Silipigni, L. The cadmium seleniophosphate ($CdPSe_3$) XPS and XAES spectra, *Appl. Surf. Sci.* **171** (3-4), 306-313, 2001.

[29] Sun, T. S., Buchner, S. P. and Byer, N. E., *J. Vac. Sci. Technol.* **17** (5), 1067-1073, 1980.

[30] Trofimova, E. Y., et al. Monodisperse spherical mesoporous silica particles: fast synthesis procedure and fabrication of photonic-crystal films, *Nanotechnology* **24** (15), 155601(1)-155601(11), 2013.

[31] Johansson, E. M. *Controlling the pore size and morphology of mesoporous silica*, Ph. D. thesis, Linköping University, Sweden, 2010.

[32] Toshima, T. and Imai, M. Structure of a new oligomer of glutaraldehyde produced by aldol condensation reaction, *J. Org. Chem.* **56** (2), 694-697, 1991.

[33] Manna, U., Dhar, J., Nayak, R. and Patil, S., Multilayer single-component thin films and microcapsules via covalent bonded layer-by-layer self-assembly, *Chem. Commun.* **46** (13), 2250-2252, 2010.

[34] Kalsi, P.S., *Spectroscopy of Organic Compounds*: New Age International Publishers, Delhi, 2007. Print.

[35] Larumbe, S., et. al. Effect of a SiO_2 coating on the magnetic properties of Fe_3O_4 nanoparticles, *J. Phys. Condens. Matter.* **24** (26), 266007(1)-266007(6), 2012.

Chapter 6

Quantum confined Stark effect in magneto-fluorescent hybrid nanosystems

6.1 Introduction:

In the primitive days, Stark effect was defined as spectroscopic observation of an occasional transition between quantum states of a physical system due to the effect of a relatively weak perturbation varying sinusoidally in time [1]. In case of bulk semiconductors, application of electric field leads to broadening of the band-edge absorption, which was named as Franz-Keldysh effect [2]. However, proper inclusion of the Coulomb correlation of electron and hole leads to Stark effect of the exciton resonance to lower energies [3]. Large shifts in band-edge absorption in GaAs-AlGaAs quantum wells were observed for electric fields perpendicular to the layers which was explained in terms of quantum confinement in the thin semiconductor layers in contrast to Franz-Keldysh effect [4-5]. In general, the wavelength modulation of exciton emission/absorption of quantum confined system by applying an external electric field is described as Quantum Confined Stark effect (QCSE) [6-7]. Stark effect due to internal electric field is observed in case of unstrained GaN quantum wells with strained AlGaN barriers [8].The presence of strong electric field originated in this case due to balancing of the piezoelectric and spontaneous polarization in the well and barrier layers so that a flat Fermi level is obtained throughout the heterostructure. The initial QCSE studies in quantum well and wire were extended to quantum dots (QD) in subsequent years. In a capacitor-like geometry of single self-assembled CdSe/ZnSe QD, Stark shift was observed in the emission spectra under the influence of an external electric field [9]. Similarly, local electric field induced Stark shift, spectral diffusion and inhomogeneous broadening are reported in single CdSe QD [10]. Also, the luminescence of QD conjugated to functionalized carbon nanotube exhibited Stark shift under a local electric field induced by surrounding cations or anions of nanostructures in polar solvents [11]. Appropriate theoretical and experimental explanations were being forwarded for observed redshifted and blueshifted QCSE in quantum dot systems – governed by Coulomb dominance and the field induced effects [12].

Integration of QD with magnetic nanoparticles to develop magneto-fluorescent hybrid nanosystems will have enormous potential biomedical applications as simultaneous anatomic imaging and real time monitoring of molecular targeting through magnetic resonance (MR) and optical imaging [13]. For deep tissue imaging, there is an urgent need to develop bright and stable QDs that are broadly tunable in the far-red and infra-red spectral regions [14]. Also, to achieve simultaneous magneto-fluorescent imaging through diffuse optical tomography (DOT) and MRI, the fluorescent probes should emit in the NIR range (600-1000 nm) so that photon propagation in tissues is dominated by scattering rather than absorption [15-16]. Such QDs have been prepared by core-shell methods with tunable emission towards longer wavelength [17] but their application is limited to single functionality. Therefore, developing a hybrid of QD and magnetic nanoparticle with emission tuned towards longer wavelength without any external stimuli is of immense importance as multifunctional probe for magnetic resonance and optical imaging.

6.2 Experimental details:

Silica based magneto-fluorescent hybrid system of CdTe QD and superparamagnetic iron oxide nanoparticles (SPION) are developed by the procedures as described under the subsection 5.2.2 and 5.2.3 of chapter 5. Hybrid B and C are the systems prepared by template-free and templated route respectively. In their emission characteristics QCSE is realized by comparing the emission spectra of the pristine QD and that of its hybrids B and C. The Stark shift is measured for both the hybrids from the emission maxima in the photoluminescence (PL) spectra.

6.3 Results and Discussion:

Optical characterization of the two hybrids are done with the help of UV-Visible absorption and PL spectroscopy. Figure 1 presents the UV-visible absorption and PL spectra of hybrid B.

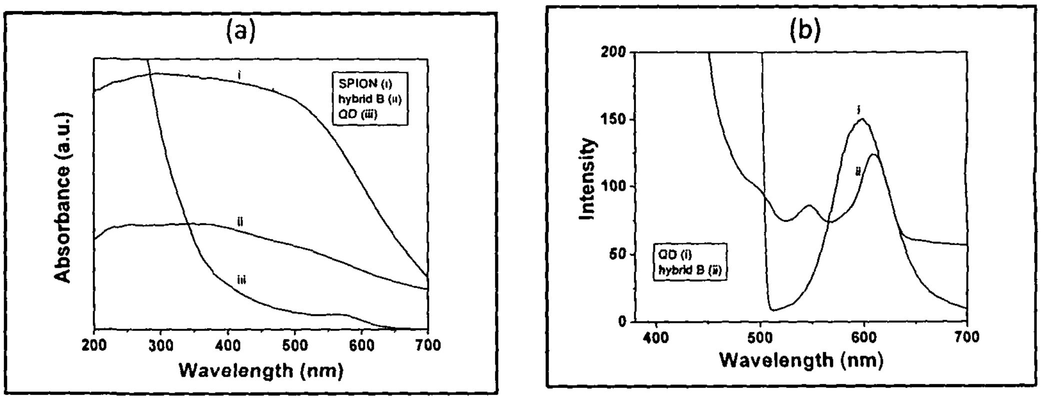

Figure 6.1(a) UV-Visible absorption spectra of SPION (curve i), hybrid B (curve ii) and QD (curve iii), (b) PL spectra of QD (curve i) and hybrid B (curve ii).

From the comparison plot of UV-Visible absorption spectra of QD, SPION and hybrid B in Figure 6.1(a), it is clearly evident that the hybrid possesses broad absorption peak of SPION covering almost the whole visible range and the QD absorption peak is masked under this peak. It is interesting to note from the comparative PL spectra of QD and hybrid B [Figure 6.1(b)] that significant red shifting of emission peak is observed in the hybrid from their pristine peak positions. For instance, the QD emission peak is red shifted by ~ 12 nm on hybrid formation and decreases in intensity too. In terms of energy, this can be quantified as a blue shift of 40.8 meV [Energy (eV)=1240/Wavelength (nm)]. The intensity quenching is attributed to the intense absorption by the SPIONs in the visible range as observed from the UV plot [refer Figure 6.1(a)] and thereby absorbs the emitted wavelength from the QDs in the hybrid. The observed shift in emission peak of QD in hybrid B can be ascribed due to the Quantum Confined Stark effect under local electric field, induced by the ionic environment of the hybrid sample surface. The development of this silica hybrid without template is mediated by the electrostatic force of attraction between free Cd^{2+}, Fe^{3+} ions of nanoparticles and OH^{-} ions of SiO_2 surface. Hence the dispersion of charges at the SiO_2 and solvent (polar) interface raises maximum possibility for the induction of a net local electric field around the SiO_2 particles [11]. Due to spherical shape of silica particles as evident from the HR-TEM image [refer Figure 5.4(b)], there should not be any net electric field at the core. Therefore, only the silanol groups present on SiO_2 surface contribute to the local electric field.

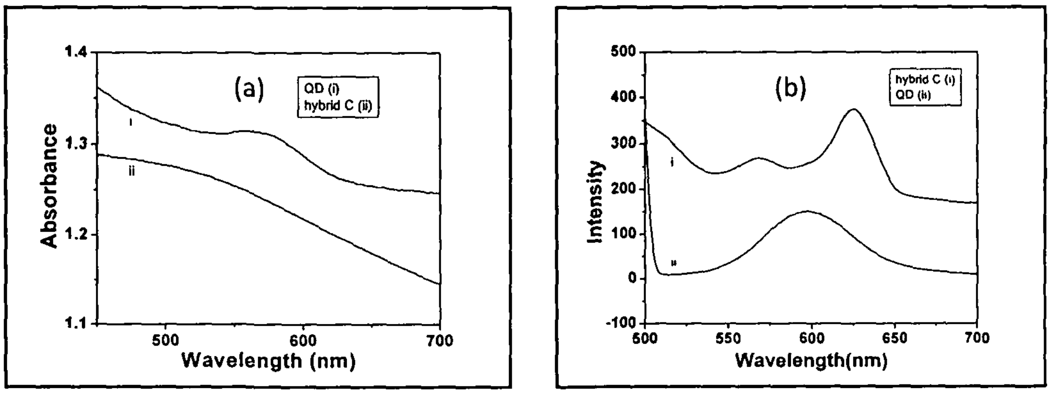

Figure 6.2 (a) UV-Visible absorption spectra of QD (curve i) and hybrid C (curve ii), (b) PL spectra of hybrid C (curve i) and QD (curve ii).

Similar optical investigations were carried out for hybrid C and the results are presented in Figure 6.2. The UV-Visible absorption spectra in Figure 6.2(a) shows that the QD absorption peak is entirely masked by the broad hump of SPION absorption in hybrid C. It is worthwhile to mention that the emission peak in this hybrid (curve i) is observed to be red shifted by ~27 nm from that of pristine QD [curve ii in Figure 6.2(b)] and in terms of energy, this can be correlated to a blue shift of 89.5 meV. The mentioned shifting in hybrid C is associated to 'Quantum Confined Stark effect' as well. To explain the presence of QCSE in this hybrid, its formation mechanism can be recalled. The development of hybrid C is followed by the templated synthesis mechanism resulting in silica structures with hollow core and the mesoporous shell containing the nanoparticles. With calcination, though the internal silanol groups condense to form solid silica but the groups present on the outer surface as well as on the walls of the mesopores remain intact. Hence, the existence of induced local electric field at the SiO_2/solvent (polar) interface is expected here.

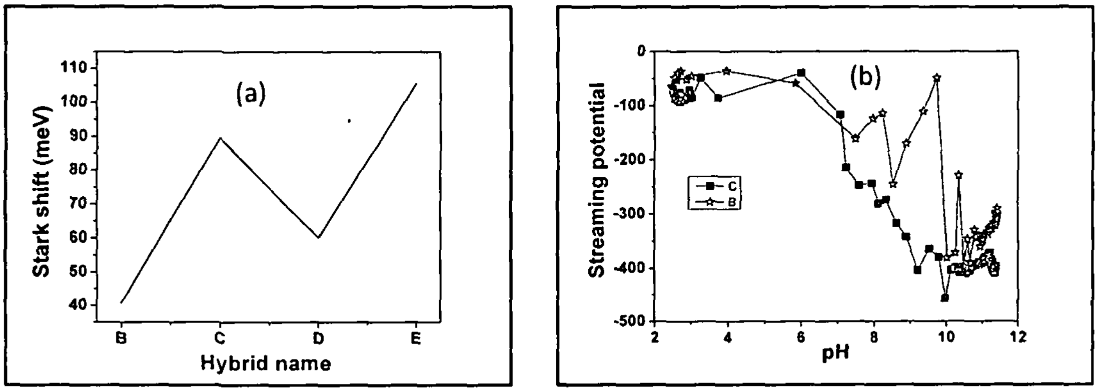

Figure 6.3 (a) Comparative Stark shift in hybrid samples and (b) Streaming potential plot of hybrids B and C.

To elucidate the effect of the superparamagnetic component, if any, in the observed QCSE, another two hybrids (D and E) were prepared without SPION and their optical properties were analyzed. Hybrid D and E are silica embedment of QD only, developed by template free and templated route respectively. From the analysis of Figures 6.1(b) and 6.2(b), it is observed that the Stark shift in the QD emission is significantly enhanced in case of mesoporous, smaller average particle sized hybrid C than B. In terms of energy, the Stark shift percentage is found to be 1.96% and 4.31% in hybrids B and C respectively w.r.t. the QD emission peak at 598 nm. It is interesting to note that exactly the same difference in Stark shift is observed between hybrids D and E also [Figure 6.3(a)]. Therefore, the Stark effect seems to be consistent with similar characteristics in the hybrids without the superparamagnetic component. The shift is a direct function of the induced local electric field that in turn is dependent on the density of charge present over the silica particles in polar solvents. In this regard, it is worthwhile to mention that the total charge developed by silica particles suspended in aqueous media vary widely depending on the size and porosity of the particles but the charge density at the outer surface is approximately constant, as is the density of surface hydroxyl group [18]. We are observing the Stark shift in emission spectra in the calcined samples of B and C. Due to calcination, the internal silanol groups condense to form siloxane bridges with simultaneous elimination of water. Therefore, the effect of density of charge due to internal silanol groups on the Stark effect for both the samples is nullified. Hence, the lone factor influencing the variation in Stark shift in hybrids B and C is the structure. Hybrid B is nonporous by nature. Therefore, the density of charge per unit mass, i. e. the specific charge is expected to be greater in hybrid C than in hybrid B. This is because of the fact that the ionization of silanol groups is confined to both outer surface and the walls of the mesopores of hybrid C while in hybrid B it is confined to the outer surface only. It is correlated with the streaming potential characteristics of the hybrids [Figure 6.3(b)]. For hybrid C, the streaming potential is found to be – 209 mV while for hybrid B is – 137 mV at the neutral pH. Moreover, the overall streaming potential seems to be higher for hybrid C in the whole pH range.

To estimate the order of the local electric field induced in the hybrid, a Hamiltonian is developed and Perturbation theory is applied to the exciton [19]. This is performed by considering the exciton as an analogous to hydrogen atom [20]. The electric field required to induce the first-order energy shift can be obtained from the following relation,

$$\Delta E = 3ea_B|E| \quad (1)$$

where, ΔE is the energy shift, e is the electronic charge having a value of 1.6×10^{-19} C, a_B is the exciton Bohr radius of CdTe having a value of 7.3 nm [21] and $|E|$ is the magnitude of electric field. Using this formula, the local electric field is evaluated as 1.8×10^4 V/cm and 4.0×10^4 V/cm in hybrids B and C respectively. Such strong electric field pulls the electron and hole inside the QD to opposite sides of the QD leading to a decrease of band gap and a red shift of the emission wavelength [9].

6.4 Conclusion:

In summary, quantum confined Stark effect (QCSE) in the emission characteristic of the hybrid of QD and SPION in silica matrix has been demonstrated. The observed QCSE is caused by local electric field, induced by the charge dispersion on SiO_2/polar solvent interface. The experimental results exhibit a Stark shift of 40.8 meV and 89.5 meV in the emission characteristics of the QD in a nonporous to mesoporous silica hybrid system respectively. The magnitude of the corresponding local electric fields are obtained as 1.8×10^4 V/cm and 4.0×10^4 V/cm in hybrids B and C. The observed enhancement in QCSE in case of mesoporous hybrid is assumed to be due to greater density of charge per unit mass, because the ionization of silanol groups is confined to both outer surface and the walls of the mesopores. However, the conjugation of SPION to the hybrid to achieve multifunctional attribute has no influence on the observed QCSE. Such a magneto-fluorescent hybrid system with emission wavelength modulation towards red end without the use of any external electric field has potential in biomedical imaging. Further tuning of emission characteristic of QDs upto NIR range by varying the parameters during hybrid formation will surely create a giant leap in simultaneous magnetic and fluorescent biomedical imaging application through DOT/MRI techniques.

References

[1] Autler, S. H. and Towens, C. H. Stark Effect in Rapidly Varying Fields, *Phys. Rev.* **100** (2), 703-722, 1955.

[2] Stillman, G. E. and Wolfe, C. M. Avalanche photodiodes, in *Semiconductors and Semimetals*, Willard-son, R. K. and Beer, A. C., eds., Academic Press, New York, 1977, 380-392.

[3] Dow, J. D. and Redfield, D. Toward a unified theory of Urbach's Rule and exponential absorption edges, D. *Phys. Rev. B* **5** (2), 594-610, 1972.

[4] Wood, T. H., et al. High-speed optical modulation with GaAs/GaAlAs quantum wells in a p-i-n diode structure, *Appl. Phys. Lett.* **44** (1), 16, 1984.

[5] Miller, D. A. B., et al. Band-edge electroabsorption in quantum well structures: the quantum-confined Stark effect, *Phys. Rev. Lett.* **53** (22), 2173-2176, 1984.

[6] Kulakci, M., Serincan, U., Turan, R. and Finstad, T. G. The quantum confined Stark effect in silicon nanocrystals, *Nanotechnology* **19** (45), 455403(1)-455403(5), 2008.

[7] Kuo, Y. H., et al. Strong quantum-confined Stark effect in germanium quantum-well structures on silicon, *Nature* **437** (7063), 1334-1336, 2005.

[8] Leroux, M., et al. Quantum confined Stark effect due to built-in internal polarization fields in Al,Ga N/GaN quantum wells, *Phys. Rev. B* **58** (20), R13 371-R13 374, 1998.

[9] Seufert, J., et al. Stark effect and polarizability in a single CdSe ZnSe quantum dot, *Appl. Phys. Lett.* **79** (7), 1033-1035, 2001.

[10] Empedocles S. A. and Bawendi, M. G. Quantum-confined Stark effect in single CdSe nanocrystallite quantum dots, *Science* **278** (5346), 2114-2117, 1997.

[11] Wang, W., et al. Surface charge induced Stark effect on luminescence of quantum dots conjugated on functionalized carbon nanotubes, *Chem. Phys. Lett.* **469** (1-3), 149-152, 2009.

[12] Ritter, S., et al. Anomalous Stark effect in semiconductor quantum dots, *Phys. Rev. B* **76** (16), 165302(1)-165302(7), 2007.

[13] Medarova, Z., et al. In vivo imaging of siRNA delivery and silencing in tumours, *Nat. Med.* **13** (3), 372-377, 2007.

[14] Gao, X., et al. In vivo cancer targeting and imaging with semiconductor quantum dots, *Nat. Biotechnol.* **22** (8), 969-976, 2004.

[15] Unlu, M. B., et al. A multimodal contrast agent for simultaneous magnetic resonance and optical imaging of small animals, *Proc. of SPIE* **7557**, 75570C(1)-75570C(7), 2010, doi: 10.1117/12.843240.

[16] Choe, R. *Diffuse optical tomography and spectroscopy of breast cancer and fetal brain*, Ph. D. Thesis, University of Pennsylvania, USA 2005.

[17] Wang, X., et al. NIR-emitting quantum dot-encoded microbeads through membrane emulsification for multiplexed immunoassays, *Small*, 6 March 2013, doi: 10.1002/smll.201203156.

[18] Wells, J.D., Koopal, L.K. and Keizer, A. Monodisperse, nonporous, spherical silica particles, *Colloids Surf. A* **166** (1-3), 171-176, 2000.

[19] Fitzpatrick, R. The linear Stark effect. http://farside.ph.utexas.edu/teaching/qm/lectures/node54.html, 2006.

[20] Vij, D. R. (ed.). *Luminescence of Solids*, Plenum Press, New York, 1998, pp. 103.

[21] Masumoto, Y. and Sonobe, K. Size-dependent energy levels of CdTe quantum dots, *Phys. Rev. B* **56** (15), 9734-9737, 1997.

Chapter 7

Potential applications of developed nanosystems

7.1 Introduction:

Magnetic nanoparticles have controllable size ranging from few to tens of nm which places them at comparable dimension to those of biological entity viz. a cell (10-100 μm), a virus (20-450 nm), a protein (5-50 nm) or a gene (2 nm wide and 10-100 nm long). Thereby, they can be applied for addressing the biological entity of interest in a controllable means. Also they can be manipulated by an external magnetic field gradient. These two combined functionalities open up many potential applications for magnetic nanoparticles involving transport or immobilization to a targeted region of the body (such as tumor) or by making the magnetic nanoparticles to resonantly respond to a time-varying magnetic field (MR imaging). Developing hybrid of magnetic nanoparticles with other nanosystem yield multifunctional nanosystem which combines more than one functionality in a single stable construct. In this chapter, we have investigated the potential application of representative so developed nanosystems in MRI technique as contrast agent as well as drug-protein loading capability. Moreover, multifunctional applicability as MRI contrast agent and therapeutic agent has been tested for a so developed single moiety nanosystem.

7.1.1 Basic principle of MRI technique:

MRI can provide both morphological and anatomical information noninvasively with high spatial resolution and without any limit on penetration depth [1]. Magnetic resonance is based upon the interaction between an applied magnetic field and a nucleus that possesses spin. It can be explained by considering an arbitrary volume of tissue containing protons (H^1). In absence of applied magnetic field, there will be random orientation of spin of the protons in all directions resulting in zero net magnetization in the tissue. However, in presence of a magnetic field, B_0, the individual protons begin to rotate perpendicular to, or precess about, the magnetic field [2]. The geometrical representation of the axis of precession is depicted in Figure 7.1, where, B_0 and the axis of precession are oriented in the z direction of Cartesian coordinate system. The x and y coordinates of the precessional motion vary with time but the z component is constant with time. The frequency of precession is known as Larmour precession and is expressed by equation (1) [2]:

$$\omega_0 = \gamma B_0 / 2\pi \qquad (1)$$

where, ω_0 is the Larmour frequency in megahertz (MHz), B_0 is the magnetic field strength in Tesla (T) and γ is a constant known as gyromagnetic ratio.

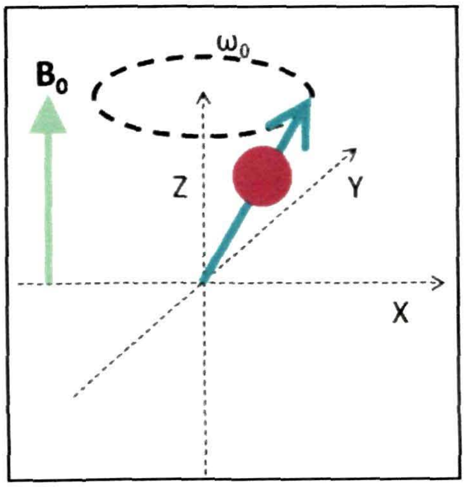

Figure 7.1 Schematic representation of Larmour precession of magnetic nucleus in presence of applied magnetic field.

Hence, due to the application of B_0, a net magnetization, M_0 is formed within the sample. Now, a pulse of radiofrequency energy containing many frequencies spread over a narrow range is applied to the protons. During the pulse, the protons absorb the portion of this energy at a particular frequency and get excited from spin up to spin down orientation. After the pulse, the protons emit the energy at same frequency. The energy difference between spin up and down levels is expressed by the following equation [2]:

$$\Delta E = \hbar\omega_0 = h\gamma B_0/2\pi \qquad (2)$$

where, h is Planck's constant and ħ is h divided by 2π. This quantized energy absorption is known as resonance absorption and the frequency of energy is known as resonant frequency. From the instant that the radio frequency pulse is turned off, the relaxation is measured via induced current in pick-up coils in the scanner. The relaxation signals are of the form [3]:

$$M_Z = M_0\left(1 - e^{-t/T_1}\right) \qquad (3)$$

$$M_{x,y} = M_0 \,\mathrm{Sin}(\omega_0 t + \varphi)e^{-t/T_2} \qquad (4)$$

where, T_1 and T_2 are longitudinal and transverse relaxation time and φ is a phase constant. Both T_1 and T_2 can be shortened by the use of contrast agent so that the contrast between lesions and nearby healthy tissue is amplified. The details of two types of relaxation time and the role of nanoparticles in shortening the relaxation time (i.e. acting as contrast agent) have been described under the section 1.4 of chapter 1.

Part A

7.2 Multicomponent multifunctional hybrid of SPION and QD:

The silica based magneto-fluorescent hybrid C of SPION and QD with mesoporous structure and of relatively smaller size (details in part A of chapter 5) has been investigated for potential multifunctional applications as MRI contrast agent and drug-protein loading vehicle. Also, due to the bright fluorescent property of the hybrid [refer Figure 5.4(f)], this can be used as a potential fluorescent probe in optical imaging.

7.2.1 Contrast property of SPION and its hybrid:

The MRI contrast property of the hybrid was evaluated by observing the transverse relaxation time (T_2) of water at 25°C with five different concentrations of hybrid (1.26, 0.63, 0.32, 0.1, 0.05, 0.025 and 0.01 mg/ml). The spin echo sequence of the microfuge tubes containing water was measured with different echo times with a 14.1T NMR microimager using repetition time TR=6 sec and echo time TE in the range of 7-600 ms. The MRI signal intensities with different echo times were fitted to a single exponential function $S_{TE}=S_{TE=0}(1-e^{-TE/T_2})$ to derive T_2. Transverse relaxation rate ($R_2=1000/T_2$) was calculated and plotted against hybrid concentration. Same measurements were taken for SPION only and the results are presented below.

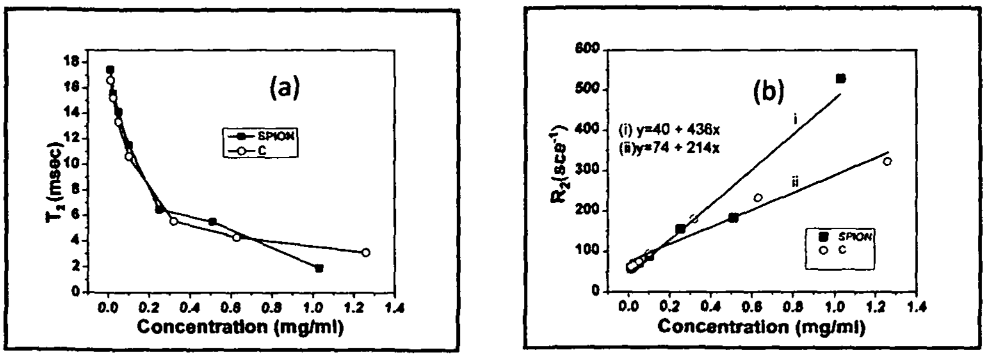

Figure 7.2 Comparison plot of (a) transverse relaxation time (T_2) and (b) variation of transverse relaxation rate (R_2) w.r.t. concentration of SPION and hybrid C.

It is observed from the comparison plot of transverse relaxation time in Figure 7.2(a) that T_2 of water decreases almost similarly with SPION and hybrid C (1.89 ms for SPION concentration of 1.03 mg/ml while 3.1 ms for hybrid C concentration of 1.26 mg/ml). The transverse relaxivity, r_2, determined from the slope of the plot between the transverse relaxation rate, R_2, against the concentration of hybrid C, is found to be 214 mg^{-1} mL s^{-1} whereas for SPION it is 436 mg^{-1} mL s^{-1} [Figure 7.2(b)]. The decrease in relaxivity, r_2, on hybrid formation can be understood from decrease of saturation magnetization value of it as described in the section 5.3 of chapter 5 [refer Figure

5.5(c)]. While for commercial T_2 contrast agent, feridex (Dextran coated SPION), the transverse relaxivity value is160 mM^{-1} sec^{-1} at a magnetic field of 0.47 T [4]. However, the above study indicates the potential of the hybrid as a promising T_2 contrast agent for MRI application.

7.2.2 BSA protein loading on mesoporous silica based hybrid nanosystem:

Different concentrations of hybrid C were added to four batches of BSA solution (7.31 μM) in PBS buffer of pH 6.9. Then the mixtures were kept on shaking for 3 hours at room temperature. The resulting solutions were seemed to be clear and all the samples showed absorbance at 280 nm in the UV-Visible absorption spectra. The calculations for BSA loading were made according to Beer Lambert's law with extinction coefficient of BSA, $\varepsilon = 43{,}824$ M^{-1} $cm^{-1}$and path length, l=1cm.

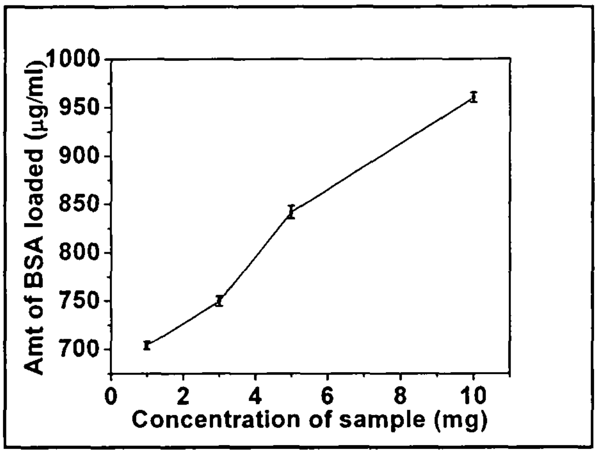

Figure 7.3 BSA adsorption on mesoporous silica based hybrid nanosystem.

Bovine serum albumin (BSA) is used as the model for human serum albumin. It is the major constituent of bovine blood plasma which can bind to various drug species [5]. The BSA adsorption efficiency of the mesoporous silica based hybrid C is studied as described above. It is observed from Figure 7.3 that with increase in concentration of the sample, the adsorption increases which is confirmed by attenuation in absorbance at 280 nm (characteristic absorption peak of BSA) in the UV-Visible absorption spectra of the solutions. This suggests a strong interaction between surface hydroxyl groups of silica particles and amine groups of protein molecules, leading to increase in amount of loading per surface area. The loading amount of BSA was determined as 9.6wt% by hybrid C. The loading amount increases with the increase of the concentration of the hybrid which suggests a strong interaction between the two. The mesoporous morphology adds to an enhancement of the total surface area of this hybrid leading to more no. of adsorption sites for BSA on its surface.

7.2.3 Drug loading on mesoporous silica based hybrid nanosystem:

Before performing the drug loading experiment, amine functionalization was done on the hybrid surface. For that, 12.3 mg of hybrid C was dispersed in 20 ml of toluene by sonication for 30 min. Then 2 ml of APTES was added to the mixture and the whole solution was put again under sonication for 15 min. Then the reaction was refluxed at 100°C for 12 hr under continuous N_2 flow. The final reddish colored product was obtained by centrifugation with more toluene addition and washed three times with 1:1 volume ratio of ethanol and water and then left for drying at 50°C.

Aspirin (acetylsalicylic acid) is a salicylate drug, often used as an analgesic. The commercially available drug is first extracted with ethanol to melt the base, following a reported procedure [6]. Then, four batches of PBS buffer solutions (pH 6.9), each of 5 ml, are mixed with four different concentrations of APTES functionalized hybrid silica samples. The concentrations of the samples used are 3 mg, 17 mg, 34 mg, 77 mg and 100 mg. To each of the solution, an amount of the drug 5.4 mg/ml was added and the mixtures were shaken for 24 hr at room temperature. The drug loading calculations were performed using the UV-Visible absorption spectra of the centrifuged solutions, assuming extinction coefficient of aspirin to be 14464 M^{-1} cm^{-1} and path length as 1 cm.

The results of APTES functionalization and drug loading experiment are presented in Figure 7.4. All the FTIR bands observed in Figure 7.4(a) are assigned to various stretching and bending vibrations of bonds in SiO_2 [refer to Figures 5.3(b), 5.4(a) and 5.4(d) of chapter 5]. The additional bands which appear in the functionalized hybrid are the bands at 1564 cm^{-1}, 1324 cm^{-1} and 604 cm^{-1}. These bands are assigned to $N\text{-}H_{bending}$, $C\text{-}N_{stretching}$ and $N\text{-}H_{wagging}$ vibrations of APTES molecule, respectively [7]. It is of interest to observe that the Si-OH band at 950 cm^{-1} appears distinctly even after APTES functionalization, making the hybrid system functionalized with different functional groups. From the drug loading experiment result in Figure 7.4(b), it is observed that with increase in concentration of the hybrid, the amount of loaded drug increases. The adsorption is occurring due to electrostatic attraction between positively charged amine groups of APTES functionalized silica particles and negatively charged salicylic acid molecules.

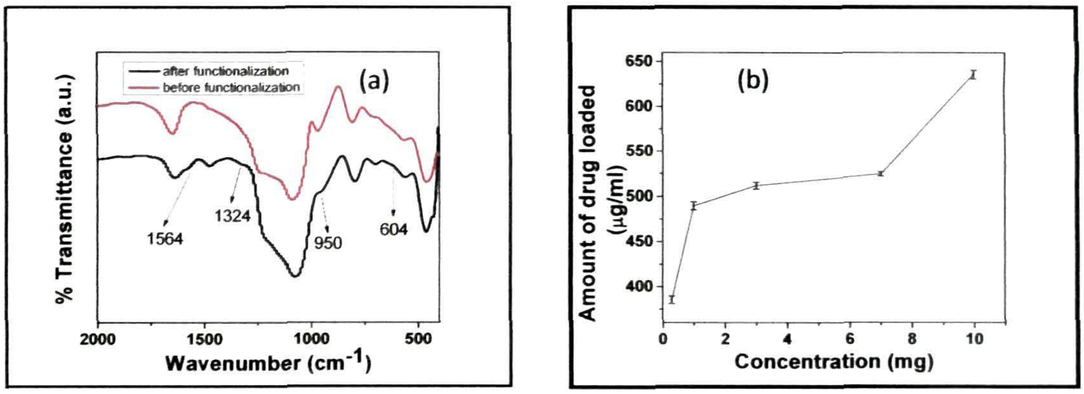

Figure 7.4 (a) FTIR comparison plot of hybrid C before (curve i) and after (curve ii) APTES functionalization and (b) drug loading efficiency of hybrid particles.

Part B

7.3 Single moiety, multifunctional iron-platinum nanoparticles:

Among the ascorbic acid capped iron-platinum nanoparticles synthesized by facile chemical route, sample P2 is superparamagnetic in nature (details in part B of chapter 3). Therefore, the potential application of so developed iron-platinum nanoparticle as MRI T_2 contrast agent has been studied. Moreover, the presence of cubic Pt phase along with cubic FePt phase in this sample, confer its potency as a therapeutic agent also. Therapeutic property of the sample has been realized by reactive oxygen species (ROS) generation from H_2O_2 (mimicking the cellular production of H_2O_2) at physiological pH by employing the catalytic property of Pt. Hence, this nanoparticle can serve as single moiety, multifunctional nanosystem in biomedical application.

7.3.1 Contrast property of nanoparticles in MR Imaging:

T_2 of water with different concentrations (0.05, 0.10, 0.25 and 0.5 mg/mL) of P2 sample was measured using a spin echo sequence as described under the section 7.2.1.

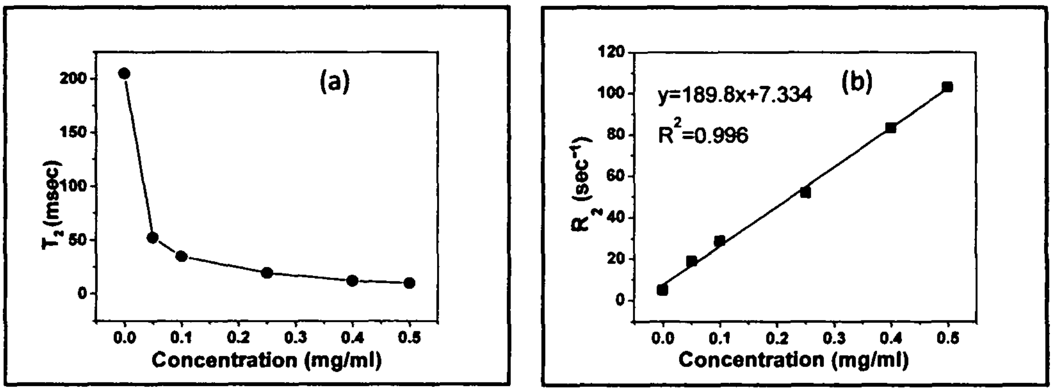

Figure 7.5 (a) Transverse relaxation time (T_2) and (b) Transverse relaxation rate (R_2=1000/T_2) with varying concentration of P2. The slope of the line in panel b indicates the relaxivity.

It is observed from relaxivity measurement of T_2-weighted proton that T_2 of water decreases drastically (55 ms vs 200 ms for pure water) at a concentration of 0.05 mg/mL nanoparticle [Figure 7.5(a)]. T_2 values further decrease with the increase of the concentration of FePt nanoparticles. The transverse relaxivity, r_2, determined by plotting the transverse relaxation rate, R_2=1000/T_2, against the concentration of nanoparticles, was found to be 189 mg^{-1} mL s^{-1} [Figure 7.5(b)].

7.3.2 Therapeutic— catalytic activity of the nanoparticles in generation of ROS:

To mimic the cellular production of ROS, the primary defense of the body, exogenous oxidant H_2O_2 was used. Fenton's reaction employs Fe-catalyzed H_2O_2 decomposition in which highly reactive oxygen species such as $OH^{\bullet}$ radicals are generated to cause death of tumor cells; in which acid etching of Fe-based nanoparticles was carried out for Fe release to take place [8]. To achieve similar kind of therapeutic at physiological pH and avoiding harsh processes like acid etching, the catalytic efficacy of Pt phase in decomposing H_2O_2 to generate ROS, was examined.

Generation of ROS from Pt-catalyzed H_2O_2 decomposition was evaluated by using 2′,7′-dichlorofluorescein (DCFH) as the indicator dye. DCFH was produced immediately before each assay by incubating 2′,7′-dichlorofluorescein diacetate (DCFHDA) in NaOH (0.1M) for 20 min. After incubation, basic DCFH solutions were diluted in phosphate buffer at neutral pH, for the experiments. To carry out the H_2O_2 decomposition experiment, six reaction flasks were taken. To each reaction flask, 0.125 mL of 0.01 M DCFH, 0.05 mL of 0.32 M H_2O_2 and 4.825 mL of Tris-HCl buffer solutions were added. The pH of the solution was checked to be 7.4. Then, five different concentrations of nanoparticle solution in water were added to the five flasks and one was the control reaction flask without nanoparticles. Then, room temperature shaking was applied for 12 h, followed by centrifugation to separate the nanoparticles. With the supernatant solutions, UV-Visible absorption spectroscopy was done. All the reactions and characterizations were carried out in the dark (light protected chamber).

For fluorescence microscopic study of ROS generation from H_2O_2 with 2′,7′-dichlorofluorescin (DCF is the oxidized form of DCFH) as the indicator, solutions from control as well as supernatants of the reaction mixtures were drop cast over glass slides and then covered with cover slips. They were allowed to dry for some time, and then were observed under fluorescence microscope, excited with wavelength 340-380 nm.

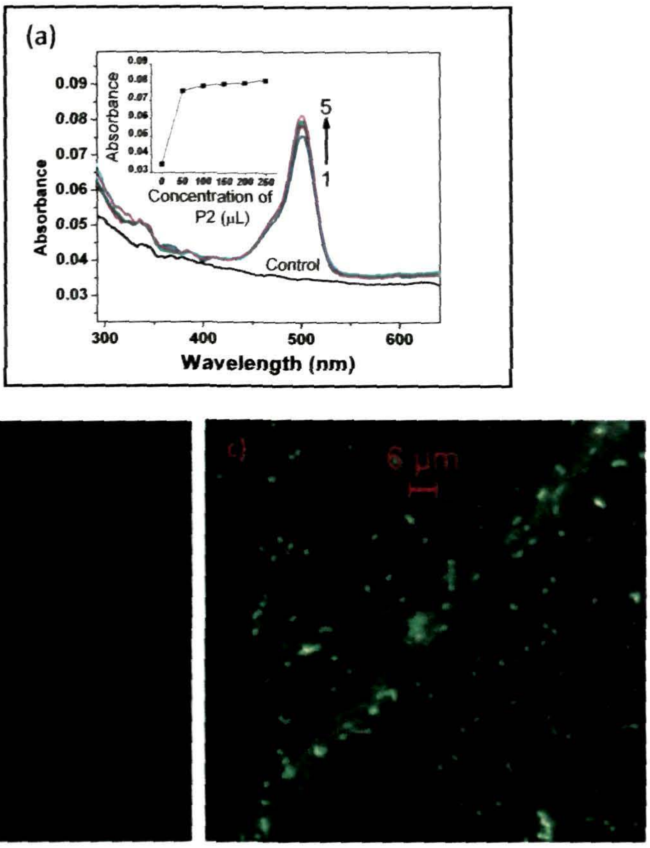

Figure 7.6 (a) Decomposition of H_2O_2 using P2 indicated by increasing absorbance of ROS-sensitive DCF. Here sample 1,2,3,4 and 5 are differentiated by the amount of P2 used as 50µL, 100 µL, 150 µL, 200 µL and 250 µL of a solution of concentration 1 mg/mL. Figure 7.6(b) and (c) show the fluorescence micrographs of control and sample 5.

Fluorescent product 2′, 7′- Dichlorofluorescin (DCF) is formed by oxidation of non-fluorescent DCFH [9]. Figure 7.6(a) shows an increase of absorbance in the UV–Visible absorption spectra of DCF at ~502 nm with increase in nanoparticle concentration. Increase in nanoparticle concentration leads to increased H_2O_2 decomposition, hence to increased oxidation of the DCFH, which is shown by the increased absorbance of the oxidation product DCF. The same conclusion follows from the observed many-fold increase in fluorescence intensity in fluorescence micrographs [Figure 7.6(b) and (c)].

7.4 Conclusion:

The potential application of hybrid of SPION and QD embedded in mesoporous silica matrix has been investigated in multifunctional aspects. To be a promising MRI T_2 contrast agent, the transverse relaxivity of this hybrid is obtained as 214 mg^{-1} mL s^{-1}. Then the efficacy of the hybrid has been tested as drug and protein loading vehicle. BSA protein is assumed to be adsorbed on hybrid surface through electrostatic interaction between surface hydroxyl groups of silica and amine groups of protein. Further APTES functionalization was done on silica surface and aspirin drug has been loaded on it by utilizing the same electrostatic interaction between amine groups of APTES and salicylic group of drug.

Also, the so developed ascorbic acid capped iron-platinum nanoparticles can act as single moiety, multifunctional nanosystem because of its unique composition. The iron-platinum nanoparticles exhibit efficiency in generating ROS from H_2O_2 decomposition, useful for tumor cell death and the transverse relaxivity of water against concentration of nanoparticle was found to be 189 mg^{-1} mL sec^{-1}.

References

[1] Fang, C. and Zhang, M. Multifunctional magnetic nanoparticles for medical imaging applications, *J. Mater. Chem.* **19** (35), 6258-6266, 2009.

[2] Brown, M. A. and Semelka, R. C. *MRI Basic Principles and Applications,* Wiley-LISS, New Jersy, 2003.

[3] Pankhurst, Q. A., Connolly, J., Jones S. K. and Dobson, J. Applications of magnetic nanoparticles in biomedicine, *J. Phys. D.: Appl. Phys.* **36** (13), R167-R181, 2003.

[4] Magnetic resonance technology information portal, Feridex, www.mr-tip.com/serv1.php?type=db1&dbs=Feridex, 2013.

[5] Yu, C. H., et.al. Immobilization of BSA on silica-coated magnetic iron oxide nanoparticle, *J. Phys. Chem. C* **113** (2), 537-543, 2009.

[6] Ahmad, I. and Vaid, F. H. M. Determination of benzoic acid and salicylic acid in commercial benzoic and salicylic acids ointments by spectrophotometric method, *Pak. J. Pharm. Sci.* **22** (1), 18-22, 2009.

[7] Kalsi, P. S. *Spectroscopy of organic compounds*, New Age International Publishers, Delhi 2007.

[8] Xu, C., et al. FePt nanoparticles as an Fe reservoir for controlled Fe release and tumor inhibition, *J. Am. Chem. Soc.* **131** (42), 15346-15351, 2009.

[9] Chignell, C. F. and Sik, R. H. A photochemical study of cells loaded with 2′,7′-dichlorofluorescin: implications for the detection of reactive oxygen species generated during UVA irradiation, *Free Rad. Bio. Med.* **34** (8), 1029-1034, 2003.

Chapter 8

8.1 Conclusion and future prospect:

In the present thesis, an in-depth study on synthesis and structure-property correlation of magneto-fluorescent hybrid and its constituent nanocomponents have been presented. Applicability of so developed optimized systems as potential MRI contrast agent, therapeutic agent and drug-protein loading vehicle have been investigated.

Superparamagnetic iron oxide nanoparticles (SPION) have been synthesized and successfully surface modified to transfer from hydrophobic to hydrophilic phase [1]. Our study shows that in presence of excess surfactant, there are multilayers of stearic acid molecules on nanoparticle surface. The first layer is chemisorbed over it while the subsequent layers are physisorbed through tail to tail hydrophobic interaction. Therefore, by pH adjustment from acidic to basic, the stearic acid capped SPIONs can be made water soluble. However, to obtain an ultrastable SPION suspension in water, useful for biomedical applications, controlled replacement of stearic acid by hydrophilic, small ligand DMSA has been carried out. Then size-tunable undoped and Mn^{2+}-doped CdTe QDs have been developed through an aqueous method. It is observed that though in pristine CdTe preparation, a size-series of QDs can be obtained through refluxing governed by Ostwald ripening, but in case of Mn^{2+}-doped CdTe system, refluxing for similar period results into growth, disintegration and again growth of NC. Surface adsorbed Mn^{2+} promotes faster growth rate of the NCs to reach saturation and then disintegration into smaller fraction with refluxing time [2]. After that silica based magneto-fluorescent hybrid of SPION and optimized size fraction of CdTe QD have been developed through templated and template-free methods. The hierarchical structure formation of the hybrid based on the nanocomponent units have been revealed through small angle X-ray and neutron scattering studies and are corroborated by corresponding microstructural analysis [3]. In addition, an organic dye has been synthesized by a facile method and a magneto-fluorescent hybrid of the dye and SPION has been developed using silica as the matrix. The so developed hybrid evolved out as microporous structure with radial distribution of pore channels perpendicular to the surface [4]. A mechanistic understanding of the nonporous, mesoporous and microporous hybrids have been proposed with schematic diagrams. Interestingly, the emission characteristic of the magneto-fluorescent hybrid of SPION and QD exhibit quantum confined Stark effect under the influence of local electric field induced by charge dispersion at SiO_2/polar solvent interface. In case of the mesoporous hybrid, the Stark shift is observed to be enhanced which is demonstrated by increased specific charge over the mesoporous hybrid surface as compared to the nonporous one. A quantitative estimation of the magnitude of the induced local electric field has been carried out by considering the exciton as an analogous to hydrogen atom [5]. Then the transverse relaxivity of SPION and its silica based hybrid are measured to ascertain its potency as MRI T_2 contrast agent.

Another magnetic system i.e. iron-platinum nanoparticles have been synthesized by a simple, one-pot and aqueous chemical route using ascorbic acid as reducing as well as capping agent. While performing reduction, the ascorbic acid gets oxidized to dehydroascorbic acid which acts as the capping agent of the nanoparticles. Variation in reaction conditions such as reducing agent, pH and sequence of precursor addition has resulted in significant differences in composition and magnetic property of the synthesized nanoparticles [6]. Due to the presence of cubic Pt phase along with the cubic FePt phase in the superparamagnetic iron-platinum nanoparticles, the potential application of the nanoparticles has been demonstrated to serve as therapeutic agent (utilizing the catalytic property of Pt) and MRI T_2 contrast agent.

The future outlook of this thesis can be extended to synthesize various combinations of QD/dye and magnetic nanoparticles to develop hybrids. Also, more fucntionalities can be integrated to the hybrids in addition to the explored ones in the present thesis. Efficiency judgment of the developed systems in real applications like *in* *vivo* can be researched. In this regard, MRI has been done in mouse abdomen injected with iron-platinum nanoparticles and the results are presented in APPENDIX B. One can utilize the QCSE governed red shifting of the hybrid emission characteristic to develop NIR emitting fluorescent probe and investigate the simultaneous dual contrast property of the magneto-fluorescent hybrid through DOT/MRI techniques.

References:

[1] Gogoi, M., et al. Direct monophasic replacement of fatty acid by DMSA on SPION surface, *Appl. Surf. Sci.* **258** (24), 9685-9691, 2012.

[2] Gogoi, M., Deb, P. and Kostka, A. Differential tunability effect on the optical properties of doped and undoped quantum dots, *Phys. Status Solidi A* **209** (8), 1543-1551, 2012.

[3] Gogoi, M., et al. Probing hierarchically structured mesoporous maglumino hybrid multifunctional nanomaterial (communicated).

[4] Gogoi, M. and Deb, P. Fabrication of a hybrid of newly synthesized fluorescent dye and SPION with radial porous channels (communicated).

[5] Gogoi, M., et al. Enhanced quantum confined Stark effect in a mesoporous hybrid multifunctional system (communicated).

[6] Gogoi, M., et al. Single moiety, multifunctional Iron-Platinum nanoparticles synthesized by facile aqueous route (communicated).

APPENDIX A

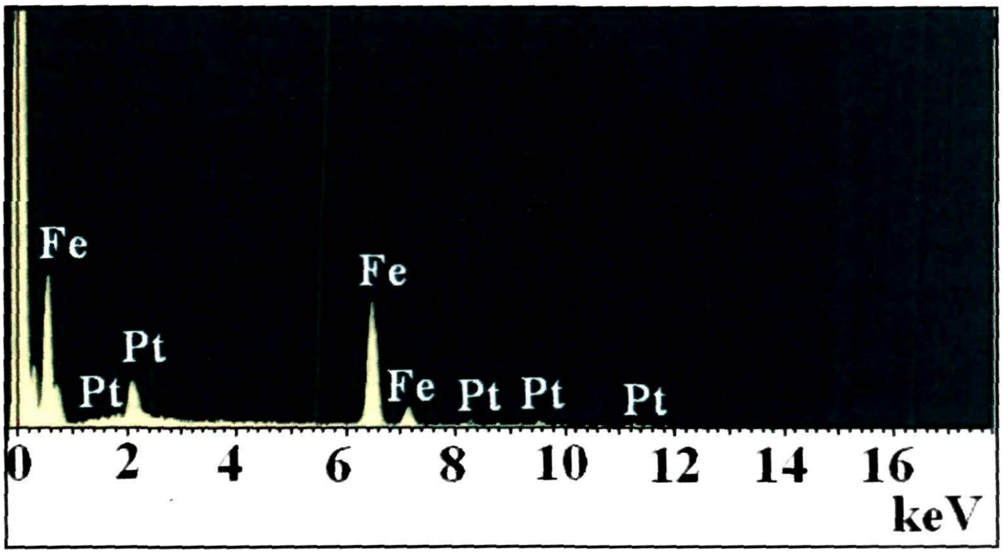

Figure C-1. The EDX spectra of the P3 sample synthesized at alkaline pH.

APPENDIX B

Experiment: T_2-weighted MR images of the abdomen of mouse were obtained before and after (45 min) administration of the nanoparticles of P2 sample using the parameters: TR = 4000 ms, TE = 14 ms, slice thickness = 0.5 ms, FOV = 28 x 28 mm^2; matrix size = 128 x 128 and number of averages =2. The ascorbic acid capped FePt nanoparticles were injected through tail vein, 5 mg/kg (0.5 mg/ml) in mouse (~30 g). The acquisition of the MRI image was synchronized with the respiration of the animals (measured by placing a balloon under the lung) to correct the artefacts related with the respiration.

The mathematical calculation followed is shown below:

Mouse weight ~ 30 gm

Dose required ~ 5 mg/kg

So, amount of nanoparticles to be injected in mouse = 0.03 kg X (5mg/kg)

= 0.15 mg of nanoparticle

Initial concentration of the nanoparticle solution ~ 0.5 mg/ml

So, from $C_1V_1=C_2V_2$

0.5 mg X V_1 = 0.15 mg X 1 ml

V_1 = (0.15/0.5) ml = 0.3 ml

Hence, 0.3 ml of 0.5 mg/ml solution is injected in mouse of 30 gm at a dose of 5 mg/kg.

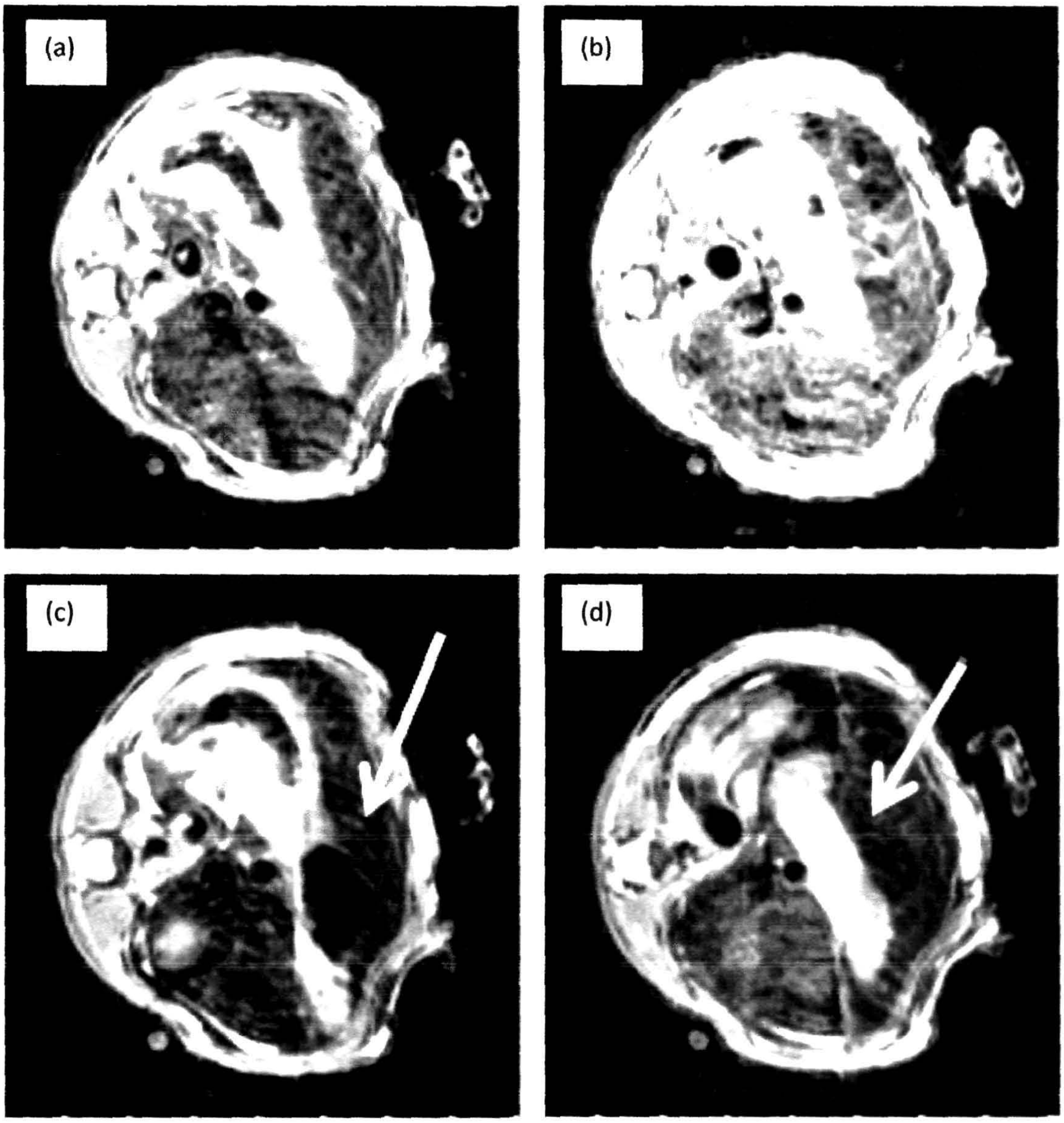

Figure D-1. The T_2 weighted MR images of mouse abdomen pre (a and b) and post (c and d) administration of P2. The hypointensity in liver following administration of P2 is indicated with white arrow (c, d).

Observation: From the MR imaging *in vivo*, it is clear that the signal intensity is reduced significantly in the liver [Fig D-1(c) and (d), indicated with arrows] following administration of FePt nanoparticles as compared to the corresponding pre-administered images [Figure D-1(a) and (b)].

List of publications

Included in thesis

[1] Chakrabarty, S., Gogoi, M., Kalita, E. and Deb, P. Multifucntional, high luminescent, biocompatible CdTe quantum dot fluorophores for bioimaging applications, *International Journal of Nanoscience* **10** (4-5), 1191-1195, 2011.

[2] Gogoi, M., et al. Direct monophasic replacement of fatty acid by DMSA on SPION surface, *Appl. Surf. Sci.* **258** (24), 9685-9691, 2012.

[3] Gogoi, M., Deb, P. and Kostka, A. Differential tunability effect on the optical properties of doped and undoped quantum dots, *Phys. Status Solidi A* **209** (8), 1543-1551, 2012.

[4] Gogoi, M., et al. Probing hierarchically structured mesoporous maglumino hybrid multifunctional nanomaterial (communicated).

[5] Gogoi, M. and Deb, P. Fabrication of a hybrid of newly synthesized fluorescent dye and SPION with radial porous channels (communicated).

[6] Gogoi, M., et al. Enhanced quantum confined Stark effect in a mesoporous hybrid multifunctional system (communicated).

[7] Gogoi, M., et al. Single moiety, multifunctional Iron-Platinum nanoparticles synthesized by facile aqueous route (communicated).

Not included in thesis

[1] Gogoi, M. and Deb, P. Light scattering behavior of magnetic field induced directional self assembly of iron oxide nanoparticle suspension, *NANO* 7 (4), 1250027(1)-1250027(7), 2012.

[2] Deb, P., Gogoi, M. and Karmakar, P. K. Anomalous magneto-optic Faraday rotation behavior due to resonant tunneling of magnetic moment, *J. Opt.* **41** (1), 41-47, 2012.

Patents

[1] Multifunctional nanoparticles and methods for synthesis thereof, application no. 1742/DEL/2013.

[2] Method for kinetic analysis of solid state processes from nonisothermal calorimetry (processed, ref no. BT/BPFC/04/70/2012 and IP22306/KA).

Copyright registered

[1] **MaxQ**: Programme for microstructural study of nanomaterials from X-ray diffraction pattern analysis, 9277/2013-Co/SW

[2] **KinLac**: Programme for kinetic analysis of solid state process, 9278/2013-Co/SW

Conference attended

International

[1] "Multicolour, high luminescence, biocompatible CdTe quantum dot based fluorophores for bioimaging applications", S. Chakraborty, M. Gogoi, E. Kalita and P. Deb, International Conference on Nanoscience and Technology. 2010, IIT Bombay. (poster)

[2] "Surface functionalization mediated enhanced bio-distribution of SPION for diagnostic applications", H. Sonowal, M. Gogoi, P. Deb, A. Erbe, G. Vasan and E. Kalita, International Conference on Nanoscience and Technology. 2010, IIT Bombay. (poster)

[3] "Light scattering by single domain nanoparticle suspension", M. Gogoi and P. Deb, International Conference on Advanced Nanomaterials and Nanotechnology. 2009, Center for Nanotechnology, IIT Guwahati. (poster)

[4] "Light propagation in nanomagnets", M. Gogoi and P. Deb, International Conference on Trends in optics and photonics, 2009, Department of Applied Optics and Photonics, University of Calcutta. (oral)

National

[1] "Preparation of nanocrystalline iron oxide particles and their characterization", M. Gogoi and P. Deb, National seminar on photonics and quantum structures, 2009, Department of Physics, Tezpur University (poster).

[2] "Superstructure formation in iron oxide nanoparticles studied through electron diffraction", M. Gogoi and P. Deb, National workshop on nuclear and atomic techniques based pure and applied sciences, 2011, Department of Physics, Tezpur University (poster).